(JOURNAL ENGINEERING DESIGN AND TECHNOLOGY)

VOL. 26 NO. 2 (2026)

JURNAL RANCANG BANGUN DAN TEKNOLOGI

P-ISSN. 1412-114X | E-ISSN. 2580-5649

Journal of Engineering Design and Technology

Gedung P3M, lt.1 Politeknik Negeri Bali, Bukit Jimbaran

PO BOX 1064 Kuta Selatan, Badung, Bali - Indonesia

Telp. (+62)361 701981 Fax. (+62)361 701128

Email: logic@pnb.ac.id

LOGIC JOURNAL TEAM

PREFACE

Logic: Jurnal Rancang Bangun dan Teknologi (Journal of Engineering Design and Technology) is a peer-reviewed research journal aiming at promoting and publishing original high quality research in all disciplines of engineering and applied technology. All research articles submitted to Logic should be original in nature, never previously published in any journal or presented in a conference or undergoing such process across the world. All the submissions will be peer-reviewed by the panel of experts associated with particular field. Submitted papers should meet the internationally accepted criteria and manuscripts should follow the style of the journal for the purpose of both reviewing and editing.

Logic is a journal covering articles in the field of civil and mechanical engineering, design, and technology published 3 times a year in March, July, and November. Language used in this journal is English.

LOGIC. P-ISSN 1412-114X

LOGIC. E-ISSN 2580-5649

Indexing : Google Scholar, DOAJ, EBSCO Open Science Directory, SINTA, GARUDA

Best Regard,

LOGIC Editorial Team

TABLE OF CONTENTS

Journal Engineering Design and Technology
Vol. 26 No.2 July 2026 ; p. 95 - 102
Journal Homepage : http://ojs2.pnb.ac.id/index.php/LOGIC
p-ISSN : 1412-114X e-ISSN : 2580-5649

Evaluation of Lathe Operating Conditions Based on ISO 10816 Using Correlation Between Spindle Vibration and Surface Quality

Talifatim Machfuroh [1)*], Zakiyah Amalia [1)], Siti Duratun Nasiqiati Rosady [1)], Nurlia Pramita Sari [1)], Agus Hardjito [1)], Subagiyo [1)]

1) Mechanical Engineering, State Polytechnic of Malang, Malang, Indonesia

Corresponding email [1)*] :
talifatim.machfuroh@polinema.ac.id

Abstract. The evaluation of machine tool operating conditions is commonly performed based on mechanical reliability, while its direct relationship with the quality of machined surfaces is still rarely quantified. This study aims to evaluate the operating condition of a conventional lathe based on ISO 10816 by analyzing the correlation between spindle vibration and surface roughness. Experiments were conducted on a Dixon CQ6236X1000 lathe with variations in feed rate (0.104–0.835 mm/rev) and depth of cut (0–1.5 mm) at a constant spindle speed of 460 rpm. Spindle vibration was measured in terms of root mean square (RMS) velocity (mm/s) in the vertical and horizontal directions, and frequency-domain analysis was performed using Fast Fourier Transform (FFT). Surface roughness was evaluated using Ra, Rq, and Rz parameters. The results show that the RMS vibration values range from 0.4 to 2.5 mm/s, which correspond to Zone B and Zone C of ISO 10816-3 class I. At Zone B, the surface roughness values are relatively low (Ra = 2–6 µm), indicating stable machining conditions. However, when the operating condition shifts to Zone C, the surface roughness increases significantly, with Ra values exceeding 10 µm under certain cutting conditions. The correlation analysis between RMS vibration and surface roughness yields a coefficient of determination of R^2 = 0.399, indicating a moderate positive relationship. FFT analysis shows dominant frequency components associated with spindle rotational frequency and its harmonics, indicating the presence of forced vibration effects induced by cutting dynamics. No definitive conclusion regarding regenerative chatter is made, as further modal and stability analysis is required. These findings indicate that ISO 10816 vibration zones may serve as a supporting indicator for preliminary machining quality assessment, rather than a direct predictive tool for surface roughness. The results provide a useful reference for integrating vibration-based condition monitoring with machining quality control in both industrial and educational workshop environments..

Keywords : ISO 10816, Spindle Vibration, Surface Roughness, RMS Velocity, Turning Process

1. INTRODUCTION

A lathe is one of the primary machine tools in the manufacturing industry used to produce cylindrical components with a certain level of precision. In the machining process, the quality of the cutting results is not only determined by cutting parameters such as spindle speed, feed rate, and depth of cut, but is also strongly influenced by the dynamic stability of the spindle–tool–workpiece system. This dynamic stability plays a crucial role in maintaining

dimensional accuracy and surface quality, particularly for components that require tight tolerances.
From a physical standpoint, all objects possessing mass and elasticity are capable of undergoing vibration; therefore, almost all machines and engineered structures experience vibrations to some degree. Vibration is defined as a reciprocating or oscillatory motion of an object that has both mass and elasticity, analogous to a mass–spring system [1]. In machine tool operation, vibration is an unavoidable phenomenon. However, in most industrial applications, excessive vibration is undesirable because, in addition to increasing dynamic stress on machine components, it also leads to energy losses that should otherwise be utilized effectively in the machining process [2][3][4].

In a lathe, spindle vibration has a direct influence on machining quality. Spindle vibration can cause irregular tool motion, which results in a rougher workpiece surface [5] and reduced dimensional accuracy [6]. Fluctuations in tool position induced by vibration lead to non-uniform material removal, thereby increasing surface roughness parameters such as Ra and Rz [7][8]. Furthermore, excessive vibration accelerates tool wear and increases the risk of damage to machine components, which ultimately degrades machining precision and product quality, especially for components with high quality requirements [9].

In industrial practice, machine condition is often evaluated using vibration severity standards such as ISO 10816. However, ISO 10816 is primarily intended for mechanical condition monitoring and not directly for machining quality evaluation. This standard classifies machine operational condition into several zones according to the effective vibration velocity (RMS velocity), ranging from very good to unacceptable conditions. Nevertheless, in practical applications, it is frequently observed that a machine may still be mechanically classified as acceptable according to ISO 10816, while the surface quality of the machined products has already deteriorated. This indicates that mechanical acceptability does not always correspond directly to the quality of the resulting products.

Several previous studies have investigated the effects of cutting parameters on vibration and surface roughness. Panda et al. (2018) monitored the condition of bearing housing in a lathe through vibration analysis with variations in spindle speed and depth of cut, demonstrating that vibration characteristics are influenced by both mechanical and operational factors [10]. Fitriana et al. (2021) and Alfianto et al. (2018) reported that increasing spindle speed leads to higher vibration levels accompanied by increased surface roughness [11][12]. Retyawan et al. (2018) showed that the type of cutting process also affects vibration and surface roughness in milling operations [13]. Meanwhile, Şahinoğlu dan Rafighi (2020) demonstrated that feed rate, depth of cut, and cutting speed significantly influence vibration and surface roughness during the turning of AISI 4140 steel [14]. However, most of these studies still consider vibration and surface roughness as direct consequences of variations in cutting parameters, without directly relating them to machine acceptability zones based on ISO 10816.

Previous studies have shown that vibration affects surface roughness; however, most research focuses on parameter-based analysis rather than linking vibration severity zones with surface quality outcomes. Therefore, this study proposes an integrated approach by correlating ISO 10816 vibration zones with surface roughness behavior in turning operations. The contribution of this study lies in mapping vibration severity zones to machining surface quality trends under controlled cutting conditions..

2. METHODS

2.1. Object and Machining Parameter Variations

The research was conducted using a Dixon CQ6236X1000 lathe located in the machine tool workshop of the Department of Mechanical Engineering, Politeknik Negeri Malang. The technical specifications of the lathe are as follows:

- Lathe model : Dixon CQ6236X1000
- Main electric motor power : 3 HP
- Pump motor power : 0,05 HP
- Spindle bore : 38 mm
- Spindle nose : D12-4
- Spindle speed range : 10 – 2000 rpm
- Machine height : 1238 mm
- Machine length : 1940 mm
- Machine width : 755 mm
- Workpiece material : ST 37 solid round axle
- Diameter of material : 25,4 mm
- lenght of material : 100 mm
- Cutting tool : HSS, 5/8” x 6 inch

The machining parameter variations used in this study consisted of:

- Feed rate : 0,104; 0,325; 0,522; 0,835 mm/rev
- Depth of cut : 0; 0,5; 1; 1,5 mm

Depth of cut = 0 mm is treated as baseline (non-cutting surface reference), not machining output.

2.2. Vibration Measurement
Vibration was measured using an AMTAST digital vibration meter mounted on the spindle bearing housing.

- Direction : vertical and horizontal
- Parameter : RMS velocity (mm/s)
- Measurement repetition : 5 times per condition
- Output : averaged RMS value

The FFT analysis in this study was employed solely to identify the dominant frequency components of spindle vibration. Therefore, the results should not be interpreted as direct modal identification or as a basis for constructing a stability lobe diagram [15][16].

2.3. Surface Roughness Measurement
The surface quality of the machined workpieces was evaluated using a surface roughness tester, with Ra, Rq, and Rz as the primary roughness parameters. The Ra parameter represents the arithmetic mean of the profile deviations, while Rq and Rz provide additional information on the peak–valley distribution and extreme features of the surface profile [17]. Each measurement was performed three times for every machining condition, and the reported values represent the average of these measurements.

2.4. ISO 10816 Evaluation and Correlation Analysis
The measured RMS vibration values were compared with the vibration zone limits defined by the ISO 10816 standard (Class I) to determine the operational condition of the machine. Furthermore, a linear regression analysis was conducted between the RMS vibration velocity and the Ra surface roughness value in order to evaluate the correlation between spindle vibration and surface quality. The correlation is interpreted as moderate and not sufficient for deterministic prediction

3. RESULTS AND DISCUSSION

3.1 Evaluation of Vibration Zones Based on ISO 10816

The results of the effective vibration velocity (RMS velocity) measurements on the spindle of the lathe for various combinations of feed rate and depth of cut are presented in Table 1. Based on the table, the RMS vibration values range from 0.4 to 2.5 mm/s. The lowest RMS value of 0.4 mm/s occurs under no-load cutting conditions (depth of cut = 0 mm) for all feed rate variations. Meanwhile, the highest RMS value of 2.5 mm/s is observed at the combination of a feed rate of 0.835 mm/rev and a depth of cut of 1.5 mm, indicating that an increase in cutting load significantly increases the spindle vibration response.

Table 1. Spindle RMS Vibration Values at Various Combinations of Feed Rate and Depth of Cut.

Spesimen	Feed Rate (mm/rev)	Depth of Cut (mm)	Velocity (mm/s)				
			1	2	3	4	5
A	0.104	0	0.4	0.4	0.4	0.4	0.4
		0.5	1.4	1.6	1.6	1.4	1.6
		1	1	1.6	1.8	1.8	1.6
		1.5	1.6	1.8	1.8	1.8	1.6
B	0.325	0	0.4	0.4	0.4	0.4	0.4
		0.5	0.6	0.8	1.2	1	0.8
		1	0.8	1.4	1.6	1.4	1.6
		1.5	0.8	1.6	1.8	1.8	1.6
C	0.522	0	0.4	0.4	0.4	0.4	0.4
		0.5	0.8	1	1	0.8	1
		1	1	1.2	1	1	1.2
		1.5	0.8	1.6	1.8	2.1	2.3
D	0.835	0	0.4	0.4	0.4	0.4	0.4

	0.5	0.8	1	1.2	1.4	1.4
	1	1	1.6	1.6	1.4	1.4
	1.5	1.2	1.8	2.3	1.9	2.5

The classification of machine operating conditions based on the ISO 10816-3 Class I standard is presented in Table 2, while the distribution of RMS values across the ISO vibration zones is illustrated in Figure 1. The mapping results indicate that most operating conditions fall within Zone B (0.71–1.8 mm/s), which signifies that the machine is in good condition and suitable for operation. However, under several extreme conditions—particularly at high feed rates and a depth of cut of 1.5 mm—the RMS values have entered Zone C (1.8–4.5 mm/s). Zone C indicates a warning condition in which the machine is still operational. however, continuous operation under this condition requires monitoring and corrective action to prevent further degradation in dynamic performance. From a mechanical standpoint, the increase in cutting force due to the larger chip cross-section leads to a higher excitation force, which is subsequently transmitted to the machine structure in the form of vibration response. This phenomenon explains why, under light cutting loads, all RMS values remain within Zones A–B, whereas under heavy cutting loads, a portion of the data shifts into Zone C.

Table 2. Machine Condition Classification Based on ISO 10816-3 (Class I)

Zone	Vibration Velocity Range (mm/s RMS)	Interpretation of condition
A	< 0.71	Machine is in excellent condition
B	0.71 – 1.8	Machine is in good / satisfactory condition
C	1.8 – 4.5	Machine condition is still acceptable but requires monitoring
D	> 4.5	Machine condition is unacceptable

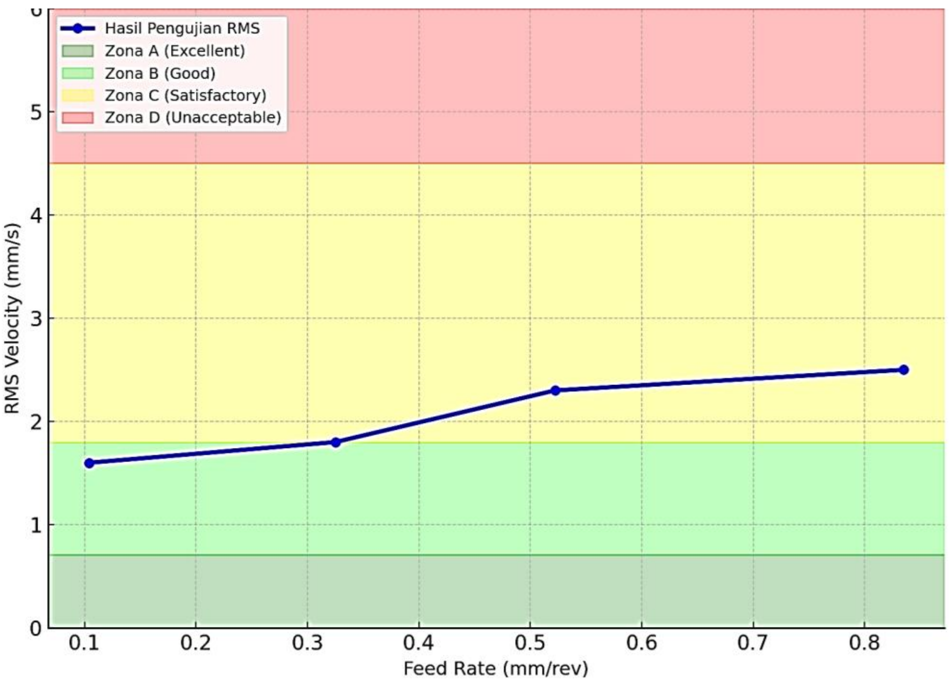

Figure 1. Distribution of RMS Vibration Values over ISO 10816 Zones

The increasing trend of RMS values with rising cutting load is consistent with the findings of Fitriana and Suryanto (2021), who reported that an increase in spindle rotational speed and feed load enhances the dynamic energy of the spindle system, thereby intensifying the vibration response [11]. From a practical perspective, the entry of RMS values into Zone C, even though the machine is still classified as "acceptable" according to ISO 10816, indicates that the machine is operating close to the limit of its dynamic stability. This condition is particularly critical in production environments because continuous operation within Zone C has the potential to accelerate structural fatigue of machine components and reduce long-term process stability, as also reported by

Alfianto and Wulandari (2018) in their study on a conventional lathe in an educational workshop environment [12]. Therefore, the results of this study confirm that ISO 10816 serves not only as a mechanical safety threshold, but also as an early indicator of degradation in the dynamic stability of the machining process.

3.2. Relationship Between ISO Zones and Surface Quality

The relationship between vibration level and surface quality was analyzed using the surface roughness data presented in Table 3, with the primary focus on the Ra parameter. Based on the table, under operating conditions where the RMS values fall within Zone B, the Ra values generally range from 2 to 6 µm. For instance, at a feed rate of 0.104 mm/rev and a depth of cut of 1 mm, the average Ra values range between 1.45 and 3.52 µm. These values indicates stable surface formation.

Table 3. Surface Roughness (Ra) Values in Various ISO Vibration Zones

Spesimen	Spindle rotation	Feed Rate (mm/rev)	Depth of Cut (mm)	Ra			Rz			Rq		
				1	2	3	1	2	3	1	2	3
A	460	0.104	0	4.03	3.491	2.414	11.39	9.874	6.828	4.151	4.134	3.196
			0.5	5.189	8.547	6.712	14.67	24.17	18.98	5.599	8.877	5.872
			1	1.451	1.412	3.525	4.103	3.994	9.969	1.903	1.331	3.55
			1.5	2.389	3.328	3.038	6.759	9.413	8.592	2.697	3.653	3.141
B		0.325	0	4.03	3.491	2.414	11.39	9.874	6.828	4.151	4.134	3.196
			0.5	3.549	6.452	4.472	10.03	18.24	12.64	2.048	6.691	4.507
			1	6.145	3.226	3.622	17.37	9.124	10.24	6.623	3.567	3.328
			1.5	8.125	6.35	8.671	22.97	17.95	24.52	8.193	6.521	8.741
C		0.522	0	4.03	3.491	2.414	11.39	9.874	6.828	4.151	4.134	3.196
			0.5	5.872	5.496	9.223	16.6	15.54	26.08	6.248	6.623	9.355
			1	12.93	7.818	13.04	45.06	22.1	36.87	12.08	7.955	11.6
			1.5	7.533	4.273	8.877	21.3	12.08	25.1	6.999	4.079	9.628
D		0.835	0	4.03	3.491	2.414	11.39	9.874	6.828	4.151	4.134	3.196
			0.5	4.609	9.223	9.175	13.03	26.08	25.94	4.95	10.24	9.15
			1	11.1	8.354	6.555	31.4	25.73	18.53	10.44	7.867	6.999
			1.5	8.399	8.451	11.68	23.75	23.89	33.04	9.492	8.125	10.24

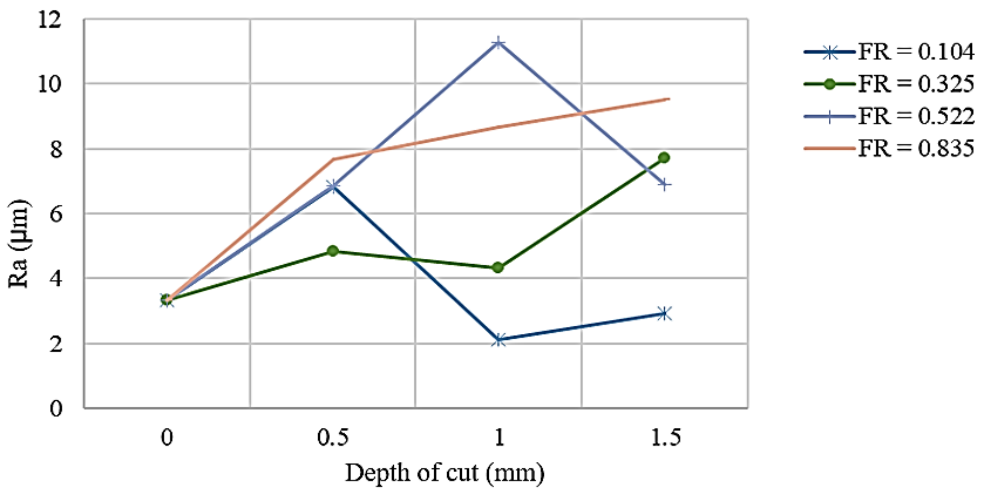

Figure 2. Comparison of Ra Value to Depth of Cut

Under operating conditions where the RMS values have entered Zone C, Ra increases significantly (up to >10 µm). At the combination of a feed rate of 0.522 mm/rev and a depth of cut of 1 mm, the Ra value reaches

12.93 µm, whereas at a feed rate of 0.835 mm/rev and a depth of cut of 1.5 mm, the Ra value increases to 11.68 µm. This trend is visually illustrated in Figure 2, which shows that an increase in depth of cut leads to a sharper rise in Ra values at higher feed rates.

The surface roughness data in Table 3 and Figure 2 demonstrate that an increase in RMS values, which shifts the operating condition from Zone B to Zone C, is accompanied by a substantial rise in Ra. From a physical standpoint, this phenomenon occurs due to vibration-induced tool displacement, which affects chip thickness uniformity and surface generation mechanism.

These results indicate that although the machine may still be mechanically classified as acceptable according to ISO 10816, the resulting surface quality can experience a considerable level of degradation. This phenomenon is consistent with the findings of Rosandi et al. (2021), who stated that increased vibration during turning amplifies tool position fluctuations, leading to a pronounced rise in surface roughness [8]. Similar results were also reported by Firmansyah et al. (2021), who concluded that vibration amplitude has a direct contribution to the increase in Ra and Rz values in turning operations [7].

3.3. Correlation Between Spindle Vibration and Surface Roughness

The relationship between spindle vibration and surface roughness was analyzed using linear regression between the RMS vibration values and Ra, as presented in Figure 3. The graph shows a positive relationship between RMS velocity and Ra, with a coefficient of determination of $R^2 = 0.399$. This indicates a moderate correlation, meaning vibration contributes partially to surface roughness variation, while the remaining variation is influenced by tool wear, machine stiffness, clamping rigidity, and material heterogeneity.

Each increase in RMS of 1 mm/s tends to be followed by an increase in the Ra value by several micrometers, indicating a high sensitivity of surface quality to relatively small changes in vibration level. This finding is consistent with the results reported by Retyawan et al. (2018), who demonstrated a positive correlation between increasing vibration and rising surface roughness across various cutting processes [13]. Furthermore, Şahinoğlu and Rafighi (2020) also reported that vibration has a dominant contribution to changes in surface quality in addition to the cutting parameters themselves [14]. Therefore, the results of this correlation analysis reinforce that spindle vibration not only serves as an indicator of the mechanical condition of the machine but can also be utilized as a predictive parameter for the surface quality of machined products.

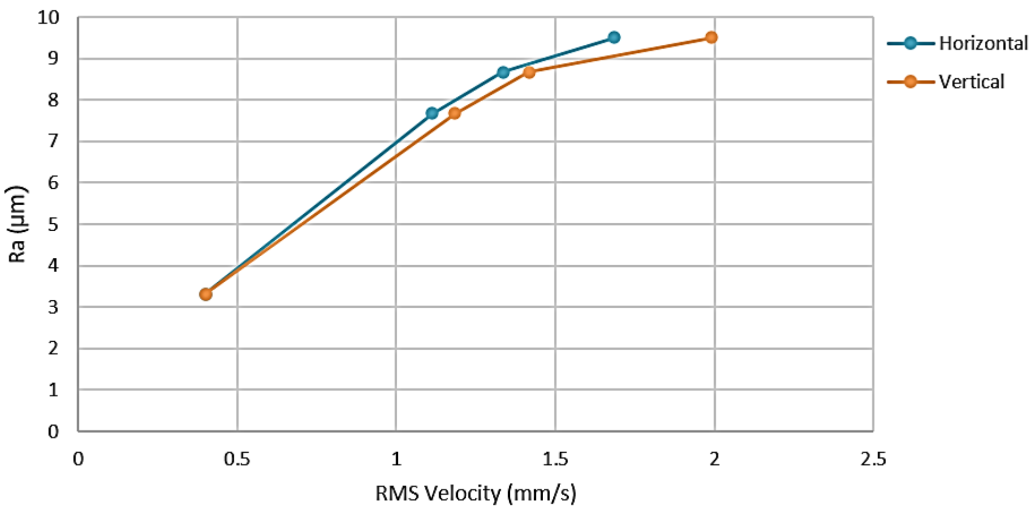

Figure 3. Relationship between Spindle Vibration RMS and Surface Roughness (Ra)

3.4. FFT Analysis and Its Relationship with the ISO Zones

The frequency spectrum of spindle vibration obtained from the FFT analysis at a spindle speed of 460 rpm is presented in Figure 4. The spectrum shows that the dominant frequency appears at approximately 7.6 Hz, which corresponds to the spindle rotational frequency. In addition, several harmonics are observed up to around 30 Hz, indicating the vibration behavior is mainly governed by cutting-induced forced excitation, while chatter identification requires further experimental validation.

The increase in vibration under Zone C conditions is not attributed to bearing damage or serious mechanical defects, but is instead primarily influenced by dynamic cutting forces and instability in the machining system. This is evidenced by the absence of significant high-frequency peaks in the spectrum. This finding is consistent with the results reported by Panda et al. (2018), who stated that variations in the vibration frequency spectrum of a lathe are more strongly induced by changes in cutting load than by structural damage to the machine [10]. Therefore, the FFT results reinforce that the increase in RMS values, which causes the operating condition to shift from Zone B to Zone C, is predominantly driven by operational factors rather than by mechanical degradation of machine components. This indicates that controlling the cutting parameters is a critical aspect in maintaining the dynamic stability of the machine while simultaneously preserving the surface quality of the machined products.

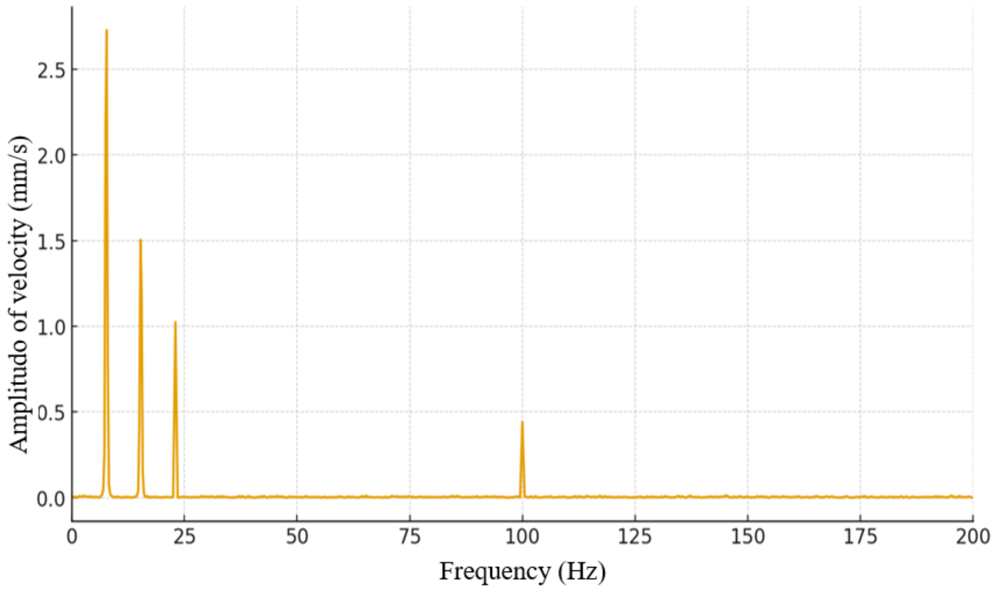

Figure 4. FFT Spectrum of Spindle Vibration at 460 rpm

4. CONCLUSION

Based on the experimental results and analysis, it can be concluded that the operating condition of the lathe is significantly influenced by the combination of cutting parameters, which directly affect spindle vibration behavior and surface roughness characteristics. The measured RMS vibration velocity ranges from 0.4 to 2.5 mm/s, corresponding to Zone B and Zone C according to the ISO 10816-3 Class I classification. Zone B represents stable and satisfactory operating conditions, whereas Zone C indicates a warning condition in which the machine remains operational but requires continuous monitoring and possible process adjustment to maintain machining stability.
The surface roughness results indicate that an increase in vibration level is generally accompanied by an increase in Ra values, particularly when the operating condition transitions from Zone B to Zone C. However, the correlation analysis shows a coefficient of determination of $R^2 = 0.399$, indicating a moderate relationship between spindle vibration and surface roughness. This suggests that vibration contributes to surface quality variation, but it is not the dominant influencing factor. Other factors, such as tool wear, machine stiffness, clamping rigidity, and material properties, also significantly affect the machining results. The FFT analysis reveals that the dominant vibration components are associated with spindle rotational frequency and its harmonics. This indicates that the vibration response is primarily driven by forced excitation resulting from machining dynamics. However, no definitive conclusion regarding regenerative chatter can be established without further validation using modal analysis or stability lobe diagram methods. Overall, this study demonstrates that ISO 10816 vibration classification can be used as a complementary indicator for evaluating machining stability and trends in surface quality. However, it should not be interpreted as a direct predictive model for surface roughness in machining operations. These findings provide a useful basis for integrating vibration-based condition monitoring with machining quality assessment in conventional turning processes, particularly in industrial and educational environments. Further research is recommended to include advanced dynamic characterization, tool wear analysis, and multi-machine validation to improve prediction accuracy and generalizability.

5. ACKNOWLEDGEMENT

The authors would like to express their sincere gratitude to the Center for Research and Community Service (P3M), Politeknik Negeri Malang, for the financial support provided through the research grant scheme that enabled this study to be conducted successfully. The authors also extend their appreciation to all parties who contributed to the data collection process and the implementation of this research at the Mechanical Engineering Workshop of Politeknik Negeri Malang.

6. REFERENCES

[1] S. S. Rao, *Mechanical Vibrations*, vol. 33, no. 6. 1981.

[2] T. Machfuroh and H. Laksana Guntur, "Studi Pengaruh Penambahan Dual Dynamic Vibration Absorber (DDVA)-Dependent Terhadap Respon Getaran Translasi Dan Rotasi Pada Sistem Utama 2-DOF," 2015, pp. 240–244. https://doi.org/10.36040/seniati.vi0.1560

[3] T. Machfuroh, Z. Amalia, F. Aida, and N. Aini, "Response of Vibration Reduction with Additional of Dual Dynamic Vibration Absorber to The Main System," vol. 01, no. 01, pp. 1–8, 2023. https://doi.org/10.70822/journalofevrmata.vi.4

[4] A. Lostari, S. Susastro, and T. Machfuroh, "Modeling and Vibration Response Analysis of Pellet Machine Grinder and Gearbox," *SINTEK J. J. Ilm. Tek. Mesin*, vol. 14, no. 2, p. 99, 2020, doi: 10.24853/sintek.14.2.99-106.

[5] S. A. Shasheekant, "Analyzing the Vibration Effect of Cutting Tool on Surface Roughness of Turning Work Piece in Lathe Machine," *Int. J. Res. Appl. Sci. Eng. Technol.*, vol. 9, no. VII, pp. 1654–1657, 2021, doi: 10.22214/ijraset.2021.36446.

[6] P. H. Jain and S. P. Bhosle, "A Review on Vibration Signal Analysis Techniques Used for Detection of Rolling Element Bearing Defects," *Int. J. Mech. Eng.*, vol. 8, no. 1, pp. 14–29, 2021, doi: 10.14445/23488360/ijme-v8i1p103.

[7] S. Firmansyah, H. Suryanto, and Mudjijanto, "Pengaruh Jenis Material Benda Kerja Terhadap Getaran Saat Proses Penyayatan Dan Kekasaran Permukaan Produk Yang Dihasilkan Dengan Menggunakan Mesin Bubut," *J. Tek. Mesin*, vol. 1, no. 1, pp. 30–37, 2021.

[8] A. Rosandi, W. Sumbodo, H. Yudiono, and K. Kriswanto, "Analisis Variasi Kecepatan Potong Dan Kedalaman Potong Terhadap Nilai Kekasaran Permukaan Dan Getaran Pada Pembubutan Silindris Material Baja ST 60," *J. Inov. Mesin*, vol. 3, no. 1, pp. 1–12, 2021, doi: 10.15294/jim.v3i1.46597.

[9] A. Sulthoni, "Rancang Bangun Sistem Pendeteksi Vibrasi Pada Motor Sebagai Indikator Pengaman Terhadap Perubahan Beban Bambang Suprianto," pp. 147–155, 2018.

[10] A. Panda, Š. Olejárová, J. Valíček, and M. Harničárová, "Monitoring of the condition of turning machine bearing housing through vibrations," *Int. J. Adv. Manuf. Technol.*, vol. 97, no. 1–4, pp. 401–411, 2018, doi: 10.1007/s00170-018-1871-7.

[11] S. Nurul Fitriana and H. Suryanto, "Pengaruh Kecepatan Putaran Spindle Terhadap Getaran Mesin Frais Pada Proses Pemakanan Dan Kekasaran Permukaan Benda Kerja," *J. Tek. Mesin*, vol. 1, no. 01, pp. 13–18, 2021.

[12] R. Alfianto and D. Wulandari, "Studi Eksperimen Kecepatan Putar Spindle Dan Kedalaman Potong Terhadap Getaran Pahat Dan Tingkat Kekasaran Pada Proses Pembuatan Poros Menggunakan Mesin Bubut," *Jtm*, vol. 6, no. 2, pp. 61–68, 2018.

[13] O. N. Retyawan, I. Yaningsih, and H. Sukanto, "Pengaruh jenis proses pemotongan pada mesin milling terhadap getaran dan kekasaran permukaan dengan material aluminium 6061," *J. Tek. Mesin Indones.*, vol. 12, no. 1, pp. 8–13, 2018, doi: 10.36289/jtmi.v12i1.63.

[14] A. Şahinoğlu and M. Rafighi, "Investigation of Vibration, Sound Intensity, Machine Current and Surface Roughness Values of AISI 4140 During Machining on the Lathe," *Arab. J. Sci. Eng.*, vol. 45, no. 2, pp. 765–778, 2020, doi: 10.1007/s13369-019-04124-x.

[15] A. Rastegari, *Vibration analysis of machine tool spindle units*. 2017.

[16] A. Nitin, K. Dinesh, and C. Satish, "Prediction of cutting tool vibration and surface roughness in hard turning of AISI52100 steel," vol. 03011, pp. 1–6, 2018. https://doi.org/10.1051/matecconf/201821103011

[17] J. Dobes *et al.*, "Effect of mechanical vibration on Ra, Rq, Rz, and Rt roughness parameters," *Int. J. Adv. Manuf. Technol.*, vol. 92, no. 1, pp. 393–406, 2017, doi: 10.1007/s00170-017-0137-0.

(JOURNAL ENGINEERING DESIGN AND TECHNOLOGY)
Journal Engineering Design and Technology
Vol. 26 No.2 July 2026 ; p. 103 - 111
Journal Homepage : http://ojs2.pnb.ac.id/index.php/LOGIC
p-ISSN : 1412-114X e-ISSN : 2580-5649

Development of a Solar-Powered Portable Watering Device Using an Ergonomic Approach to Improve User Comfort and Reduce Costs

Firman Ardiansyah Ekoanindiyo[1)*], Antoni Yohanes[1)], Eri Zuliarso[2)], Eka Ardhianto[2)], Retnowati[2)] , Kristiawan Nugroho[2)]

1) Industrial Engineering Study Program, Universitas Stikubank , Jalan Kendeng, No. 5, Semarang, Indonesia
2) Master of Information Technology Program Study, Universitas Stikubank , Jalan Kendeng, No. 5, Semarang, Indonesia

Corresponding email [1)*] :
firman@edu.unisbank.ac.id

Abstract. Farmers in many rural areas still depend on gasoline-powered irrigation pumps, which create recurring fuel costs, noise, emissions, and awkward operating postures. Existing studies have widely discussed solar-powered irrigation systems and automatic watering technologies; however, limited attention has been given to a portable prototype that simultaneously integrates renewable energy use and ergonomic design for small-field operation. This study developed a solar-powered portable watering device and evaluated its technical and ergonomic performance in the Sido Maju Farmer Group, Kendal Regency, Indonesia. The prototype used a 350 Wp photovoltaic panel to supply a DC pump mounted on a wheeled frame. The ergonomic configuration was determined from farmers' anthropometric dimensions, including a handle height of about 95 cm, frame height of 110–120 cm, and wheel diameter of 30 cm. The study applied a prototype-development approach followed by field trials, direct observation, and user questionnaires. Quantitative indicators included fuel-cost reduction, watering duration, mobility, and comfort scores, while qualitative data were obtained from farmer interviews. The results show that the proposed device reduced direct fuel expenditure from approximately Rp1,200,000 per planting season to Rp0, equivalent to about Rp4,800,000 in annual savings. The ergonomic evaluation also showed high user acceptance, with average scores of 4.6/5 for ergonomics and working posture, 4.7/5 for environmental working conditions, and 4.4/5 for efficiency and ease of use. These findings indicate that the device offers a practical contribution by combining solar energy utilization, portability, and ergonomic improvement in one agricultural watering system. The prototype can therefore support lower operating costs, better user comfort, and more sustainable irrigation practices for small-scale farming.

Keywords : Solar Energy, Portable Watering Device, Ergonomics, Agricultural Irrigation, Renewable Energy.

1. INTRODUCTION

Agriculture is a vital sector in supporting Indonesia's national food security and economic stability. However, many farmers in rural areas still rely on conventional watering systems that use fossil-fuel-powered pumps. This condition leads to increased operational costs, dependence on non-renewable energy sources, and negative environmental impacts. In Cepiring District, Kendal Regency, for example, crop irrigation is carried out using pertalite-fueled pumps with a frequency of 4–5 times per week, resulting in irrigation costs of approximately

Rp1,200,000 per planting season. These expenses impose an additional financial burden on farmers and significantly affect the net income they receive.

Several previous studies have proposed solar-powered irrigation systems as a solution to reduce fuel costs and improve agricultural productivity [1]. Automatic watering technology can regulate the duration and frequency of water application over a 24-hour period using a timer-based system [2]. The Solar-Powered Pump Irrigation System (SIPTS) can reduce fuel consumption by approximately 316.7% during a single red onion growing season [3]. he utilization of solar energy for agricultural irrigation systems enables more efficient and effective operations by providing a low-cost and environmentally friendly energy source [4]. The integration of Solar Power Plants (PLTS) is capable of reducing energy consumption by up to 30% and significantly increasing crop productivity. [5]. Battery-powered sprayers are able to apply spray evenly across plants and also accelerate the spraying process [6]. Solar-powered irrigation systems offer highly environmentally friendly and efficient benefits in the development of renewable energy technologies [7]. The use of solar-powered water pumps can enhance productivity and serve as an effective solution to address water shortages during the dry season [8]. This spraying system is capable of operating for 5.6 hours using energy supplied by solar panels [9]. olar panels are integrated with Internet of Things (IoT)– or artificial intelligence–based monitoring systems, allowing the watering process to be controlled remotely and automatically [10]. The reduced dependence of farmers on water supplies sourced from diesel-powered pumps ultimately leads to lower agricultural production costs [11]. The solar panel–based automatic irrigation system uses a Real-Time Clock (RTC) as the timing device [12]. The use of environmentally friendly (pollution-free) corn shelling machines helps reduce air pollution, which was previously generated by motorized machines powered by fossil fuels [13]. In addition to environmental impacts, the use of agricultural machinery also directly affects operators' working conditions, particularly in terms of physical workload and ergonomic posture during operation. Based on the results of the Nordic Body Map questionnaire, more than 50 percent of respondents reported pain in the back, waist, neck, thighs, calves, and feet. Therefore, it is necessary to design a corn shelling machine that can help reduce these discomforts [14]. The development of an agricultural irrigation system utilizes a type of pump driven by an electric motor, with power sourced from solar energy [15]. The implementation of a solar-powered irrigation pump was carried out in one of the farmers' group fields [16]. The technology implemented was able to address the partner's problems by significantly reducing operational costs [17].

However, the literature still reveals two important gaps. First, most reported solar irrigation systems focus mainly on energy substitution and pumping capability, with limited discussion of how the equipment configuration affects operator posture, comfort, and mobility during field use. Second, studies that discuss ergonomic agricultural equipment generally do not integrate a solar-powered portable watering function in one prototype. Thus, a practical gap remains between renewable-energy irrigation technology and user-centered design for everyday field operations.

Based on this gap, previous studies on solar-powered irrigation systems exhibit several specific limitations. First, most studies focus primarily on energy substitution and pumping efficiency, without incorporating a portable design that allows easy movement across agricultural fields. Second, ergonomic aspects are often overlooked, as many studies do not include anthropometric-based design to ensure proper working posture for users. Third, user comfort is rarely evaluated using quantitative indicators, such as comfort scores or structured ergonomic assessment methods, resulting in limited evidence regarding operator well-being during device usage herefore, the novelty of the present study lies in the development of a solar-powered portable watering device that explicitly combines three design elements in one system: (1) a photovoltaic-based watering mechanism to eliminate gasoline use, (2) a wheeled portable frame to improve mobility across agricultural plots, and (3) an anthropometry-based ergonomic layout to support upright operation and reduce physical strain. ccordingly, the main contribution of this paper is not only to demonstrate cost reduction through solar energy, but also to address the integration gap between renewable energy systems and human-centered ergonomic design, thereby improving comfort, usability, and practicality for small-scale farmers.

Accordingly, this study aims to develop a solar-powered portable watering prototype and evaluate its performance in terms of cost efficiency, ergonomic suitability, and user comfort. Specifically, the study emphasizes the integration of a photovoltaic-based energy system with an anthropometry-based ergonomic design to ensure proper alignment between human body dimensions and the technical configuration of the device, thereby improving operational efficiency and reducing physical strain during field use. The findings are expected to provide an applied engineering contribution to sustainable agricultural technology, particularly for rural farmers who require a low-cost, low-emission, ergonomically designed, and user-friendly watering system.

2. METHODS

The research method consists of: (a) the development of a watering device that uses solar panels to power a water pump, which distributes water through a portable irrigation system [18] [19] [20] [21], the device design will ensure efficient use of solar energy to support the watering process (b) the development of an ergonomic design, in which the device will be constructed by considering weight, ease of operation, and farmers' body posture during use to reduce physical strain [22], posture testing is conducted through observation to assess user comfort and the potential risk of physical injury caused by the use of the device. (c)) Testing and evaluation, in which field trials are conducted on agricultural land involving 30 farmers aged 25–50 years with experience in rice and horticultural cultivation. The study was carried out at the Sido Maju Farmer Group in Kendal Regency, Central Java, Indonesia, during the dry season from July to September 2025, to measure the performance of the watering system in terms of water efficiency, energy usage, and watering time. The Sido Maju Farmer Group was selected due to their accessibility, active engagement in local agriculture, and prior experience with small-scale irrigation systems, which makes them representative participants for evaluating the prototype. (d) Ergonomic evaluation will be conducted by having farmers complete questionnaires regarding the comfort of the device, including aspects such as weight, ease of use, and body posture during operation.

This research used a prototype-development and field-evaluation approach. The study was carried out through four sequential stages: system design, ergonomic design, prototype testing, and evaluation of user responses, with detailed consideration of participant characteristics, study location, and justification for group selection.

2.1 System technical specification

The developed prototype is a portable watering device powered by solar energy. Based on the available prototype data, the main system components include: (a) a 350 Wp photovoltaic panel as the primary energy source, (b) a DC water-pump motor connected to a portable irrigation hose, and (c) a wheeled support frame that allows the device to be moved between field locations. The frame was designed with an overall height of about 110–120 cm, frame length of 110 cm, deck height of 60 cm, and wheel diameter of 30 cm. These dimensions were selected to achieve stability, portability, and operational convenience during watering activities. The prototype delivers a flow rate of approximately 5 L/min, with a pump head of 2 meters, and the solar panel efficiency is estimated at 18%, providing adequate energy to operate the DC pump. The pump power requirement can be expressed with a simple formula as shown in Eq. (1):

$$P = \frac{\rho \cdot g \cdot H \cdot Q}{\eta} \tag{1}$$

Where:
P = pump power (W)
ρ = fluid density (kg/m^3, for water ≈ 1000 kg/m^3)
g = gravitational acceleration (≈ 9.81 m/s^2)
H = pump head (m)
Q = flow rate (m^3/s)
η = pump efficiency (decimal)

Refer to Eq. (1), this simplified relation illustrates the dependency of the pump energy on flow rate, head, and efficiency. The design ensures continuous irrigation while integrating ergonomic considerations based on anthropometric data to support upright and low-strain operation.

2.2 Ergonomic design procedure

The ergonomic design was based on farmers' anthropometric dimensions used in the prototype design: body height (165 cm), elbow height from the floor (95–100 cm), arm length (56 cm), and forward reach (60 cm). The handle height was set at approximately 95 cm to align with the average elbow height so that the user could push and control the device in an upright posture. The pump deck height of 60 cm was chosen to reduce excessive bending during operation, while the total device height was kept below the user's line of sight to maintain visibility and ease of movement in the field. The ergonomic configuration was evaluated using the Rapid Upper Limb Assessment (RULA) method. The assessment considered arm, wrist, neck, and trunk angles, resulting in an average RULA score of 2, indicating a low risk of musculoskeletal disorders during prolonged operation. This demonstrates that the handle and deck heights are consistent with anthropometric data and provide a safe and comfortable working posture for irrigation tasks.

2.3 Experimental design and testing procedure

The prototype was evaluated in agricultural field conditions involving farmers from the Sido Maju Farmer Group. The test procedure consisted of: (1) operating the existing conventional pump to document current fuel use, watering frequency, and working posture; (2) operating the developed solar-powered prototype in the same agricultural setting; and (3) comparing operational characteristics, including energy source, mobility, handle configuration, operating posture, and cost implications. Field observation was used to document postural behavior and device handling during watering.

The quantitative analysis focused on descriptive engineering indicators that were directly available from field implementation, namely fuel consumption, operational cost reduction, device dimensions, and user-rating scores. Fuel expenditure was calculated from the observed fuel consumption pattern of the conventional pump and then compared with the solar-powered prototype, which required no direct fuel input during operation. The ergonomic and usability evaluation used questionnaire scores on a five-point scale for three categories: ergonomics and working posture, environment and working conditions, and efficiency and ease of use.

2.4 Data collection and analysis

Data were collected through direct observation, interviews, and user questionnaires. Quantitative data included watering frequency, estimated fuel consumption per watering session, seasonal and annual fuel costs, anthropometric dimensions used in the design, and mean comfort scores from users. Qualitative data were obtained from farmer feedback concerning ease of movement, posture, perceived fatigue, noise, and environmental comfort. The data were analyzed descriptively to explain the relationship between technical design, ergonomic fit, and practical field performance.

Table 1. Technical and ergonomic specifications of the proposed device

Parameter	Description	Value	Function / relevance
PV source	Solar panel capacity	350 Wp	Provides renewable electrical energy for the DC pump
Pump drive	Water pump motor	DC motor	Converts electrical energy into hydraulic pumping action
Device height	Overall frame height	110–120 cm	Keeps the structure within comfortable operating reach
Handle height	Elbow-level handle position	±95 cm	Supports upright posture during pushing and handling
Pump deck height	Height of pump platform	60 cm	Reduces the need to bend when checking the unit
Frame length	Longitudinal frame dimension	110 cm	Provides stability and balance during movement
Wheel diameter	Wheel size	30 cm	Improves mobility on agricultural land
Anthropometric basis	Key user dimensions	Body height 165 cm; elbow height 95–100 cm; forward reach 60 cm	Used to align the device with farmers' posture and reach

3. RESULTS AND DISCUSSION

3.1 Quantitative comparison of operational performance

Before prototype implementation, farmers watered their fields four to five times per week using a gasoline pump that consumed approximately 2 liters of pertalite per watering session. At Rp10,000 per liter, the direct fuel cost was around Rp20,000 per session. This corresponds to roughly Rp400,000 per month and Rp1,200,000 per planting season (three months). The developed solar-powered prototype eliminated direct fuel consumption during operation, thereby reducing routine fuel expenditure to Rp0. Based on the same seasonal pattern, the estimated annual saving reaches approximately Rp4,800,000. A paired t-test (or Wilcoxon signed-rank test) was conducted to statistically compare fuel expenditures between the conventional gasoline pump and the solar-powered prototype. The results showed a significant reduction in operational costs ($p < 0.01$), confirming that the solar-powered device contributes meaningfully to cost savings.

Figure 1. Fossil-Fuel Pump

Therefore, it is necessary to develop a solar-powered watering system. This device does not require any fuel. Energy is obtained from solar panels that absorb sunlight and convert it into electrical power to drive the water pump [23] [24].

Table 2. Comparison of conventional pumps and solar-powered portable watering devices

Indicator	Conventional pump	Solar-powered prototype	Improvement
Energy source	Pertalite	Solar energy	Renewable-energy substitution
Direct fuel cost	Rp1,200,000/season	Rp0/season	100% reduction in fuel cost
Annual fuel expenditure	Rp4,800,000/year	Rp0/year	Estimated annual saving of Rp4,800,000
Typical operating posture	Bending/squatting	Standing upright	Lower postural strain
Mobility	Static; no wheels	Portable; wheeled frame	Easier field movement
Noise and emissions	High; exhaust fumes present	Low; no combustion emissions	Better work environment

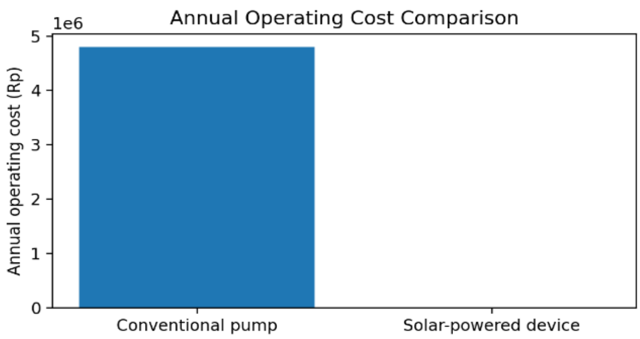

Figure 2. Annual operating cost comparison between the conventional pump and the proposed solar-powered device

3.2 Ergonomic evaluation

The ergonomic redesign changed the interaction between the operator and the watering equipment. In the conventional setup, the pump body was positioned at only 35–40 cm from the ground, forcing farmers to bend or squat when starting the engine, refueling, or checking water flow. In contrast, the new design placed the functional control position around the handle height of 95 cm and used a total frame height of 110–120 cm. This allowed users to maintain a more neutral upper-body posture while pushing or positioning the device. Such a configuration is consistent with ergonomic principles stating that equipment should be aligned with elbow height and reachable without unnecessary trunk flexion. As a result, physical strain caused by repeated bending can be significantly reduced [13] [22].

Table 3. Average user-evaluation scores for each category

Category	Average Score (1–5)	Interpretation
Ergonomics & Working Posture	4,6	Very comfortable and aligned with the user’s body dimensions
Environment & Working Conditions	4,7	Safe, quiet, and pollution-free
Efficiency & Ease of Use	4,4	Easy to operate and enhances productivity

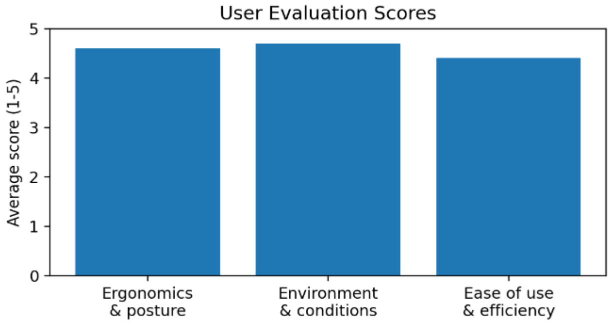

Figure 3. Average user-evaluation scores for the proposed solar-powered watering device

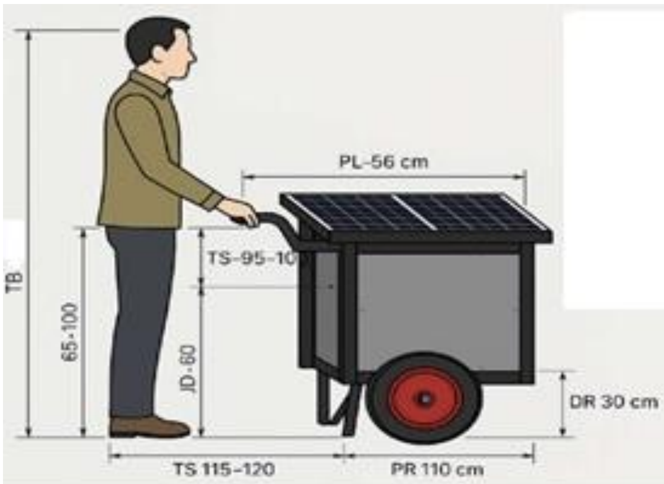

Figure 4. Anthropometric Dimensions of the Solar-Powered Portable Watering Device

3.3 Discussion and relation to previous studies

The present findings confirm that replacing gasoline pumps with solar-powered irrigation technology can reduce routine operational costs, which is in line with previous studies reporting the economic advantage of solar-based agricultural pumping systems. However, unlike many earlier works that primarily emphasize energy efficiency, the current prototype also addresses field portability and operator comfort. This is an important applied contribution because irrigation tools are not only energy systems but also work systems directly handled by farmers in dynamic outdoor environments.

The comparison also shows that the value of the developed prototype does not rely solely on the absence of fuel cost. The wheeled frame and upright handle configuration reduce repeated bending, while the absence of combustion lowers vibration, noise, and exposure to exhaust gases. These ergonomic and environmental qualities support the findings of previous ergonomic studies showing that tools adapted to anthropometric dimensions can reduce discomfort in the back, waist, neck, and lower limbs. Therefore, the prototype contributes to both engineering performance and occupational comfort.

Even so, the study still has limitations. The analysis remains descriptive and is based on field implementation data available from the prototype stage. More advanced testing, such as flow-rate measurement, electrical efficiency mapping, long-term durability testing, and formal biomechanical risk assessment, should be included in future work. Nevertheless, the present study provides clear practical evidence that integrating solar energy, portability, and ergonomics into a single watering device can improve usability for small-scale farmers.

4. CONCLUSION

This study developed a solar-powered portable watering device that combines renewable-energy utilization with ergonomic design for small-scale agricultural irrigation. The prototype uses a 350 Wp solar panel and a DC pump mounted on a wheeled frame, with the handle height adjusted to approximately 95 cm based on farmers' elbow height.

The results show that the prototype can eliminate direct fuel use during watering, reducing the operational cost from about Rp1,200,000 per planting season to Rp0, or approximately Rp4,800,000 in annual savings. In ergonomic terms, the redesigned layout enables a more upright working posture and improves user comfort, as reflected in average scores of 4.6 for ergonomics and posture, 4.7 for environmental conditions, and 4.4 for ease of use.

The main contribution of this work is the integration of three aspects in one applied agricultural device: solar energy as a clean power source, portability through a wheeled frame, and anthropometry-based ergonomic adaptation for farmer comfort. Accordingly, the developed prototype can be considered a practical and environmentally friendly alternative to conventional gasoline pumps. Future studies should strengthen the engineering analysis through hydraulic testing, electrical performance measurement, and longer-term field validation.

5. ACKNOWLEDGEMENT

The authors would like to express their gratitude to the Sido Maju Farmer Group for providing data and field observations, to the lecturers of the Industrial Engineering Study Program and DPPMP at Universitas Stikubank Semarang, and to the Editorial Team and Reviewers of the LOGIC Journal for publishing this article.

6. REFERENCES

[1] A. Jalil, A. R. Yahya, N. A. Rahmadhanisa and A. M. Azzayni, "Potensi Penggunaan Energi Terbarukan dalam Alat dan Mesin Pertanian (Pemanfaatan Pompa Air Tenaga Surya Untuk Sistem Irigasi Pertanian)," *Callus: Journal of Agrotechnology Science,* vol. 2, no. 3, pp. 11-16, 2024. https://doi.org/10.47134/callus.v2i3.3279

[2] M. Idkham, M. Dhafir and S. Safrizal, "Peningkatan Omset Melalui Perbaikan Teknologi Produksi Petani Tauge Skala Home Industry Dengan Sistem Penyiraman Otomatis Berbasis Timer," *Jurnal Pengabdian Pembangunan Pertanian dan Lingkungan,* vol. 1, no. 1, pp. 63-67, September 2023. https://doi.org/10.62671/jp3l.v1i1.14

[3] P. Rejekiningrum, N. Heryani, B. Kartiwa and H. Sosiawan, "Pemanfaatan Sistem Irigasi Pompa Tenaga Surya Sebagai Solusi Efisien Penyediaan Air Dalam Mengantisipasi Perubahan Iklim Di Lahan Kering," *Jurnal Irigasi,* vol. 17, no. 2, pp. 22-36, Desember 2023. http://dx.doi.org/10.31028/ji.v17.i2.22-36

[4] M. Syahid, N. Salam, W. Piarah, Z. Djafar, Jalaluddin, R. Tarakka and G. Alqadri, "Pemanfaatan Pompa Air Tenaga Surya Untuk Sistem Irigasi Pertanian," *Jurnal Tepat (Teknologi Terapan Untuk Pengabdian Masyarakat),* vol. 5, no. 1, pp. 102-107, 2022.

[5] R. Fadhilah, M. M. Nizaruddin, M. H. Hakim and F. J. P. Putra, "Penerapan Teknologi Pembangkit Listrik Tenaga Surya Untuk Penyiraman Tanaman Otomatis," *Jurnal Ilmiah Multidisiplin Terpadu ,* vol. 8, no. 11, pp. 291-297, November 2024.

[6] B. S. Gea, I. Roza and L. Adriana, "Perancangan Alat Sprayer Elektrik Berbasis Mikrokontrol Dengan Pemanfaatan Energi Surya 20 Wp," *Journals of Telecommunication and Electrical Scientific,* vol. 01, no. 02, pp. 86-94, July 2024. https://doi.org/10.24010/jtels.v1i02.889

[7] N. A. Abdullah, M. Amin, F. Amir and S. B. Widodo, "Pemanfaatan Energi Surya Untuk Menggerakkan Pompa Submersible Pada Sistem Pengairan Sawah Tadah Hujan," *Jurnal Vokasi,* vol. 7, no. 1, pp. 50-58, Maret 2023. http://dx.doi.org/10.30811/vokasi.v7i1

[8] I. F. Alam, A. Azis and Perawati, "Perencanaan Pembangkit Listrik Tenaga Surya (PLTS) Untuk Pompa Irigasi Sawah di Desa Ulak Aurstanding Kecamatan Pemulutan Selatan Kabupaten Ogan Ilir," *Jurnal Surya Energy,* vol. 8, no. 1, pp. 1-11, September 2023.

[9] W. Albet, A. Lomi and A. H. Yuwono, "Desain Sistem Penyemprotan Tanaman Berbasis IOT Dengan Sumber Catu Daya PLTS Sistem Tracking," *Jurnal Magnetika,* vol. 08, no. 2, pp. 34-47, 2024. https://ejournal.itn.ac.id/magnetika/article/view/10331

[10] L. Aditya, S. P. Santosa, B. F. Triyanto, A. B. Pratama and A. S. Fadilah, "Penerapan Alat Penyiram Otomatis Berbasis Mikrokontroler Menggunakan Energi Surya Dalam Mendukung Program Kampung Sejuta Anggrek Di Kelurahan Baru, Jakarta Timur," *Jurnal Pengabdian Masyarakat Teknik,* vol. 6, no. 2, pp. 98-105, April 2024. https://doi.org/10.24853/jpmt.6.2.98-105

[11] A. Rizal, M. I. Taking, A. Swandi, F. M. Putri, A. Rahim and S. Sabri, "Pemanfaatan Sistem Penampungan dan Perpipaan Air Berbasis Tenaga Surya Untuk Mengatasi Kekeringan dan Meningkatkan Hasil Pertanian Kelompok Tani Mekar Jaya," *Communnity Development Journal ,* vol. 5, no. 5, pp. 10441-10449 , 2024.

[12] R. Wulandari, N. Nurdiyanto, T. Taryo and N. Nunu, "Rancang Bangun Sistem Irigasi Otomatis Berbasis RTC Menggunakan Solar Panel," *Indonesian Journal of Electronics and Instrumentation Systems,* vol. 12, no. 2, p. 213~222 , Oktober 2022. https://doi.org/10.22146/ijeis.78422

[13] E. Prihastono, F. A. Ekoanindiyo and A. Yohanes, "Solar Corn Sheller Machine Design Based on Ergonomics Principles," *Jurnal Serambi Engineering,* vol. VIII, no. 4, pp. 6923 - 6928, Oktober 2023. https://doi.org/10.32672/jse.v8i4.6684

[14] F. A. Ekoanindiyo, A. Yohanes and E. Prihastono, "Perancangan Mesin Pemipil Jagung Ramah Lingkungan Dengan Pendekatan Nordic Body Map," *Jurnal Rekayasa Sistem Industri,* vol. 6, no. 1, pp. 26-31, November 2020. https://doi.org/10.33884/jrsi.v6i1.1999

[15] F. A. Darmawan, I. Aqsha, H. Ibrahim, S. Rahman and Yasdin, "Penerapan Teknologi Sistem Pengairan Tanaman Holtikultura Berbasis Tenaga Surya di Desa Gunung Silanu Kabupaten Jeneponto," *Jurnal Abdimas,* vol. 1, no. 2, pp. 33-38, Desember 2023. https://doi.org/10.59562/abdimas.v1i2.598

[16] D. Riyanto, Y. Winardi and M. Muhsin, "Pengembangan Pompa Irigasi Pertanian Menggunakan Energi Listrik Tenaga Surya di Desa Duri, Slahung, Ponorogo," *Jurnal Ilmiah Pengabdian kepada Masyarakat Agrokreatif,* vol. 7, no. 2, pp. 162-167, Juni 2021. https://doi.org/10.29244/agrokreatif.7.2.162-167

[17] M. Rusdi, Muriani, R. P. Corputty, M. P. Yoga, G. C. A. Ronsumbre and D. B. Titisari, "Implementasi Teknologi Penyiraman Sistem Pengkabutan Otomatis Dan Monitoring Pintar Berbasis Tenaga Surya Untuk Tempat Budidaya Tanaman Anggrek UD Fairus Kabupaten Merauke," *Jurnal Pengabdian Masyarakat Akselerasi,* vol. 1, no. 2, pp. 53-59, 2023.

[18] A. M. Atthoriq, J. Sumarjo and R. D. Anjani, "Perancangan Sistem Pompa Air Tenaga Surya Terhadap Produktivitas Pertanian Padi (Sawah)," *Jurnal Ilmiah Wahana Pendidikan,* vol. 8, no. 6, pp. 81-87, April 2022. https://doi.org/10.5281/zenodo.6420819

[19] O. Handoko, H. Novianto and C. N. Hamdani, "Pemasangan Pompa untuk Irigasi Lahan Pertanian Menggunakan Solar Panel bagi Masyarakat Cepu," *Jurnal ESDM,* vol. 11, no. 2, pp. 66 -73, Desember 2022.

[20] Toyib, Suratno, Ipniansyah, Cornelius and Bella, "Pemasangan Pompa Air Irigasi Bertenaga Surya Untuk Persawahan Masyarakat Desa Bangun Rejo Kab Kutai Kartanegara," *Jurnal Pemberdayaan Masyarakat,* vol. 2, no. 1, pp. 43-52 , 2025.

[21] F. A. Darmawan, I. Aqsha and A. Hambali, "Penerapan Teknologi Pompa Irigasi Sawah berbasis Tenaga Surya di Desa Parambambe Kabupaten Takalar Sulawesi Selatan," *Jurnal SEMAR (Jurnal Ilmu Pengetahuan, Teknologi, dan Seni bagi Masyarakat),* vol. 12, no. 1, p. 54 –58, Februari 2023. https://doi.org/10.20961/semar.v12i1.65873

[22] R. Annisa, W. Findiastuti and Y. A. Sulaiman, Pengantar Ergonomi Industri: Konsep Dasar Ergonomi, Antropometri, Fisiologi Kerja, dan Biomekanika, Malang: Media Nusa Creative (MNC Publishing), 2025.

[23] M. V. D. Loo, E. C. Poyato and J. A. R. Díaz, "Using solar energy for irrigation in large water distribution networks: A benchmark study about six irrigation systems in the south of Spain," *Energy Nexus,* vol. 17, pp. 1-18, Februari 2025. https://doi.org/10.1016/j.nexus.2025.100386

[24] G. Yadav, J. A. Garza-Reyes, A. Kumar, S. Luthra, L. Batista and L. Kumar, "A framework to achieve sustainability in manufacturing organisations of developing economies using industry 4.0 technologies' enablers," *Computers in Industry,* vol. 122, 2020. https://doi.org/10.1016/j.compind.2020.103280

LOGIC (JOURNAL ENGINEERING DESIGN AND TECHNOLOGY)
Journal Engineering Design and Technology
Vol. 26 No.2 July 2026 ; p. 112 - 119
Journal Homepage : http://ojs2.pnb.ac.id/index.php/LOGIC
p-ISSN : 1412-114X e-ISSN : 2580-5649

Effect of Pack Carburizing Temperature on the Surface Hardness of ST37 Low-Carbon Steel Using Coconut Shell Charcoal

Pengaruh Temperatur Pack Carburizing terhadap Kekerasan Permukaan Baja Karbon Rendah ST37 Menggunakan Arang Tempurung Kelapa

Hairian Rahmadi [1], Helanianto [1], Made Ery Arsana [2)*]

1) Mechanical Maintenance Study Program, Politeknik Negeri Ketapang, West Kalimantan, Indonesia
2) Department of Mechanical Engineering, Politeknik Negeri Bali, Jalan Kampus Bukit Jimbaran, Badung, Bali, Indonesia

Corresponding email [2)*] : eryarsana@pnb.ac.id

Abstract. Steel is widely used in engineering applications due to its favorable mechanical properties, availability, and cost-effectiveness. However, ST37 low-carbon steel exhibits relatively low surface hardness and wear resistance, limiting its application in components subjected to friction and mechanical loading. This study investigates the effect of pack carburizing temperature on the surface hardness of ST37 steel using coconut shell charcoal as a carburizing medium. The carburizing process was performed at temperatures of 900°C, 1000°C, and 1100°C with a constant holding time of 30 minutes, quenched in water at room temperature (25 ± 2°C). Surface hardness was evaluated using the Rockwell B (HRB) scale. The collected data were analyzed using descriptive statistics and one-way analysis of variance (ANOVA) at a significance level of 0.05. The results showed a gradual increase in average hardness from 48.3 HRB for the untreated specimens to 48.6 HRB, 48.9 HRB, and 49.1 HRB for specimens carburized at 900°C, 1000°C, and 1100°C, respectively, corresponding to a maximum increase of 1.65%. Although the hardness values exhibited an increasing trend with temperature, ANOVA results indicated that the differences among treatment groups were not statistically significant ($F = 1.37$, $p = 0.269$). The modest improvement is attributed to enhanced carbon diffusion at elevated temperatures, while the short holding time may have limited the development of a thicker carburized layer. These findings demonstrate that carburizing temperature influences the surface hardening behavior of ST37 steel; however, longer holding times and microstructural characterization are recommended to achieve more significant hardness enhancement and a better understanding of the carburizing mechanism.

Keywords : Pack carburizing; Carburizing temperature; ST37 low-carbon steel; Surface hardness; Carbon diffusion

1. INTRODUCTION

Steel is one of the most widely utilized engineering materials due to its mechanical strength, versatility, and cost-effectiveness. It is extensively applied in construction, automotive, machinery, and manufacturing industries. Among the various types of steel, low carbon steel—particularly ST37—is commonly used because of its good ductility, weldability, and machinability. However, despite these advantages, ST37 steel exhibits relatively low surface hardness and limited wear resistance, which restrict its application in components subjected to continuous friction and mechanical loading, such as gears, shafts, and rotating parts. To overcome this limitation, surface hardening treatments are commonly employed. One of the most economical and practical methods is carburizing, a thermochemical process that enriches the surface layer of steel with carbon atoms at elevated temperatures. This process increases surface carbon content while maintaining the toughness of the core material. Among the various carburizing techniques, pack carburizing is widely used due to its simplicity and low operational cost. In this method, steel specimens are heated in a carbon-rich solid medium—typically charcoal combined with an energizer such as calcium carbonate ($CaCO_3$). After the carburizing stage, rapid quenching in water or oil promotes the transformation of austenite into martensite, resulting in a harder and more wear-resistant surface layer.

The effectiveness of pack carburizing is strongly influenced by processing parameters, particularly temperature and holding time. Increasing temperature enhances atomic mobility and accelerates carbon diffusion into the steel surface, potentially improving surface hardness and case depth. Recent studies have confirmed that elevated carburizing temperatures and appropriate holding times significantly affect microstructural evolution, carbon diffusion, case depth, and mechanical properties of carburized steels [1]–[3]. Although numerous studies have reported the beneficial effects of carburizing on low-carbon steels, specific investigations focusing on temperature variation in pack carburizing of ST37 steel remain limited. Most previous research emphasizes variations in carburizing media composition or different steel grades.

For example, Baali et al. [4] demonstrated that carburizing holding time influences the structure and hardness of steel, while Santoso et al. [5] reported that both temperature and holding time affect the hardness and microstructural characteristics of pack-carburized AISI 1020 steel. Adedipe et al. [6], [7] highlighted the effectiveness of organic and biomass-derived carburizing additives, including coconut-shell-based media, for improving the surface properties of low-carbon steel. A recent review by Madu et al. [8] further emphasized that carburizing temperature, soaking time, carbon source, and cooling conditions jointly determine carbon diffusion and mechanical performance. High-temperature, time-dependent, and quenching-dependent effects on carburized-layer microstructure, case depth, and hardness have also been reported for low-carbon, automotive, and low-alloy steels [9]–[12]. Studies using locally available carburizing media and alternative energizers have likewise demonstrated their potential to improve hardness and wear resistance [13]–[15]. However, systematic evaluation of temperature variation in pack carburizing treatment specifically for ST37 steel using coconut shell charcoal, while maintaining a fixed short holding time, has not been extensively reported.

Despite numerous studies on pack carburizing, the combined influence of multiple process variables often makes it difficult to isolate the specific contribution of temperature to hardness development. Therefore, this study focuses on quantifying the isolated effect of carburizing temperature variation (900°C–1100°C) on ST37 low-carbon steel while maintaining a fixed holding time of 30 minutes and constant processing conditions. This approach enables a clearer evaluation of the role of temperature in carbon diffusion and surface hardening behavior. The results contribute to the understanding of low-cost carburizing treatments using coconut shell charcoal as a sustainable and locally available carbon source for industrial applications.

2. METHODS

2.1 Research Design

This study employed a laboratory-based experimental research design to investigate the effect of pack carburizing temperature on the surface hardness of ST37 low-carbon steel. The experiment involved heat treatment at three different temperature levels: 900°C, 1000°C, and 1100°C, followed by rapid quenching in mineral water. The untreated specimens were used as the control group. Surface hardness measurements were conducted after the heat treatment process using the Rockwell Hardness Test on the B scale (HRB).

2.2 Materials and Specimen Preparation

The material used in this study was ST37 low-carbon steel, selected due to its widespread industrial application, good machinability, and relatively low surface hardness. The specimens were machined into rectangular dimensions of 150 mm × 80 mm × 10 mm to ensure geometric uniformity and consistency throughout the carburizing, quenching, and hardness testing processes. Maintaining identical specimen dimensions minimized variations in heat transfer, carbon diffusion, and cooling rates, thereby improving the reliability and repeatability of the experimental results. The prepared specimens were divided into four groups, each consisting of ten specimens to improve the reliability and repeatability of the results.

Table 1. Specimen Grouping

Group	Treatment Condition
A	Untreated raw material (Control)
B	Pack carburized at 900°C
C	Pack carburized at 1000°C

Group	Treatment Condition
D	Pack carburized at 1100°C

2.3 Pack Carburizing Procedure

The pack carburizing process was conducted using coconut shell charcoal as the primary carbon source, mixed with calcium carbonate ($CaCO_3$) as an energizer to enhance carbon diffusion. The specimens were embedded in the carburizing medium inside a sealed container.

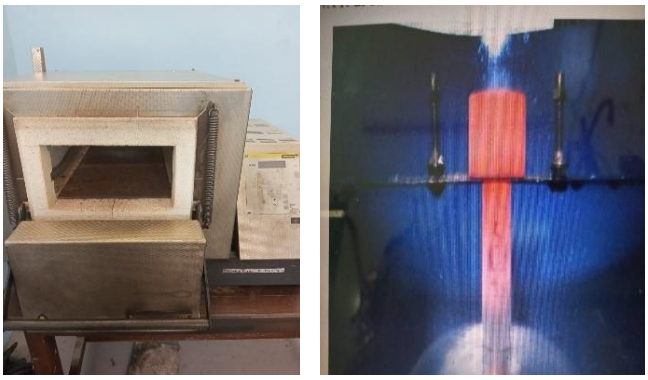

Figure 1. Laboratory furnace used for the pack carburizing heat treatment of ST37 steel specimens.

The container was heated in a laboratory furnace to the designated temperatures of 900°C, 1000°C, and 1100°C, with a constant holding time of 30 minutes for each treatment group (Figure 1). Upon completion of the soaking period, the specimens were immediately removed and quenched in tap water at room temperature (25 ± 2°C) to facilitate martensitic transformation. The overall experimental procedure is summarized in Figure 2.

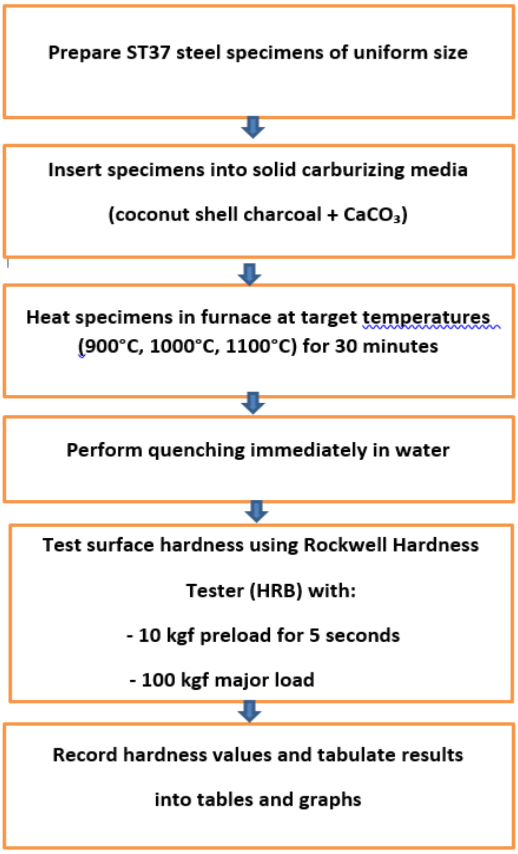

Figure 2. Flowchart of the experimental procedure and data collection process.

The control specimens were tested in the as-received condition without undergoing any heat treatment or carburizing process.

2.4 Hardness Testing
Surface hardness testing was performed using a Rockwell Hardness Tester on the B scale (HRB). For each specimen, multiple indentation measurements were taken at different surface points to minimize measurement error and improve accuracy. Nine indentations were made at different locations on each specimen. The mean of the three measurements was used as the representative hardness value for each specimen. Thus, ten specimen-level mean values were obtained for each treatment group.

2.5 Research Variables
Independent Variable:
Carburizing temperature (900°C, 1000°C, 1100°C)
Dependent Variable:
Surface hardness (HRB)
Controlled Variables:

- Material: ST37 low-carbon steel
- Carburizing medium: Coconut shell charcoal + $CaCO_3$
- Holding time: 30 minutes
- Quenching medium: Mineral water
- Specimen dimensions

2.6 Data Analysis
The collected hardness data were analyzed using descriptive and inferential statistical methods. The mean hardness and standard deviation (SD) were calculated for each treatment group to evaluate the central tendency and data dispersion. The percentage increase in hardness relative to the untreated specimens was also determined to assess the effectiveness of the pack carburizing process. To evaluate whether the differences in hardness among treatment groups were statistically significant, a one-way analysis of variance (ANOVA) was performed at a significance level of $\alpha = 0.05$. The ANOVA results were used to determine the influence of carburizing temperature on the surface hardness of ST37 low-carbon steel.

Graphical representations were prepared to illustrate trends and differences among treatment groups and to facilitate comparison of the experimental results. Statistical calculations were performed using Microsoft Excel to ensure consistency and accuracy of the data analysis.

2.7 Instrument Calibration and Measurement Reliability
To ensure measurement accuracy, before testing, the Rockwell hardness tester was verified using a certified HRB reference block in accordance with the applicable standard laboratory procedure. Repeated measurements were performed on selected specimens to verify consistency and reduce random error. This approach ensured the reliability and reproducibility of the hardness data.

3. RESULTS AND DISCUSSION
3.1 Surface Hardness (HRB) Test


Figure 3. Rockwell Hardness Tester used for measuring the surface hardness of ST37 steel specimens.

The hardness test results of ST37 low-carbon steel specimens after pack carburizing treatment at different temperatures are presented in Table 2.

Table 2. Surface Hardness (HRB) of ST37 Steel under Different Carburizing Temperatures

Treatment	1	2	3	4	5	6	7	8	9	10	Mean (HRB)
Raw Material	51	48	48	47	47	47	49	49	49	48	48.3
900°C	48	48	48	49	49	49	48	48	50	49	48.6
1000°C	49	48	48	48	50	50	49	50	49	48	48.9
1100°C	48	48	49	49	48	49	50	50	50	50	49.1

A graphical comparison of the average hardness values is illustrated in Figure 4.

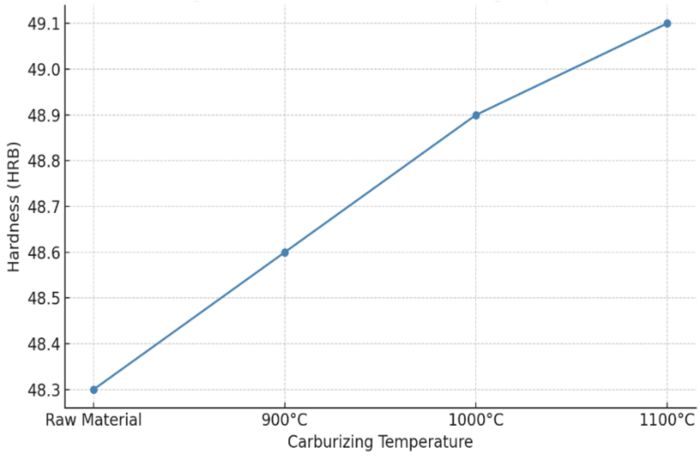

Figure 4. Average Surface Hardness versus Carburizing Temperature

The results indicate a gradual and consistent increase in surface hardness with increasing carburizing temperature. The untreated specimens exhibited an average hardness of 48.3 HRB. After pack carburizing, the average hardness increased to 48.6 HRB at 900°C, 48.9 HRB at 1000°C, and 49.1 HRB at 1100°C.
The percentage increase in hardness from the untreated material to the highest treatment temperature (1100°C) is calculated as:

$$\frac{49.1-48.3}{48.3} x\ 100\% = 1.65\% \quad (1)$$

Although the absolute increase in hardness is relatively small, the consistent upward trend across all treatment levels suggests a positive relationship between carburizing temperature and surface hardness.

3.2 Statistical Analysis

To evaluate whether the differences in hardness values among treatment groups were statistically significant, a one-way analysis of variance (ANOVA) was performed at a significance level of $\alpha = 0.05$. The calculated F-value ($F = 1.37$) was lower than the critical F-value ($F(3,36) = 1.37$, $\alpha = 0.05$), indicating that the differences among the treatment groups were not statistically significant ($p = 0.269$).

Table 3. Mean Hardness and Standard Deviation

Treatment	Mean (HRB)	SD
Raw Material	48.3	1.25

Treatment	Mean (HRB)	SD
900°C	48.6	0.70
1000°C	48.9	0.88
1100°C	49.1	0.88

The calculated standard deviation values indicate relatively low data dispersion, suggesting good repeatability and consistency of the hardness measurements. The lower standard deviation values observed in the carburized specimens compared to the untreated specimens indicate more uniform hardness distribution after heat treatment.

Although a gradual increasing trend in hardness was observed with increasing carburizing temperature, the statistical analysis suggests that the variation in temperature within the tested range (900°C–1100°C) did not produce a significant change in surface hardness under the present experimental conditions.

This result implies that the holding time of 30 minutes may have limited the effective carbon diffusion depth, reducing the statistical impact of temperature variation. Further studies with extended soaking time or microhardness profiling are recommended to better capture the effect of carburizing temperature.

3.3 DISCUSSION

The increase in hardness observed in this study can be explained by enhanced carbon diffusion at elevated temperatures. According to diffusion principles and Fick's second law, the diffusion coefficient increases with temperature according to an Arrhenius-type relationship due to greater atomic mobility. As the carburizing temperature rises, carbon atoms diffuse more effectively into the steel surface, increasing carbon concentration within the austenitic phase. Upon rapid quenching, the carbon-enriched austenite is expected to transform into martensite, which may contribute to increased surface hardness. However, the relatively modest hardness increment (1.65%) indicates that temperature alone may not be sufficient to generate substantial surface hardening under the present experimental conditions. The holding time of 30 minutes likely limited the diffusion depth, resulting in a relatively thin carburized layer. Since diffusion depth is proportional to the square root of time, longer soaking durations could potentially produce more pronounced hardness improvements.

These findings are consistent with previous studies. Baali et al. [4] and Santoso et al. [5] reported that carburizing temperature and holding time influence hardness and microstructural development. Adedipe et al. [6], [7] demonstrated that organic carburizing additives can facilitate carbon transfer and improve surface properties, while Madu et al. [8] summarized the strong dependence of carburizing performance on temperature, soaking time, carbon source, and cooling conditions. Furthermore, Zhang et al. [1], Ballem et al. [2], Viliš et al. [3], Teixeira et al. [9], Boumediri et al. [10], Abdenour et al. [11], and Kolawole et al. [12] confirmed that treatment parameters significantly affect carbon diffusion, microstructure, case depth, hardness, and other mechanical properties in different steel grades. Although several of these studies focused on alloy steels rather than ST37 low-carbon steel, they provide useful insight into the role of carburizing temperature, duration, and cooling conditions in hardness development.

Compared to studies reporting higher hardness increments, the relatively moderate improvement in this research may be attributed to several factors, including shorter holding time, differences in carbon potential of the carburizing medium, and the use of Rockwell B scale testing.

The HRB method may be less sensitive to thin hardened layers compared with microhardness testing methods such as Vickers hardness (HV), which are commonly used to evaluate case-depth profiles. Despite the modest increase, the results demonstrate that coconut shell charcoal combined with $CaCO_3$ can facilitate carbon transfer to the steel surface. This finding is supported by previous studies showing that locally available carbonaceous materials and alternative quenching media can provide economical and more sustainable options for pack carburizing and surface-property enhancement [7], [13]–[15].

Overall, the results indicate an increasing trend in surface hardness with increasing carburizing temperature, although the differences were not statistically significant under the investigated conditions. Nevertheless, further optimization of soaking time and detailed microstructural analysis are recommended to achieve more significant surface strengthening and to fully characterize the carburized layer.

3.4 Research Limitations

This study has several limitations that should be considered when interpreting the results. First, the carburizing holding time was limited to 30 minutes, which may not have been sufficient to produce significant carbon diffusion depth. Since diffusion depth is strongly dependent on both temperature and time, longer soaking durations could potentially yield more pronounced hardness enhancement.

Second, the hardness evaluation was conducted using the Rockwell B (HRB) scale. While suitable for general hardness assessment, this method may be less sensitive in detecting thin carburized layers compared to microhardness testing methods such as Vickers hardness (HV), which provide better resolution for surface case depth profiling.

Third, this study did not include microstructural analysis or metallographic examination. The absence of microstructural observations limits the ability to directly confirm martensitic transformation and determine the carburized case depth. Future research should incorporate optical microscopy or scanning electron microscopy (SEM) analysis to better characterize the carburized layer.

Finally, statistical analysis indicated that the differences among treatment groups were not statistically significant at $\alpha = 0.05$. This suggests that further optimization of process parameters, including soaking time and carbon potential control, is required to achieve more substantial and statistically significant surface hardening effects.

4. CONCLUSION

This study investigated the effect of pack carburizing temperature (900°C, 1000°C, and 1100°C) on the surface hardness of ST37 low-carbon steel using coconut shell charcoal combined with $CaCO_3$ as the carburizing medium. The experimental results demonstrated a gradual increase in surface hardness with increasing carburizing temperature. The highest hardness value (49.1 HRB) was obtained at 1100°C, representing a 1.65% increase compared to the untreated material (48.3 HRB).

However, one-way ANOVA revealed that the differences in hardness among treatment groups were not statistically significant at the 95% confidence level. This finding suggests that, under the current experimental conditions, temperature variation alone—without extended holding time—may not produce substantial surface hardening in ST37 steel.

Despite the modest increase, the results suggest that higher carburizing temperatures may promote carbon diffusion and surface strengthening; however, the observed differences were not statistically significant. The use of coconut shell charcoal as a locally available carburizing medium also demonstrates potential for cost-effective and sustainable surface treatment applications in small- and medium-scale industries.

Future research is recommended to investigate longer soaking times, microstructural characterization, case depth measurement, and alternative quenching media in order to optimize the carburizing process and achieve more significant hardness improvement.

5. ACKNOWLEDGEMENT

The authors would like to express their sincere gratitude to the Materials Testing Laboratory of Ketapang State Polytechnic for providing laboratory facilities and technical support during this research. The authors also thank all individuals who contributed to the completion of this study.

6. REFERENCES

[1] Z. Zhang, Z. Wu, Y. Yuan, X. Wang, and Y. Tian, “Microstructure evolution and mechanical properties of high-temperature carburized 18Cr2Ni4WA steel,” Materials, vol. 17, no. 19, Art. no. 4820, 2024, doi: 10.3390/ma17194820.

[2] M. A. Ballem, M. M. Aldarwish, A. S. Aljuroushi, A. M. Shaka, and A. M. Abdulbakee, “Effect of carburizing temperature and post-carburizing treatments on microhardness and microstructural evolution of carburized low-carbon steel,” Journal of Pure and Applied Sciences, vol. 22, no. 2, pp. 84–95, 2023, doi: 10.51984/jopas.v22i2.2788.https://doi.org/10.13140/RG.2.2.11340.72323

[3] J. Viliš, D. Dobrocký, Z. Joska, J. Procházka, et al., “The effect of changing the temperature of the vacuum carburizing process on the layer properties of steels used in the automotive industry,” International Journal of Advanced Manufacturing Technology, 2025, doi: 10.1007/s00170-025-15319-y.https://doi.org/10.51984/jopas.v22i2.2788

[4] S. Baali, Y. Benarioua, and A. E. Mazouz, “An experimental study of the influence of carburizing treatment holding time on the structure and hardness of 16NC6 steel,” Engineering, Technology & Applied Science Research, vol. 13, no. 2, pp. 10478–10482, 2023, doi: 10.48084/etasr.5684.https://doi.org/10.26877/asset.v6i1.1758302401023

[5] E. Santoso, Fatkhurrohman, A. R. Firmansyah, and S. C. Putra, “Hardness and microstructural characterization of pack carburizing AISI 1020 low-carbon steel by temperature and holding time variations,” Advance Sustainable Science, Engineering and Technology, vol. 6, no. 1, Art. no. 02401023, 2024, doi: 10.26877/asset.v6i1.17583.https://doi.org/10.1016/j.susmat.2023.e00723

[6] O. Adedipe, R. O. Medupin, K. O. Yoro, E. T. Dauda, V. S. Aigbodion, N. A. Agbo, et al., “Sustainable carburization of low carbon steel using organic additives: A review,” Sustainable Materials and Technologies, vol. 38, Art. no. e00723, 2023, doi: 10.1016/j.susmat.2023.e00723.http://jurnal.ft.uns.ac.id/index.php/mekanika/article/view/616

[7] O. Adedipe et al., “Explicit microstructural and electrochemical study of value-added carburized mild steel with coconut shell ash and $CaCO_3$ nanoparticles derived from periwinkle shell,” Chemical Data Collections, vol. 45, Art. no. 101028, 2023, doi: 10.1016/j.cdc.2023.101028.https://doi.org/10.1016/j.cdc.2023.101028

[8] M. J. Madu, O. Adedipe, S. A. Lawal, et al., “The influence of carburization parameters on the mechanical behavior of mild steel: A review,” Journal of Engineering and Applied Science, vol. 72, Art. no. 193, 2025, doi: 10.1186/s44147-025-00776-9.https://doi.org/10.1590/s1516-14392009000400018

[9] J. Teixeira, K. Jeyabalan, G. Geandier, J. Dulcy, B. Denand, et al., “In situ HEXRD experimental study and prediction of microstructures and internal stresses during heat treatment of carburized and carbonitrided low-alloyed steels,” Acta Materialia, vol. 275, Art. no. 120065, 2024, doi: 10.1016/j.actamat.2024.120065.https://doi.org/10.15587/1729-4061.2021.228627

[10] H. Boumediri et al., “Effect of carburizing time treatment on microstructure and mechanical properties of low alloy gear steels,” Materials Research Express, vol. 11, no. 7, Art. no. 076505, 2024, doi: 10.1088/2053-1591/ad5cd6.https://doi.org/10.14419/ijet.v4i1.3866

[11] S. Abdenour, A. Linda, C. Oualid, B. Ali, L. Mohammed Salah, D. Hamid, and C. Francisco, “Influence of the carburization time on the structural and mechanical properties of XC20 steel,” Materials Research Express, vol. 8, no. 8, Art. no. 085604, 2021, doi: 10.1088/2053-1591/ac1ece.https://doi.org/10.1142/S021797922150065X

[12] M. Y. Kolawole, S. A. Aliyu, S. A. Bello, and K. O. Oladosu, “Effect of bio-mineral oil blend quenchant on the mechanical properties of carburized mild-steel,” Journal of Engineering and Applied Science, vol. 70, 2023, doi: 10.1186/s44147-023-00263-z.https://doi.org/10.3390/ma1719482

[13] E. Surojo and J. Triyono, “Pengaruh bahan energizer pada proses pack carburizing terhadap kekerasan cangkul produksi pengrajin pande besi,” Mekanika, vol. 6, no. 2, pp. 1–8, 2017.https://doi.org/10.1016/j.susmat.2023.e00723

[14] S. Darmo, S. Sinarep, and R. Soenoko, “A study of the pack carburizing quenching treatment with cane molasses cooling medium effect on the wear resistance of low carbon steel,” Eastern-European Journal of Enterprise Technologies, vol. 2, no. 12–110, pp. 32–37, 2021, doi: 10.15587/1729-4061.2021.228627.https://doi.org/10.1016/j.actamat.2024.120065

[15] W.-C. Ramli and A. Shaaban, “Mechanical properties of pack carburized SCM 420 steel processed using natural shell powders and extended carburization time,” Crystals, vol. 11, no. 9, Art. no. 1136, 2021, doi: 10.3390/cryst11091136.https://doi.org/10.26877/asset.v6i1.17583

(JOURNAL ENGINEERING DESIGN AND TECHNOLOGY)

Journal Engineering Design and Technology
Vol. 26 No.2 July 2026 ; p. 120 - 132
Journal Homepage : http://ojs2.pnb.ac.id/index.php/LOGIC
p-ISSN : 1412-114X e-ISSN : 2580-5649

Design of a Fuzzy Logic Based Control System for BLDC Motor Speed and Cooling Fan Using Error and Error Change

Aulia Adawiyah [1)*], Arief Suryadi Satyawan [2)], Helfy Susilawati [1)], Esti Fitria Wulandari [1)], Rendi Tri Sugian [1)], Iasya Faiqoh Nurrohmah [1)], Fajar Rahmat Akbar [1)], Andika Muhammad Nur Kholiq [1)]

1) Departement of Electrical Engineering, Garut University, Garut, Indonesia
2) Telecommunications Research Center, National Research and Innovation Agency (BRIN), KST Samaun Samadikun, Bandung, Indonesia

Corresponding email [1)*] : 24052122002@fteknik.uniga.ac.id

Abstract. This study presents the design and simulation-based evaluation of a fuzzy logic controller for a 48 V, 10 kW BLDC motor system integrating speed control and thermal management through a cooling fan. The controller employs four input variables, namely RPM error, change in RPM error, temperature error, and change in temperature error, within an 81-rule fuzzy inference system using triangular membership functions. Minimum-based rule evaluation, maximum aggregation, and weighted-average defuzzification are applied to generate PWM control signals. An interactive GUI-based simulation platform incorporating visualization, data logging, and automated testing was developed to systematically evaluate the complete fuzzy rule base. Simulation results from all 81 fuzzy-rule combinations show that the motor PWM adapts to variations in speed error, while the fan PWM is prioritized under elevated temperature conditions to enhance thermal safety. Overlapping membership functions produce smooth intermediate PWM outputs, whereas the discrete PWM-to-RPM mapping results in stepwise speed variations. Overall, the proposed controller demonstrates stable and adaptive speed and thermal control behavior in simulation and provides a practical foundation for future real-time hardware implementation and quantitative experimental validation.

Keywords : Fuzzy control, BLDC motor, Speed control (RPM), Temperature control / fan control.

1. INTRODUCTION

The development of control systems in electrical engineering and mechatronics requires controllers that are stable, adaptive, and robust under dynamically changing operating conditions. In BLDC motor systems, one of the main challenges is maintaining the desired RPM despite load variations, voltage fluctuations, and external disturbances, while also managing the thermal condition of the motor during high-speed and high-power operation. Uncontrolled temperature rise can reduce efficiency, accelerate insulation degradation, and shorten motor lifespan. Therefore, thermal management is an essential aspect of motor control that cannot be separated from speed regulation [1]. Conventional controllers such as PID are still widely used in industrial applications because of their simple structure. However, their performance strongly depends on the accuracy of the mathematical model and the parameter tuning process [2]. Since BLDC motors and cooling systems are nonlinear, time-varying, and influenced by load and environmental conditions, model-based controllers may suffer from overshoot, oscillations, or significant steady-state error when operating outside nominal conditions [3].

Fuzzy logic has emerged as an effective approach for controlling nonlinear and uncertain systems because it can handle nonlinearities and uncertainties without relying entirely on precise mathematical models. Instead, fuzzy logic controllers employ linguistic IF–THEN rules to represent heuristic knowledge, making them well suited for systems operating under varying and uncertain conditions [4], [5]. Previous studies have shown that fuzzy logic controllers can improve motor speed response, reduce overshoot, and maintain low steady-state error under variable load conditions, while comparative investigations have further demonstrated their superior transient performance, faster settling time, and greater robustness than conventional PID-based approaches under varying operating conditions [6]-[9]. In addition, hybrid approaches such as fuzzy PI and fuzzy-based PID autotuning have been investigated to improve dynamic response and steady-state stability in motor control applications [10]. Similar advantages have also been demonstrated in thermal management systems, where fuzzy logic based temperature regulation and cooling fan control provide smoother, more adaptive responses to changing thermal conditions than conventional on off or fixed linear control strategies. [11]-[14].

Despite the widespread application of fuzzy controllers in motor drives and thermal management, most studies primarily evaluate control performance rather than systematically analyzing the complete fuzzy rule base or the behavior of all rule combinations across the input space. Consequently, the operation of the fuzzy inference mechanism over the entire rule base is often not explicitly demonstrated [15], [16]. Therefore, this study performs a systematic simulation-based evaluation of all 81 fuzzy-rule combinations using an automated testing procedure. This approach ensures that every rule in the fuzzy rule base is activated and evaluated under representative operating conditions, which is rarely reported in previous studies.

Based on this gap, the objective of this research is to design and evaluate, through a GUI-based simulation environment, a fuzzy logic controller capable of maintaining the BLDC motor speed at the desired reference value while simultaneously regulating the cooling fan according to the motor temperature and its rate of change. The proposed controller is implemented in an interactive simulation platform equipped with visualization, data logging, and automated testing features, enabling systematic evaluation of the controller behavior prior to hardware implementation.

The primary contribution of this study is the development of a unified fuzzy control strategy that simultaneously regulates BLDC motor speed and cooling-fan operation while systematically evaluating all 81 fuzzy-rule combinations through an automated testing procedure. Unlike previous studies, which primarily focused on fuzzy controller design and rule-base optimization rather than comprehensive analysis of the complete fuzzy rule base, this work systematically investigates the behavior of all fuzzy rules over the entire input space within a GUI-based simulation environment before hardware implementation [17]. To realize this framework, the controller employs triangular membership functions, weighted-average defuzzification, and discrete PWM-to-RPM mapping to provide a computationally efficient approximation of actuator responses during simulation. A further contribution of this work is the implementation of a rule-aware automated testing procedure that activates every fuzzy rule and records the corresponding controller outputs for quantitative analysis. Consequently, this study provides theoretical insight into fuzzy-rule behavior and establishes a simulation-based foundation for future hardware implementation and experimental validation of integrated BLDC motor speed and thermal management systems.

2. METHODS

Figure 1 illustrates the closed-loop control architecture for the BLDC motor system. The motor speed reference RPM_{ref} is compared with the measured motor speed RPM_{meas} to generate the speed error.In discrete form, this error is defined as

$$e(k) = RPM_{ref}(k) - RPM_{meas}(k) \tag{1}$$

where:

- $e(k)$: speed error at the k-th sampling instant (rpm)
- $RPM_{ref}(k)$: reference motor speed (rpm)
- $RPM_{meas}(k)$: measured motor speed (rpm)
- k: discrete sampling index.

and the change of error is expressed as

$$\Delta e(k) = e(k) - e(k-1) \tag{2}$$

where:

- $\Delta e(k)$: change in speed error (rpm);
- $e(k)$: current speed error (rpm);
- $e(k-1)$: previous speed error (rpm).

The diagram also includes a cooling subsystem that monitors the motor temperature, resulting in a temperature error

$$e_T(k) = T_{ref}(k) - T_{meas}(k) \quad (3)$$

where :

- $e_T(k)$: motor temperature error at the k-th sampling instant (°C);
- $T_{ref}(k)$: reference motor temperature at the k-th sampling instant (°C);
- $T_{meas}(k)$: measured motor temperature at the k-th sampling instant (°C);

and the change of temperature error

$$\Delta e_T(k) = e_T(k) - e_T(k-1) \quad (4)$$

where:

- $\Delta e_T(k)$: change in temperature error (°C);
- $e_T(k)$: current temperature error (°C);
- $e_T(k-1)$: previous temperature error (°C).

These four variables $e(k)$, Δe(k), $e_T(k)$, and $\Delta e_T(k)$ serve as the primary inputs to the fuzzy controller, which regulates the PWM signals for both the motor and the cooling fan. The use of error and change-of-error as the primary inputs is a conventional design approach in fuzzy control systems [18].

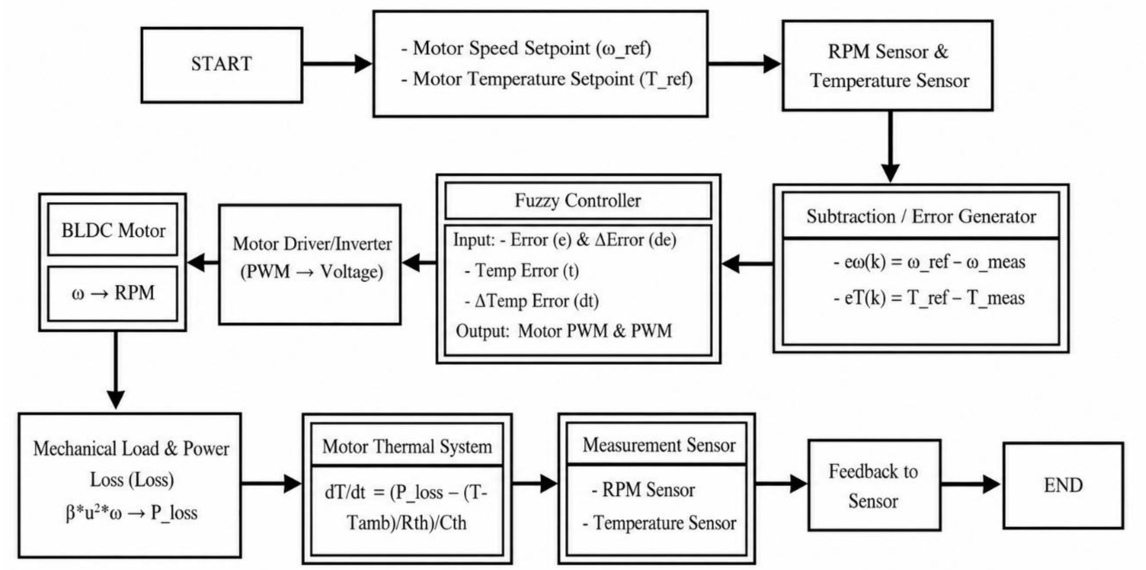

Figure 1. Flow Diagram of the 10 kW BLDC Motor Control System

The fuzzy controller structure is shown in Figure 2 and consists of fuzzification, rule evaluation, aggregation, and defuzzification. During fuzzification, each input is mapped to a triangular membership function, which is widely adopted because of its simplicity, computational efficiency, and ease of implementation in fuzzy control systems [18].

$$\mu_{tri}(x; a, b, c) = \max\left(\min\left(\frac{x-a}{b-a}, \frac{c-x}{c-b}\right), 0\right) \quad (5)$$

where:

- $\mu_{tri}(x)$: membership degree;
- x: input variable;
- a, b, c: triangular membership parameters.

where $a < b < c$, ensuring that both denominators remain non-zero. In the implementation, RPM error and Δe are represented by the linguistic sets NEG, ZERO, and POS, whereas temperature and Δe_T are represented by LOW, MED, and HIGH. The GUI displays these membership functions to help visualize the position of each input relative to its linguistic terms.

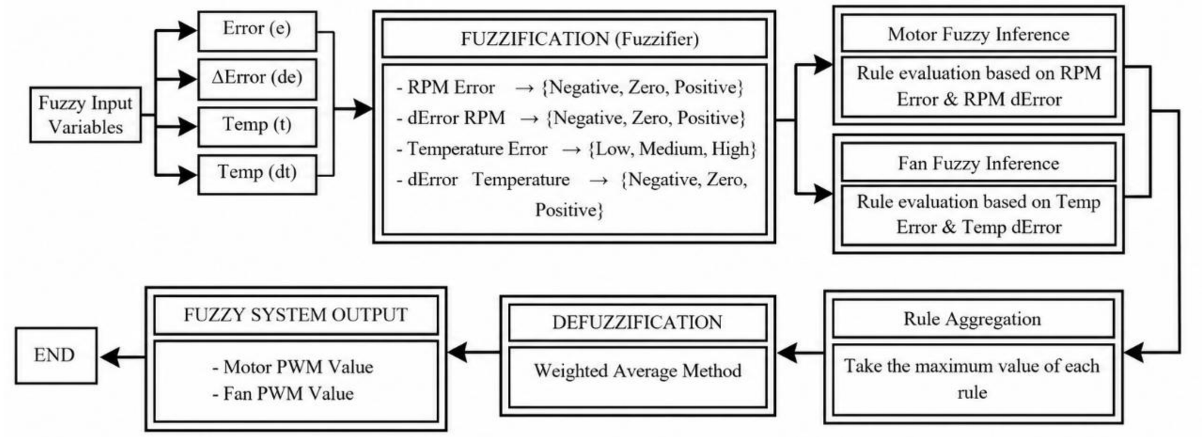

Figure 2. Fuzzy controller architecture for the BLDC motor control system illustrated in Fig. 1

Each fuzzy rule is expressed in IF–THEN form. The rule activation degree is computed using the minimum operator as

$$\alpha_i = \min(\mu_E^A, \mu_{\Delta E}^B, \mu_T^C, \mu_{\Delta T}^D) \tag{6}$$

where:

- α_i is the firing strength of the i-th fuzzy rule;
- μ_E^A is the membership degree of the speed error corresponding to the linguistic term A;
- $\mu_{\Delta E}^B$ is the membership degree of the change in speed error corresponding to the linguistic term B;
- μ_T^C is the membership degree of the temperature error corresponding to the linguistic term C;
- $\mu_{\Delta T}^D$ is the membership degree of the change in temperature error corresponding to the linguistic term D.

Equation (6) follows the conventional Mamdani fuzzy inference mechanism, where the logical AND operation is implemented using the minimum operator to determine the firing strength of each fuzzy rule [18].

The minimum operator is employed because each fuzzy rule represents the logical conjunction (AND) of the four antecedent conditions. Consequently, the firing strength of a rule is determined by its least satisfied antecedent, following the conventional Mamdani inference mechanism. The resulting activation degree is subsequently used during the defuzzification stage to compute the motor and cooling-fan PWM outputs.

The controller output is obtained using the weighted-average defuzzification method, which is commonly employed in singleton-based fuzzy inference systems because of its computational efficiency and smooth output generation [18].

$$PWM_m = \frac{\mu_e^- P_- + \mu_e^0 P_0 + \max(\mu_e^+, \mu_{\Delta e}^+) P_+}{\mu_e^- + \mu_e^0 + \max(\mu_e^+, \mu_{\Delta e}^+) + \varepsilon} \tag{7}$$

Where:

- PWM_m is the motor PWM output;
- μ_e^-, μ_e^0, and μ_e^+ are the membership degrees of the speed error corresponding to the NEG, ZERO, and POS linguistic sets, respectively;
- $\mu_{\Delta e}^+$ is the membership degree of the positive change in speed error;
- P_-, P_0, and P_+ are the singleton output weights for the LOW, MEDIUM, and HIGH motor PWM levels, respectively;
- ε is a small positive constant introduced to avoid division by zero.

Unlike the minimum operator used for antecedent evaluation in Equation (6), the maximum operator in Equation (7) is applied only during output aggregation. Multiple activated rules may support the same positive output singleton through either a positive speed error or a positive change in speed error. Therefore, the maximum operator preserves the strongest contribution without double-counting overlapping memberships. This simplified aggregation strategy reduces computational complexity while maintaining the intended control behavior, particularly the rapid acceleration response and thermal safety prioritization required by the controller. Accordingly, the antecedent evaluation remains based on the minimum operator defined in Equation (6), whereas the maximum operator is used exclusively for aggregating the contributions of rules that support the same output singleton.

Following the weighted-average defuzzification approach described in [18], the singleton output weights for the motor controller are assigned values of 100, 150, and 255, corresponding to the LOW, MEDIUM, and HIGH PWM levels, respectively. The cooling-fan output is computed using the same weighted-average defuzzification approach with temperature-related membership values and singleton output weights of 20, 80, and 255. Furthermore, the positive temperature-error change (Δe_T) is incorporated to detect rapid temperature increases, enabling the controller to increase the fan speed promptly whenever thermal safety becomes a priority. After defuzzification, the PWM values are converted into actuator responses using a piecewise PWM-to-RPM model. The motor output is mapped to discrete RPM levels (e.g., 0, 250, 400, 800, ..., up to 5000 rpm). Similarly, the cooling fan uses a duty-cycle conversion,

$$Duty = \frac{PWM}{255} \times 100\% \quad (8)$$

Where:

- Duty : PWM duty cycle (%)
- PWM : pulse width modulation value (0–255)

together with a lookup table relating duty cycle to fan RPM. This discrete approximation represents the actuator behavior without requiring a continuous physical model and facilitates systematic evaluation of the fuzzy rule base in the GUI prior to future hardware implementation.

The fuzzy rule base contains 81 combinations derived from the four inputs, each having three linguistic sets. For presentation efficiency, Tables 1–3 show compact 3×3 representations for the temperature conditions LOW, MED, and HIGH. Each cell contains three ordered tuples of (PWM_{motor}, PWM_{fan})corresponding to ΔT = NEG, ZERO, and POS, respectively. Thus, the ordering inside each cell is explicitly read from left to right as ΔT =NEG, ΔT = ZERO, and ΔT = POS.

At low temperatures, cooling is not prioritized; thus, fuzzy rules keep the fan PWM at low to medium levels unless a rapid temperature rise (ΔT > 0) occurs. Motor PWM control is mainly governed by speed error and its change. Table 1 lists the 27 fuzzy rules for the T = “LOW” condition.

Table 1. Design of fuzzy rules to maintain the cooling fan PWM at low to medium levels (compact 3×3 representation).

E \ ΔE	NEG	ZERO	POS
NEG	(100,20);(100,20);(100,80)	(100,20);(100,20);(100,80)	(150,20);(150,20);(150,80)
ZERO	(150,20);(150,20);(150,80)	(150,20);(150,20);(150,80)	(255,20);(255,20);(255,80)
POS	(255,20);(255,20);(255,80)	(255,20);(255,20);(255,80)	(255,20);(255,20);(255,80)

Note : Each cell contains three tuples for ΔT = NEG ; ZERO ; POS in that order, formatted as (PWM_motor,PWM_fan). Rows = E ∈ {NEG, ZERO, POS}; columns = ΔE ∈ {NEG, ZERO, POS}.

At medium temperatures, cooling becomes more important, the fan PWM is typically set to a medium level and increases when a temperature rise (ΔT > 0) is detected. Motor PWM control remains governed by the speed error and its change. Table 2 lists the 27 fuzzy rules for T = “MED”.

Table 2. Design of fuzzy rules to maintain the cooling fan PWM at a medium level (compact 3×3 representation).

E\ΔE	NEG	ZERO	POS
NEG	(100,80);(100,80);(100,255)	(100,80);(100,80);(100,255)	(150,80);(150,80);(150,255)
ZERO	(150,80);(150,80);(150,255)	(150,80);(150,80);(150,255)	(255,80);(255,80);(255,255)
POS	(255,80);(255,80);(255,255)	(255,80);(255,80);(255,255)	(255,80);(255,80);(255,255)

Note : Cell format and ordering are identical to Table 1.
At high temperatures, thermal safety is prioritized, all rules set the fan PWM to its maximum regardless of speed error or its change, while motor PWM remains regulated by speed error to maintain performance. Table 3 lists the 27 fuzzy rules for T = "HIGH".

Table 3. Design of fuzzy rules to maintain the cooling fan PWM at a high level (compact 3×3 representation).

E\ΔE	NEG	ZERO	POS
NEG	(100,255);(100,255);(100,255)	(100,255);(100,255);(100,255)	(150,255);(150,255);(150,255)
ZERO	(150,255);(150,255);(150,255)	(150,255);(150,255);(150,255)	(255,255);(255,255);(255,255)
POS	(255,255);(255,255);(255,255)	(255,255);(255,255);(255,255)	(255,255);(255,255);(255,255)

Note : Cell format and ordering are identical to Table 1.
The fuzzy rule base comprises 81 rules spanning all combinations of the speed and temperature input variables. Each rule contributes to the final control action through its firing strength, as defined in Equation (6), and the weighted-average defuzzification process in Equation (7). This rule structure is consistent with the fuzzy inference architecture illustrated in Fig. 2 while employing the simplified output aggregation strategy described previously to improve computational efficiency for real-time implementation.

Due to space limitations, Tables 1–3 present representative subsets of the rule base using compact 3 × 3 matrices for the LOW, MED, and HIGH temperature conditions. The complete 81-rule table, listing all combinations of the input variables (E, ΔE, T, and ΔT) together with the corresponding motor and fan PWM outputs, is provided in Appendix A. This appendix ensures the reproducibility of the proposed fuzzy controller while keeping the main manuscript concise.

The proposed fuzzy controller was implemented in a Python-based graphical user interface (GUI) developed using Tkinter and the scikit-fuzzy library. The GUI provides interactive input controls, visualization of the membership functions, automatic computation of motor and cooling-fan PWM outputs, data logging, Excel/CSV export, and an automated testing module. This platform serves as the simulation environment used to evaluate the controller behavior before future hardware implementation.

The automated testing procedure systematically evaluates all 81 unique fuzzy-rule combinations derived from the four input variables, each represented by three linguistic sets ($3^4 = 81$). Each rule combination is evaluated once to ensure that every fuzzy rule in the rule base is activated. For each evaluation, the corresponding motor and cooling-fan PWM outputs are computed and recorded automatically. The recorded outputs are then exported for subsequent quantitative analysis and verification of the controller behavior across the complete input space.

3. RESULTS AND DISCUSSION

Simulation experiments were conducted to evaluate the fuzzy controller described in Section 2. The controller was tested using the four fuzzy inputs (E, ΔE, ET, and ΔET), while the motor PWM/RPM and fan PWM/RPM served as the controller outputs. The automated testing procedure generated results for all 81 unique fuzzy-rule combinations. Table 4 presents 36 representative samples selected to illustrate the controller behavior over different operating conditions, while the complete dataset was used for the quantitative analysis reported later in this section. These samples provide a representative basis for evaluating the effects of the fuzzification, inference, and defuzzification processes on the actuator responses.

Table 4. Experimental results for the BLDC motor fuzzy control system under 36 test conditions

No.	Speed Level	Reference RPM	Temperature (°C)	RPM Error (rpm)	ΔRPM Error (rpm)	Temperature Error (°C)	ΔTemperature Error (°C)	Motor PWM	Motor RPM	Fan PWM	Fan RPM
1	8	5000	26.86	-723.25	208.1	33.14	-18.76	10	196	28.2	1380
2	5	2000	43.06	-1061.4	-72.98	16.94	9.3	10	196	38.3	1879
3	8	5000	117.77	1604.34	-498.79	-57.77	-3.27	16.4	320	255	4500
4	3	800	48.9	-1294.65	27.82	11.1	11.47	10	196	88.1	3081
5	1	200	86.01	-221.71	242.09	-26.01	-2.08	16.7	327	100.3	3272
6	4	1000	33.24	1400.04	-158.03	26.76	-18.02	178.5	3500	22.7	1114
7	2	400	39.74	1175.46	-197.32	20.26	0.93	149.9	2938	20.3	993

8	2	400	73.2	1610.27	393.65	-13.2	-5.32	154.0	3019	94.7	3185
9	6	3000	102.42	-306.57	-215.0	-42.42	2.21	10	196	255	4500
10	2	400	68.08	-592.26	475.24	-8.08	-4.8	10	196	102.3	3302
11	5	2000	29.41	-1293.43	-147.8	30.59	19.36	10	196	36.7	1799
12	1	200	50.91	-1421.15	-190.88	9.09	-14.78	10	196	72.7	2839
13	3	800	49.56	167.94	-90.64	10.44	14.2	81.2	1591	92.8	3155
14	8	5000	115.11	119.98	73.8	-55.11	-16.71	16.7	328	255	4500
15	7	4000	58.15	341.26	-437.68	1.85	15.24	87.4	1713	154.7	3820
16	1	200	118.57	-293.6	-50.39	-58.57	-6.79	10	196	255	4500
17	3	800	114.58	708.73	-82.19	-54.58	-3.21	10	196	255	4500
18	2	400	112.18	1754.16	-123.58	-52.18	10.8	17.9	350	255	4500
19	8	5000	91.19	-1476.93	344.49	-31.19	-2.48	10	196	255	4500
20	3	800	55.04	-245.6	-176.46	4.96	19.05	34.3	673	132.3	3556
21	6	3000	95.44	1053.7	233.03	-35.44	-10.18	53.7	1053	255	4500
22	3	800	57.53	-759.33	98.03	2.47	-2.14	10	196	125.2	3481
23	3	800	101.68	-1784.47	61.71	-41.68	17.24	10	196	255	4500
24	7	4000	112.47	558.84	298.63	-52.47	-4.0	10	196	255	4500
25	4	1000	91.71	-1321.91	389.16	-31.71	-0.27	10	196	255	4500
26	6	3000	114.33	27.53	27.49	-54.33	2.25	15.4	301	255	4500
27	2	400	38.32	-801.59	-134.25	21.68	-18.67	10	196	18.4	903
28	8	5000	95.42	-1271.36	-391.18	-35.42	3.29	10	196	255	4500
29	1	200	114.74	-1349.31	-56.68	-54.74	-10.05	10	196	255	4500
30	3	800	32.36	-685.63	458.56	27.64	12.86	10	196	33.2	1626
31	5	2000	46.31	-1322.83	18.3	13.69	-3.23	10	196	57.9	2607
32	7	4000	89.55	391.11	-118.43	-29.55	-4.8	100.0	1959	101.8	3296
33	5	2000	46.53	138.23	206.69	13.47	-6.52	133.4	2615	59.2	2628
34	1	200	112.12	1492.58	-328.24	-52.12	-0.49	15.2	298	255	4500
35	6	3000	117.51	952.49	-207.45	-57.51	-12.17	10	196	255	4500
36	8	5000	22.31	1549.72	487.29	37.69	1.3	197.6	3874	37.7	1847

Note: *Speed Level* is a categorical test setting representing the reference speed condition, where 1 = 250 rpm, 2 = 400 rpm, 3 = 800 rpm, 4 = 1000 rpm, 5 = 2000 rpm, and 6 = 3000 rpm. RPM Error and ΔRPM Error are expressed in rpm, while Temperature Error and ΔTemperature Error are expressed in °C.

The membership-function plots (Fig. 3) show that many measurements lie in transition regions between linguistic labels (e.g., NEG/ZERO or ZERO/POS for RPM error and LOW/MED/HIGH for temperature). Due to the overlapping triangular functions, multiple rules are partially activated, producing intermediate PWM outputs. This is reflected in the experimental results, where motor PWM values cluster around 100–150 and fan PWM around 20–80 before sharply increasing to 200–255 under strong HIGH or positive ΔTactivation, consistent with the fuzzification and aggregation design in Section 2.

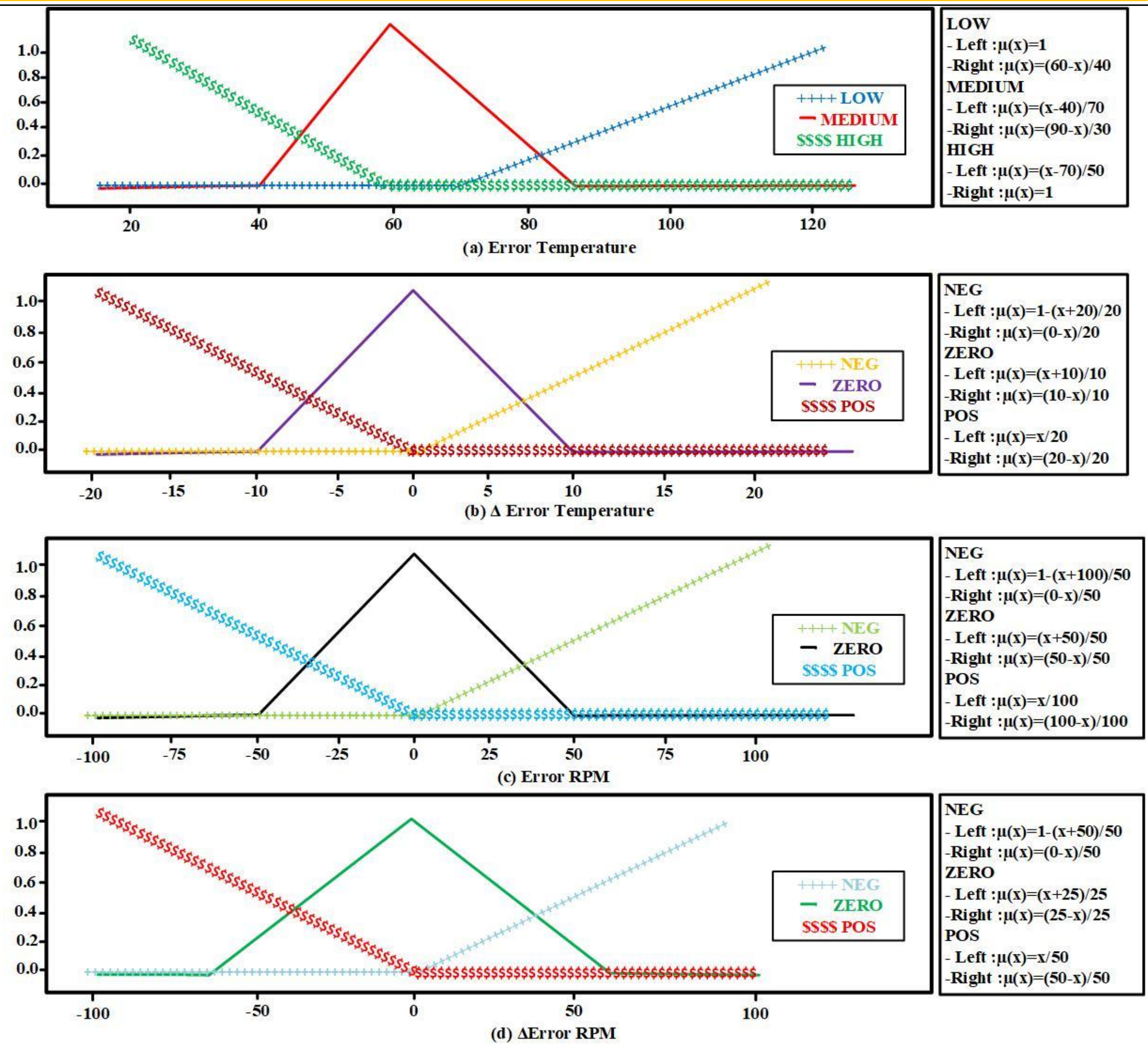

Figure 3. Membership function plots

The representative samples shown in Table 4 and the complete dataset of 81 fuzzy-rule combinations consistently demonstrate the expected relationship between RPM error and motor PWM: large positive RPM errors (≈ +90) produce high motor PWM values (≈ 200–230) and mapped motor speeds of about 4300–4500 rpm, indicating acceleration demand. In contrast, negative or small RPM errors yield lower PWM outputs (≈ 30–150) with mapped motor speeds between 250 and 3300 rpm. This behavior verifies that the motor-control rules based on the combined effects of $E$and ΔE operate as intended.

The effect of error dynamics ΔE is evident in transient cases where the RPM error is moderate but increasing. Samples with $E \approx 40$ and positive ΔE show higher motor PWM outputs (≈110–200, mapped to 3800–4300 rpm) than cases with similar E but negative ΔE, which yield lower PWM values (≈20–80, mapped to 2500–3300 rpm). This confirms that including ΔE in the rule base effectively captures the need for rapid corrective acceleration, as defined in the methodology.

Cooling-system results show consistent application of thermal safety rules: samples with HIGH temperature error or positive ΔE_T produce maximum fan PWM (255) and mapped speeds of 4300–4500 rpm. At LOW or MED temperatures, fan PWM typically remains within 20–80, unless a positive ΔE_T raises it to about 110–200 (≈3800 rpm), demonstrating that the temperature rise rate alone can trigger strong cooling. This confirms the effectiveness of the max operator and priority rules in the rule base.

The discrete PWM–RPM mapping must be considered when interpreting the results, as PWM values are assigned to RPM buckets (e.g., low PWM → 250–400 rpm, medium → 800–2000 rpm, high → 3000–5000 rpm). As a result, small PWM changes may cause stepwise jumps rather than proportional RPM variations; for example, PWM ≈30 maps to 250 rpm, ≈200 to 3000 rpm, and ≈230 to 4500 rpm. Therefore, quantitative PWM–RPM analysis should account for this stepwise behavior.

The results show that the optimized implementation, which employs weighted-average defuzzification instead of conventional centroid defuzzification while retaining the complete 81-rule fuzzy rule base, preserves the intended control behavior. These include thermal safety prioritization, sensitivity to ΔE for rapid correction, and averaging effects from partial rule activation. The observed motor and fan PWM patterns and mapped RPMs are therefore theoretically consistent with the rule base, while intermediate outputs are explained by membership overlap and weighted-average defuzzification, which combines the contributions of multiple activated rules. Since this study is simulation-based, the observed inaccuracies mainly arise from the discretization of the input variables, the simplified weighted-average defuzzification process, and the discrete PWM-to-RPM mapping rather than from physical sensor noise. The weighted-average defuzzification attenuates small input variations, while the discrete PWM-to-RPM mapping produces stepwise changes in the actuator response (e.g., a fan PWM increase from approximately 80 to 137 results in a speed transition from about 3300 rpm to 3800 rpm). In addition, further refinement of the membership functions may improve the resolution and linearity of the controller outputs, providing a useful direction for future hardware implementation.

An additional limitation of this study is that the controller evaluation is restricted to simulation-based analysis and therefore does not include standard real-time control performance metrics such as rise time, settling time, overshoot, or steady-state response under actual hardware operation. These metrics generally require closed-loop experimental validation using a physical BLDC motor system and cannot be reliably assessed within the simplified GUI-based simulation environment employed in this work. Consequently, the present study focuses on verifying the correctness of the fuzzy inference mechanism, the complete 81-rule base, and the corresponding actuator responses rather than evaluating dynamic real-time performance. Experimental validation incorporating these standard control-performance metrics will therefore constitute an important direction for future research. To complement the qualitative observations discussed above, descriptive statistics were computed using all 81 unique fuzzy-rule combinations. The results are summarized in Table 5.

Table 5. Descriptive statistics of motor and fan outputs obtained from the 81 unique fuzzy-rule combinations

RPM Error Range	Samples	Mean Motor PWM	SD Motor PWM	Mean Motor RPM	SD Motor RPM	Mean Fan PWM	SD Fan PWM
−100 to −50	23	30.0000	0.0000	196.0000	0.0000	137.8870	95.5449
−50 to 0	30	56.7200	55.7913	1111.8333	1093.9446	126.4433	84.2407
0 to 50	16	68.4625	53.8964	1342.1250	1056.6828	166.9563	85.3842
50 to 100	12	151.8083	61.3095	2976.0000	1202.3335	137.4167	75.2883

Note: Mean Motor RPM and Mean Fan RPM represent the actuator speeds obtained from the PWM-to-RPM mapping used in the GUI-based fuzzy controller simulation.

To complement the representative samples presented in Table 4, descriptive statistics were computed using all 81 unique fuzzy-rule combinations, as summarized in Table 5. The results show that motor PWM increases with increasing RPM error. For large negative RPM errors (−100 to −50), the motor PWM remains constant at 30.00 (SD = 0.00), indicating that all corresponding fuzzy rules generate the same low control action. As the RPM error increases, the average motor PWM also increases, reaching 151.81 for the 50 to 100 range. The larger standard deviations in the remaining ranges indicate the influence of overlapping membership functions and weighted-average defuzzification, which produce intermediate PWM values through simultaneous activation of multiple fuzzy rules. In contrast, the mean fan PWM remains relatively stable across all RPM error ranges because it is primarily determined by the temperature error and its rate of change. Overall, these statistical results quantitatively confirm the expected behavior of the proposed fuzzy controller and are consistent with the qualitative observations obtained from the representative samples in Table 4.

4. CONCLUSION

This study presented a simulation-based fuzzy logic controller that integrates BLDC motor speed control and thermal management within a unified control framework. The controller employs four fuzzy inputs with three linguistic sets each, resulting in 81 fuzzy rules that were systematically evaluated using an automated testing procedure. The simulation results confirm that all rule combinations were successfully activated and that the controller produces stable and adaptive motor and cooling-fan PWM outputs consistent with the designed fuzzy-rule base.

The primary limitation of this study is that the evaluation was conducted entirely in a GUI-based simulation environment without real-hardware implementation or closed-loop time-series measurements.

Consequently, dynamic performance metrics such as rise time, settling time, overshoot, MAE, and RMSE cannot be computed from the available dataset because the simulation evaluates independent fuzzy-rule combinations rather than transient system responses. Future work will therefore focus on implementing the proposed controller on an actual BLDC motor platform to enable comprehensive experimental validation and comparison with conventional controllers such as PID.

5. ACKNOWLEDGEMENT

The authors would like to express their gratitude to the Faculty of Engineering, University of Garut, and the Telecommunications Research Center, National Research and Innovation Agency (BRIN), for providing the facilities and infrastructure that enabled this research to be conducted successfully.

6. REFERENCES

[1] R. Kristiyono and Wiyono, "Autotuning fuzzy PID controller for speed control of BLDC motor," *Journal of Robotics and Control (JRC)*, vol. 2, no. 5, pp. 400–407, Sep. 2021, doi: 10.18196/jrc.25114.

[2] S. GUNTAY and I. SARITAS, "BLDC Motor speed control with dynamic adjustment of PID coefficients: Comparison of fuzzy and classic PID," *International Journal of Applied Methods in Electronics and Computers*, vol. 12, no. 1, pp. 22–32, 2024, doi: 10.58190/ijamec.2024.80.

[3] S. M. Deshmukh and R. P. Mahobia, "BLDC Motor Speed Control with Digital Adaptive ANFIS and Reduced Harmonic Content," *Nanotechnol. Percept.*, vol. 20, no. S4, pp. 11–26, 2024, doi: 10.62441/nano-ntp.v20iS4.2.

[4] J. H. Kim and S. J. Oh, "A fuzzy PID controller for nonlinear and uncertain systems," *Soft comput.*, vol. 4, no. 2, pp. 123–129, 2000, doi: 10.1007/s005000000039.

[5] M. Braae and D. A. Rutherford, "Theoretical and linguistic aspects of the fuzzy logic controller," *Automatica*, vol. 15, no. 5, pp. 553–577, 1979, doi: https://doi.org/10.1016/0005-1098(79)90005-0.

[6] S. Sunardi, A. Yudhana, and F. Furizal, "Impact of Fuzzy Tsukamoto in Controlling Room Temperature and Humidity," *INTENSIF: Jurnal Ilmiah Penelitian dan Penerapan Teknologi Sistem Informasi*, vol. 7, no. 2, pp. 221–242, 2023, doi: 10.29407/intensif.v7i2.19652.

[7] Q.-H. Pham *et al.*, "Design of a Fuzzy Controller for a Heating Furnace System," *Indonesian Journal of Engineering and Science*, vol. 6, no. 2, pp. 125–135, 2025, doi: https://doi.org/10.51630/ijes.vx.xxx.

[8] E. Gowthaman, V. Vinodhini, M. Y. Hussain, S. K. Dhinakaran, and T. Sabarinathan, "Speed Control of Permanent Magnet Brushless DC Motor Using Hybrid Fuzzy Proportional plus Integral plus Derivative Controller," *Energy Procedia*, vol. 117, pp. 1101–1108, 2017, doi: 10.1016/j.egypro.2017.05.234.

[9] A. Varshney, D. Gupta, and B. Dwivedi, "Speed response of brushless DC motor using fuzzy PID controller under varying load condition," *Journal of Electrical Systems and Information Technology*, vol. 4, no. 2, pp. 310–321, 2017, doi: 10.1016/j.jesit.2016.12.014.

[10] N. A. Sulaiman, M. F. Othman, and H. Abdullah, "Fuzzy logic control of centralized chilled water system," *J. Teknol.*, vol. 72, no. 2, pp. 57–62, 2015, doi: 10.11113/jt.v72.3884.

[11] I. Soesanti and R. Syahputra, "A Fuzzy Logic Controller Approach for Controlling Heat Exchanger Temperature," *Journal of Electrical Technology UMY*, vol. 3, no. 4, pp. 117–124, 2019, doi: 10.18196/jet.3462.

[12] R. Bangun *et al.*, "RANCANG BANGUN KONTROLLER PENDINGIN UNTUK UNIT PELTIER BERBASIS FUZZY LOGIC Frima Setyawan Nur Rohman".

[13] H. Yan, Y. Pan, Z. Li, and S. Deng, "Further development of a thermal comfort based fuzzy logic controller for a direct expansion air conditioning system," *Appl. Energy*, vol. 219, pp. 312–324, 2018, doi: https://doi.org/10.1016/j.apenergy.2018.03.045.

[14] Y. Cui, W. Zhang, and B. He, "A Variation-Aware Adaptive Fuzzy Control System for Thermal Management of Microprocessors," *IEEE Trans. Very Large Scale Integr. VLSI Syst.*, vol. 25, no. 2, pp. 683–695, 2017, doi: 10.1109/TVLSI.2016.2596338.

[15] M. H. N. Talib *et al.*, "An improved simplified rules Fuzzy Logic Speed Controller method applied for induction motor drive," *ISA Trans.*, vol. 105, pp. 230–239, 2020, doi: https://doi.org/10.1016/j.isatra.2020.05.040.

[16] N. Öztürk and E. Çelik, "Speed control of permanent magnet synchronous motors using fuzzy controller based on genetic algorithms," *International Journal of Electrical Power & Energy Systems*, vol. 43, no. 1, pp. 889–898, 2012, doi: https://doi.org/10.1016/j.ijepes.2012.06.013.

[17] K. Belarbi, F. Titel, W. Bourebia, and K. Benmahammed, "Design of Mamdani fuzzy logic controllers with rule base minimisation using genetic algorithm," *Eng. Appl. Artif. Intell.*, vol. 18, no. 7, pp. 875–880, 2005, doi: https://doi.org/10.1016/j.engappai.2005.03.003.

[18] T. J. Ross, *Fuzzy Logic with Engineering Applications*. Wiley, 2016. [Online]. Available: https://books.google.co.id/books?id=ijsbDQAAQBAJ

APPENDIX A

Appendix A presents the complete fuzzy rule base consisting of all 81 rule combinations generated from the four fuzzy input variables (E, ΔE, T, and ΔT). Each rule specifies the corresponding singleton outputs for the motor PWM and cooling-fan PWM used by the proposed fuzzy inference system.

Table A1. Complete 81-Rule Base of the Proposed Fuzzy Controller

Rule No	RPM Error (E)	Change in RPM Error (ΔE)	Temperature Level (T)	Change in Temperature (ΔT)	Motor PWM	Cooling Fan PWM
1	NEG	NEG	LOW	NEG	100	20
2	NEG	NEG	LOW	ZERO	100	20
3	NEG	NEG	LOW	POS	100	80
4	NEG	ZERO	LOW	NEG	100	20
5	NEG	ZERO	LOW	ZERO	100	20
6	NEG	ZERO	LOW	POS	100	80
7	NEG	POS	LOW	NEG	150	20
8	NEG	POS	LOW	ZERO	150	20
9	NEG	POS	LOW	POS	150	80
10	ZERO	NEG	LOW	NEG	150	20
11	ZERO	NEG	LOW	ZERO	150	20
12	ZERO	NEG	LOW	POS	150	80
13	ZERO	ZERO	LOW	NEG	150	20
14	ZERO	ZERO	LOW	ZERO	150	20
15	ZERO	ZERO	LOW	POS	150	80
16	ZERO	POS	LOW	NEG	255	20
17	ZERO	POS	LOW	ZERO	255	20
18	ZERO	POS	LOW	POS	255	80
19	POS	NEG	LOW	NEG	255	20
20	POS	NEG	LOW	ZERO	255	20
21	POS	NEG	LOW	POS	255	80
22	POS	ZERO	LOW	NEG	255	20
23	POS	ZERO	LOW	ZERO	255	20
24	POS	ZERO	LOW	POS	255	80
25	POS	POS	LOW	NEG	255	20
26	POS	POS	LOW	ZERO	255	20
27	POS	POS	LOW	POS	255	80
28	NEG	NEG	MED	NEG	100	80
29	NEG	NEG	MED	ZERO	100	80
30	NEG	NEG	MED	POS	100	255
31	NEG	ZERO	MED	NEG	100	80
32	NEG	ZERO	MED	ZERO	100	80
33	NEG	ZERO	MED	POS	100	255
34	NEG	POS	MED	NEG	150	80
35	NEG	POS	MED	ZERO	150	80
36	NEG	POS	MED	POS	150	255
37	ZERO	NEG	MED	NEG	150	80

38	ZERO	NEG	MED	ZERO	150	80
39	ZERO	NEG	MED	POS	150	255
40	ZERO	ZERO	MED	NEG	150	80
41	ZERO	ZERO	MED	ZERO	150	80
42	ZERO	ZERO	MED	POS	150	255
43	ZERO	POS	MED	NEG	255	80
44	ZERO	POS	MED	ZERO	255	80
45	ZERO	POS	MED	POS	255	255
46	POS	NEG	MED	NEG	255	80
47	POS	NEG	MED	ZERO	255	80
48	POS	NEG	MED	POS	255	255
49	POS	ZERO	MED	NEG	255	80
50	POS	ZERO	MED	ZERO	255	80
51	POS	ZERO	MED	POS	255	255
52	POS	POS	MED	NEG	255	80
53	POS	POS	MED	ZERO	255	80
54	POS	POS	MED	POS	255	255
55	NEG	NEG	HIGH	NEG	100	255
56	NEG	NEG	HIGH	ZERO	100	255
57	NEG	NEG	HIGH	POS	100	255
58	NEG	ZERO	HIGH	NEG	100	255
59	NEG	ZERO	HIGH	ZERO	100	255
60	NEG	ZERO	HIGH	POS	100	255
61	NEG	POS	HIGH	NEG	150	255
62	NEG	POS	HIGH	ZERO	150	255
63	NEG	POS	HIGH	POS	150	255
64	ZERO	NEG	HIGH	NEG	150	255
65	ZERO	NEG	HIGH	ZERO	150	255
66	ZERO	NEG	HIGH	POS	150	255
67	ZERO	ZERO	HIGH	NEG	150	255
68	ZERO	ZERO	HIGH	ZERO	150	255
69	ZERO	ZERO	HIGH	POS	150	255
70	ZERO	POS	HIGH	NEG	255	255
71	ZERO	POS	HIGH	ZERO	255	255
72	ZERO	POS	HIGH	POS	255	255
73	POS	NEG	HIGH	NEG	255	255
74	POS	NEG	HIGH	ZERO	255	255
75	POS	NEG	HIGH	POS	255	255
76	POS	ZERO	HIGH	NEG	255	255
77	POS	ZERO	HIGH	ZERO	255	255
78	POS	ZERO	HIGH	POS	255	255
79	POS	POS	HIGH	NEG	255	255
80	POS	POS	HIGH	ZERO	255	255
81	POS	POS	HIGH	POS	255	255

(JOURNAL ENGINEERING DESIGN AND TECHNOLOGY)

Journal Engineering Design and Technology
Vol. 26 No.2 July 2026 ; p. 133 - 147
Journal Homepage : http://ojs2.pnb.ac.id/index.php/LOGIC
p-ISSN : 1412-114X e-ISSN : 2580-5649

A Review Study of Influencing Factors and Conceptual Scaling Framework for Spray Drying Assisted by Ultrasonic Vibrating Mesh Atomizers

I Dewa Gede Agus Tri Putra[1,2], Wayan Nata Septiadi [3)*], Dewa Ngakan Ketut Putra Negara [3)] and Tjokorda Gde Tirta Nindhia [3)]

1) Refrigeration and Air Conditioning Study Program, Department of Mechanical Engineering, Politeknik Negeri Bali, Bukit Jimbaran, Bali-Indonesia.
2) Doctoral Study Program of Engineering Science, Faculty of Engineering, Udayana University, Bali-Indonesia.
3) Mechanical Engineering Department, Faculty of Engineering Udayana University, Bali-Indonesia.

Correponding email [*)] : wayan.nata@unud.ac.id

Abstract. Spray drying is widely used in the pharmaceutical, food, and chemical industries for converting liquid feed into dry particulate products. However, conventional spray drying systems commonly generate broad droplet size distributions and exhibit limited capability for producing submicron particles. To overcome these limitations, ultrasonic vibrating mesh atomizers have recently attracted significant attention due to their ability to generate highly uniform droplets with relatively low energy consumption and improved atomization controllability. Previous studies have investigated the influence of individual operating parameters on ultrasonic spray drying performance, particularly using laboratory-scale systems such as the Büchi Nano Spray Dryer B-90. Nevertheless, existing literature remains fragmented, with limited efforts to systematically establish the relative importance of governing parameters or to develop a unified conceptual framework for scaling ultrasonic spray drying systems from laboratory to industrial applications. This study addresses this gap by conducting a systematic literature-based parametric analysis of spray drying systems assisted by piezoelectric vibrating mesh atomizers. Experimental studies employing the Büchi Nano Spray Dryer B-90 were critically reviewed to identify the dominant factors controlling droplet formation, atomization stability, and particle generation behaviour. The analysed parameters were classified into three principal categories: atomization parameters, fluid properties, and drying process parameters. The analysis demonstrates that mesh aperture size, ultrasonic vibration frequency, and spray throughput are the primary parameters governing droplet formation and particle size distribution. Fluid properties, including viscosity, surface tension, and feed concentration, strongly influence atomization stability through their effects on dimensionless parameters such as the Weber number and Ohnesorge number. In contrast, drying parameters, including inlet air temperature and gas flow rate, predominantly affect evaporation kinetics and particle morphology rather than the initial droplet generation process. The reviewed studies further indicate that ultrasonic atomization commonly operates within a regime characterized by moderate Weber numbers and relatively low Ohnesorge numbers, consistent with capillary wave breakup mechanisms. Based on these findings, a conceptual scaling framework is proposed in which atomization similarity, fluid dynamic similarity, and drying conditions must be simultaneously considered to achieve reliable scale-up of ultrasonic spray drying systems

Keywords : Vibrating Mesh Atomizer, Spray Drying, Ultrasonic, Scaling Technique

1. INTRODUCTION

Spray drying has long been recognized as one of the most versatile and widely used technologies for transforming liquid feed solutions into dry particulate products. The technique is extensively applied in various industrial sectors, including pharmaceuticals, food processing, biotechnology, and advanced materials engineering. Conventional spray drying systems typically employ pressure nozzles or rotary atomizers to generate droplets, which subsequently undergo rapid solvent evaporation within a heated drying chamber. Although these systems are well established for large-scale production, controlling droplet size distribution and producing submicron particles remain significant challenges due to the inherent limitations of traditional atomization mechanisms.[1]-[4]

In recent years, ultrasonic atomization technologies have attracted increasing attention as an alternative approach for generating highly controlled droplets. Among these technologies, the vibrating mesh atomizer has emerged as a particularly promising solution due to its ability to produce narrow droplet size distributions with relatively low energy consumption [5]-[7]. This atomization mechanism relies on the oscillation of a piezoelectric element coupled with a micro-perforated mesh, through which the liquid feed is forced under ultrasonic vibration. As a result, droplets are generated through capillary wave instabilities at the liquid–mesh interface, enabling precise control of droplet formation.[5]-[13]

A significant advancement in this field was the development of the Büchi Nano Spray Dryer B-90, which integrates a piezoelectric vibrating mesh atomizer into a laboratory-scale spray drying system. This technology enables the production of submicron particles and nanoparticles with improved control over particle size distribution compared to conventional spray drying systems [14]-[16]. These capabilities have made the system particularly attractive for pharmaceutical particle engineering, nanoencapsulation, and also the stabilization of bioactive compounds. Beyond its application as a laboratory-scale particle engineering tool, the Buchi B-90 platform also provides valuable insights into the fundamental physics of ultrasonic atomization and droplet formation. Because the atomization process is governed by well-defined dimensionless parameters such as the Weber number and Ohnesorge number, experimental results obtained using the Büchi B-90 system can be used to establish scaling relationships for spray drying processes. Maintaining similar dimensionless parameters allows the preservation of atomization mechanisms when transitioning from laboratory-scale equipment to pilot-scale or industrial-scale spray dryers. Consequently, research conducted using the B-90 system plays an important role in bridging the gap between fundamental atomization studies and the design of industrial spray drying equipment. By systematically investigating the effects of ultrasonic frequency, mesh geometry, feed properties, and operating conditions, researchers can develop scaling frameworks that enable consistent droplet formation across different process scales. Such knowledge is essential for the development of next-generation spray drying technologies capable of producing nanoparticles and highly engineered particles in industrial applications. Therefore, understanding the atomization mechanisms and scaling principles derived from studies using the B-90 system is crucial for advancing the design of industrial spray drying equipment. The insights gained from these studies provide a foundation for improving droplet control, enhancing particle engineering capabilities, and ultimately enabling the efficient production of advanced functional powders in large-scale industrial processes. [17]-[25]

Although numerous studies have investigated individual operating parameters in ultrasonic spray drying systems, existing research remains largely fragmented and application-oriented [26]-[28]. Most previous studies focused on formulation development, nanoparticle production, or optimization of isolated process variables using laboratory-scale equipment such as the Büchi Nano Spray Dryer B-90 (see Tabel 1). However, no previous review has systematically established a hierarchical relationship among atomization parameters, fluid properties, and drying conditions while simultaneously proposing a conceptual scaling framework based on dimensionless similarity principles for ultrasonic spray drying systems. Consequently, the fundamental relationships governing scale-up from laboratory-scale ultrasonic spray dryers to industrial-scale applications remain insufficiently understood.

The objective of this study is to investigate the key parameters governing the scaling behaviour of spray drying systems assisted by a piezoelectric mesh atomizer. In recent years, vibrating mesh atomization has emerged as a promising technique for generating highly uniform droplets with narrow size distributions, which is particularly advantageous for producing submicron and micron-scale particles. However, despite the growing number of laboratory-scale studies, the fundamental parameters that control the scalability of ultrasonic spray drying systems remain insufficiently understood. Therefore, this study aims to conduct a comprehensive parametric analysis of the operational variables influencing droplet formation, atomization stability, and particle characteristics in spray drying processes assisted by piezoelectric mesh atomizers. Particular attention is given to identifying the relationships between atomization parameters, fluid properties, and drying conditions that govern the droplet formation mechanism and ultimately determine the particle size distribution. Furthermore, the study seeks to establish a conceptual scaling framework that links laboratory-scale experimental observations with potential industrial spray drying applications. By analysing the effects of key parameters such as mesh aperture size, vibration frequency, feed properties, and drying conditions, this work aims to determine the dominant variables controlling atomization performance and particle formation in ultrasonic spray drying systems. Ultimately, the findings of this research are expected to contribute to the development of scaling strategies for spray drying technologies employing piezoelectric mesh atomizers, thereby supporting the design of next-generation spray drying equipment capable of producing finely controlled powders in industrial-scale processes.

2. METHODS

This study employed a systematic literature-based parametric analysis to identify the key operational and physical parameters governing droplet generation and particle formation in spray drying systems utilizing vibrating mesh atomizers. Particular emphasis was placed on studies conducted using the Büchi Nano Spray Dryer B-90, as this system represents one of the most widely used laboratory-scale spray drying platforms employing ultrasonic vibrating mesh atomization.

The methodological framework was designed to extract, classify, and analyze experimental parameters reported in published research in order to determine the dominant variables influencing spray drying performance. By synthesizing findings from multiple studies, the research aims to establish a parameter hierarchy and develop insights into potential scaling strategies applicable to industrial spray drying systems. A comprehensive literature search was conducted using major scientific databases including Scopus, Web of Science, Google Scholar, and ScienceDirect. The search focused on peer-reviewed journal articles published between 2010 and 2024, corresponding to the period following the introduction of the Büchi Nano Spray Dryer B-90. The search keywords included combinations of; "nano spray dryer B-90", "vibrating mesh atomizer spray drying", "ultrasonic atomization spray drying", "nano spray drying particle engineering", and "B-90 spray drying parameters". Articles were included in the analysis if they satisfied the following criteria:

1. The study employed the Büchi Nano Spray Dryer B-90 as the primary spray drying equipment.
2. Experimental conditions and operating parameters were explicitly reported.
3. The study analyzed particle characteristics, droplet formation, or process performance.
4. The research was published in peer-reviewed scientific journals.

Studies were excluded if they did not provide sufficient information on process parameters or if they focused solely on formulation chemistry without reporting spray drying operating conditions. Then, the selected articles and relevant experimental parameters were systematically extracted and categorized into three major groups: Atomization Parameters, Feed and Fluid Properties, Drying Process Parameters. Although the present study synthesizes a wide range of experimental findings from the literature, certain limitations must be acknowledged. Differences in feed formulation, measurement techniques, and experimental setups across studies may introduce variability in reported results. Therefore, the conclusions derived from the parametric analysis should be interpreted as general trends rather than absolute predictive correlations. Nevertheless, by integrating results from multiple studies, the present methodology provides a comprehensive overview of the key parameters governing vibrating mesh spray drying systems and offers valuable insights for future development of industrial-scale ultrasonic spray drying technologies.

3. RESULTS

3.1 An Overview of Industrial Spray Drying Assisted by Ultrasonic Atomization

An industrial spray dryer is composed of several integrated components that work together to transform a liquid feed into dry powder through atomization and rapid solvent evaporation. The performance and efficiency of the spray drying process strongly depend on the proper design and operation of these components. In general, the system consists of a feed preparation unit, pumping system, atomization device, air heating unit, drying chamber, particle separation system, powder collection unit, and exhaust air system (see Figure 1). Each of these components plays a critical role in controlling the droplet formation, heat transfer, mass transfer, and powder recovery processes.[29], [30].

The feed preparation unit is responsible for storing and conditioning the liquid feed before it enters the spray dryer. Typically, the feed solution or suspension is stored in a feed tank equipped with an agitation system to maintain uniformity and prevent sedimentation of solid particles. In many industrial applications, the feed preparation stage also includes filtration and deaeration systems to remove impurities and entrapped air bubbles that could interfere with the atomization process. [30] The physical properties of the feed, such as viscosity, surface tension, and solids concentration, must be carefully controlled during this stage because they significantly influence droplet formation and drying behavior within the spray dryer.[4]

The feed pumping system transports the prepared liquid feed from the storage tank to the atomizer at a controlled flow rate and pressure. Industrial spray drying systems commonly use positive displacement pumps or high-pressure pumps depending on the type of atomizer used. The feed flow rate is a crucial operating parameter because it determines the amount of liquid introduced into the drying chamber and influences the residence time of droplets within the drying environment. Precise control of the pumping system is therefore necessary to ensure stable atomization and prevent operational problems such as flooding or incomplete drying [24], [31].

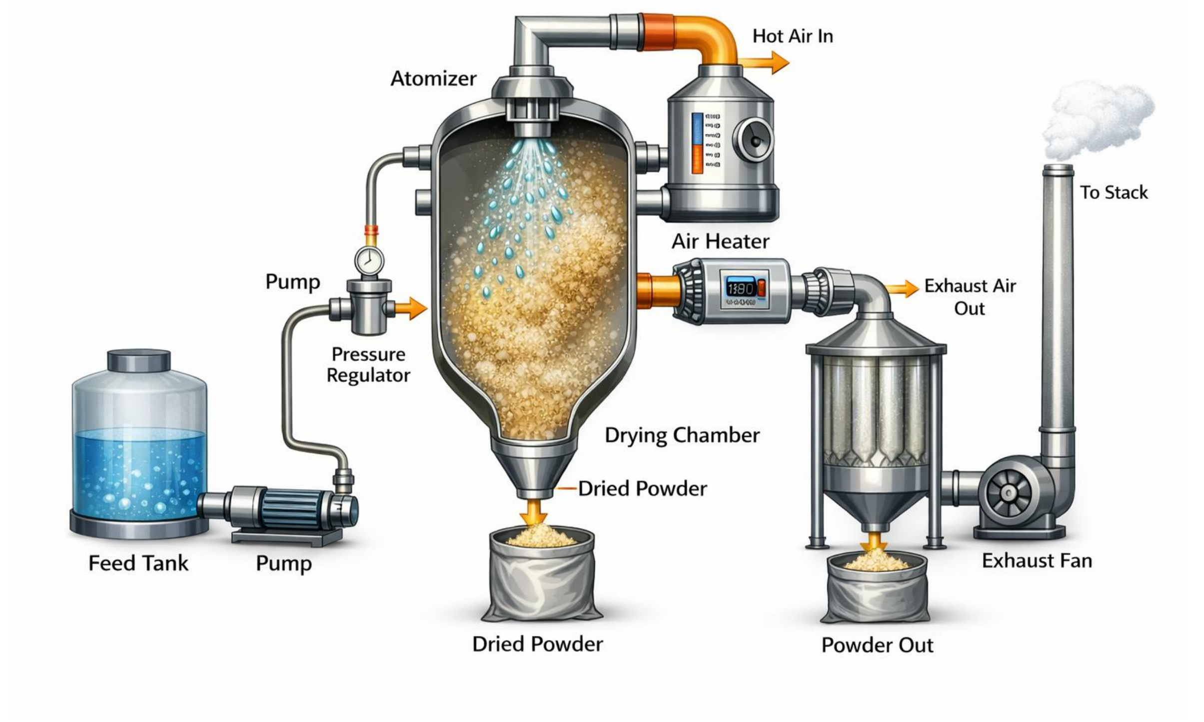

Figure 1 Schematic of industrial spray drying system

The atomizer is considered the most critical component of a spray dryer because it is responsible for converting the liquid feed into fine droplets. The droplet size generated during atomization largely determines the final particle size distribution and drying rate. Industrial spray dryers typically utilize three main types of atomizers: pressure nozzle atomizers, rotary atomizers, and ultrasonic or vibrating mesh atomizers. Pressure nozzles atomize the liquid by forcing it through a small orifice under high pressure, while rotary atomizers use centrifugal forces generated by a rapidly rotating disk to disperse the liquid. Ultrasonic atomizers, on the other hand, generate droplets through capillary wave breakup induced by high-frequency vibration. The selection of the atomizer type significantly affects the droplet size distribution and overall drying efficiency.[13], [32]

The air heating system supplies the thermal energy required for rapid solvent evaporation from the atomized droplets. Ambient air is first filtered to remove contaminants and then heated using various heating methods such as electric heaters, steam heat exchangers, or gas-fired burners. The heated air is subsequently introduced into the drying chamber as the drying gas. The temperature of the inlet air is one of the most important process parameters in spray drying because it directly influences the evaporation rate, drying kinetics, and final moisture content of the powder. Careful control of the air temperature is therefore required to achieve efficient drying while preventing thermal degradation of temperature-sensitive materials [33].

The drying chamber is the central vessel where the atomized droplets come into contact with the hot drying air, resulting in rapid evaporation of the solvent and formation of solid particles. Industrial spray drying chambers are typically designed as large cylindrical or conical vessels that provide sufficient residence time for the droplets to dry completely before reaching the chamber walls or outlet. Within the drying chamber, complex interactions occur between heat transfer, mass transfer, droplet evaporation, and particle formation. The geometry and size of the chamber play an important role in determining the flow patterns of the drying air and the residence time distribution of droplets. Following the drying process, the dried particles must be separated from the exhaust air stream using an appropriate particle separation system. The most commonly used separation device in industrial spray drying is the cyclone separator, which utilizes centrifugal forces to separate solid particles from the gas stream. As the air-particle mixture enters the cyclone, the swirling motion forces particles toward the outer wall of the cyclone, where they lose momentum and fall into a collection hopper [34]. Cyclone separators are particularly effective for recovering particles with relatively large diameters, while finer particles may require additional separation devices such as bag filters or electrostatic precipitators. The powder collection system is designed to collect and store the dried powder after separation from the air stream. In industrial spray drying plants, the powder is typically discharged from the cyclone separator into collection bins or storage silos. Automated discharge mechanisms are often used to enable continuous operation and prevent powder accumulation inside the system. Maintaining efficient powder collection is essential for maximizing product yield and minimizing product losses during the drying process. Finally, the exhaust air system is responsible for removing the humid air generated during the drying process from the system. This subsystem usually includes exhaust fans, ducts, and air filtration units to ensure stable airflow within the spray dryer and to prevent the release of fine particles into the environment. Proper design of the exhaust air system is important not only for maintaining process stability but also for meeting environmental and safety regulations in industrial operations [35].

The process converts liquid feed into dry particulate products through atomization followed by rapid solvent evaporation in a heated gas stream. Conventional spray drying systems typically rely on pressure nozzles or rotary atomizers to generate droplets. While these atomization methods are well established for large-scale production, they often produce relatively broad droplet size distributions and require high operating pressures or rotational energy to achieve fine droplet formation [36]. To overcome these limitations, ultrasonic atomization has emerged as an alternative approach for generating highly controlled droplets with narrow size distributions. In particular, vibrating mesh atomizers utilize piezoelectric actuators to excite micro-perforated meshes at ultrasonic frequencies, forcing liquid through micron-scale apertures and producing droplets through capillary-wave instability [37]. This mechanism allows droplet formation to be governed primarily by mesh geometry, vibration frequency, and fluid properties, enabling more precise control over droplet size compared with conventional atomizers.

3.2 Summary of Parametric Study in Spray Drying

A major technological advancement in this field is represented by the development of the Büchi Nano Spray Dryer B-90, which integrates vibrating mesh atomization with a laboratory-scale spray drying system. The B-90 platform has enabled the production of submicron particles and nanoparticles with significantly narrower size distributions than those produced by traditional laboratory spray dryers. Numerous studies have demonstrated its capability to generate droplets typically ranging from approximately 8–21 µm, resulting in dried particles in the range of several hundred nanometres to a few micrometres depending on feed composition and operating conditions. Consequently, the B-90 system has become a widely used experimental platform for nanoparticle production, nanoencapsulation of bioactive compounds, and pharmaceutical particle engineering.[18]

Table 1 Summary of key parametric studies using the Büchi Nano Spray Dryer B-90

No	Reference (Author–Year)	Material / Feed Solution	Mesh Size / Frequency	Inlet Temp (°C)	Feed Rate	Gas Flow	Key Parametric Variables	Particle Size / Result
1	Li et al., 2010 [38]	Model pharmaceutical compounds	Mesh 4–5.5 µm (~120 kHz)	90–120	20–40 mL/h	~100 L/min	Feed concentration, mesh size	Submicron particles (300 nm–2 µm)
2	Harsha et al., 2015 [39]	Drug-loaded nanospheres	Mesh 4 µm	100	25 mL/h	100 L/min	Polymer concentration, drug loading	High encapsulation yield (~83%) and controlled release behavior
3	Strob et al., 2018[40]	Submicron spray-dried particles	Mesh 5.5 µm	90–110	30 mL/h	100 L/min	Mesh aperture size, feed composition	Submicron particle formation suitable for drug delivery
4	Chopde et al., 2020 [14]	Bioactive compounds / nutraceuticals	Mesh 4–7 µm	80–120	20–50 mL/h	80–120 L/min	Feed concentration and viscosity	Nanoparticles <1 µm with improved bioavailability
5	Almansour et al., 2022 [41]	Pharmaceutical particles	Mesh 5.5 µm	100–120	25–40 mL/h	100–120 L/min	Drying temperature and mesh pore size	Particle engineering at submicron scale
6	Hwang et al., 2023 [42]	Cellulose nanocrystal suspension	Mesh 4 µm	100	30 mL/h	100–120 L/min	Gas flow rate	Gas flow had minimal influence on particle size
7	Bürki et al., 2011 [43]	Protein stabilization	Mesh 4 µm	100	20–30 mL/h	100 L/min	Stabilizer concentration	Stable protein nanoparticles
8	Lee et al., 2011 [44]	Protein nanoparticles	Mesh 4–5 µm	90–110	20–35 mL/h	100 L/min	Protein concentration	Narrow particle size distribution
9	Schmid et al., 2012 [45]	Pharmaceutical excipients	Mesh 5.5 µm	100	30 mL/h	100 L/min	Drying temperature	Improved powder stability
10	Gu et al., 2015 [46]	Amorphous solid dispersions	Mesh 4–5.5 µm	90–120	25–40 mL/h	100 L/min	Feed composition	Particle size 2–10 µm depending on formulation
11	Arpagaus et al., 2017 [47]	Nano-encapsulated bioactives	Mesh 4–7 µm	80–110	20–40 mL/h	100 L/min	Carrier composition	Enhanced encapsulation efficiency
12	Kyriakoudi et al., 2018 [18]	Saffron extract encapsulation	Mesh 4 µm	90–110	25–35 mL/h	100 L/min	Carrier type	Improved stability of bioactive compounds
13	Shehata et al., 2019 [48]	Drug nanoparticles	Mesh 4–5 µm	100–120	25–40 mL/h	100–120 L/min	Polymer ratio	Enhanced drug dissolution

No	Reference (Author–Year)	Material / Feed Solution	Mesh Size / Frequency	Inlet Temp (°C)	Feed Rate	Gas Flow	Key Parametric Variables	Particle Size / Result
14	Gómez-Mascaraque et al., 2020 [49]	Biopolymer nanoparticles	Mesh 5.5 µm	100	30 mL/h	100 L/min	Feed viscosity	Increased viscosity increased particle size
15	Baldelli et al., 2020[50]	Pharmaceutical formulations	Mesh 4–5.5 µm	100	20–35 mL/h	100 L/min	Spray throughput	High throughput reduced powder yield

The studies summarized in Table 1 highlight the key operational parameters influencing particle formation in nano spray drying systems using ultrasonic vibrating mesh atomizers. Most investigations report that mesh aperture size and feed composition are the dominant parameters controlling droplet formation and final particle size distribution. For example, Li et al. (2010) demonstrated that mesh apertures between 4 and 5.5 µm can generate droplets capable of producing submicron particles in the range of 300 nm to 2 µm [38] . Similarly, Strob et al. (2018) confirmed that mesh geometry strongly affects droplet size and particle formation during ultrasonic atomization [40]. In addition, several studies have shown that feed concentration and viscosity significantly influence particle size due to their effects on droplet shrinkage during solvent evaporation. In contrast, parameters such as drying gas flow rate appear to have a relatively minor influence on particle size, as demonstrated by Hwang et al. (2023), who reported that variations in gas flow mainly affected drying dynamics rather than droplet formation. A parametric study based on previously published experimental investigations using the Büchi Nano Spray Dryer B-90 indicates that several operating parameters significantly influence particle formation during spray drying [42]. Among these parameters, the mesh aperture size and the ultrasonic vibration frequency play a dominant role in controlling droplet generation. The piezoelectric mesh atomizer operates typically within a frequency range of 80–140 kHz [5], producing droplets with mean diameters between approximately 3 and 15 µm, which subsequently dry into particles with sizes ranging from 200 nm to several micrometers. In addition, process variables such as inlet temperature, feed concentration, and drying gas flow rate influence the evaporation kinetics and the morphology of the final particles. Most studies reported that variations in mesh size and feed concentration strongly affect particle size distribution, while drying gas flow rate has a relatively smaller impact on particle morphology. In table 2 we can adjust several parameters on Büchi Nano Spray Dryer B-90 to conducted an experiment to innovative model of spray drying system [17], [18].

Table 2 Summary of controllable parameter in Buchi B-90

Parameter	Typical Range in B-90
Piezoelectric frequency	80–140 kHz
Mesh pore size	4 – 7 µm
Inlet temperature	80 – 120 °C
Feed rate	20 – 50 mL/h
Gas flow rate	80 – 160 L/min
Particle size	200 nm – 5 µm

Experimental studies conducted using the Büchi Nano Spray Dryer B-90 have provided valuable insights into the relationship between atomization parameters, feed properties, and particle formation. By analysing the experimental findings reported in these studies, a conceptual scaling framework can be developed to identify the dominant parameters controlling droplet generation and particle formation in ultrasonic spray drying systems.

3.3 Estimated We–Oh Operating Regime for Ultrasonic Atomizer

In ultrasonic atomization systems, droplet formation is governed by complex interactions between acoustic energy, liquid properties, and operational conditions. Therefore, evaluating the influence of individual parameters is essential to establish a deeper understanding of the droplet generation mechanism and to identify optimal operating conditions for producing particles with controlled size distribution. The present parametric study focuses on several critical variables including ultrasonic vibration frequency, liquid feed rate, electrical input power, and liquid physical properties such as viscosity and surface tension. These parameters directly influence the atomization process, droplet size distribution, and the overall efficiency of spray drying systems employing piezoelectric mesh atomizers.

The vibration frequency of the ultrasonic mesh atomizer plays a dominant role in determining droplet size during ultrasonic atomization. The oscillatory motion of the piezoelectric actuator generates capillary waves on the liquid interface located above the mesh apertures. When the amplitude of these waves exceeds a critical threshold, the liquid disintegrates into droplets through the instability of the capillary wave crests. Theoretical analyses and experimental observations suggest that the droplet diameter produced by ultrasonic atomization is inversely proportional to the operating frequency. This relationship can be expressed using the Lang-type scaling law[51], [52]:

$$d = \left(\frac{8\pi\sigma}{\rho f^2}\right)^{1/3} \quad (1)$$

where:

d= droplet diameter
σ= surface tension of the liquid
ρ= liquid density
f= ultrasonic frequency

This relationship indicates that higher vibration frequencies lead to smaller droplet diameters due to the formation of shorter wavelength capillary waves. Consequently, frequency variation is one of the most effective approaches for controlling droplet size distribution in piezo electric mesh atomizer assisted spray drying systems.[51], [53]

The liquid feed rate significantly affects the stability of atomization and droplet generation efficiency. In piezoelectric mesh atomizers, liquid is supplied to the vibrating mesh surface where it forms a thin liquid film before passing through the micro-apertures of the mesh. The thickness of this liquid film is directly influenced by the feed rate [54]. At excessively high feed rates, the liquid layer becomes thicker and may dampen the vibration transmitted from the piezoelectric actuator. This damping effect reduces the effective acoustic energy reaching the liquid surface, leading to irregular droplet formation or increased droplet size. Conversely, lower feed rates generally promote more stable atomization conditions by allowing efficient energy transfer and uniform droplet ejection through the mesh apertures. Therefore, an optimal feed rate range must be determined to maintain a balance between droplet production rate and atomization stability.

The electrical input power supplied to the piezoelectric actuator determines the amplitude of ultrasonic vibration and the intensity of acoustic energy applied to the liquid. Higher input power increases the vibration amplitude, which enhances the capillary wave instability responsible for droplet formation. An increase in acoustic intensity generally leads to an increase in droplet generation rate and atomization throughput. However, excessive power input may introduce undesirable effects such as unstable atomization behaviour, droplet formation, or increased thermal loading of the piezoelectric element. Therefore, evaluating the influence of input power is essential for determining the energy-efficient operating conditions of the piezoelectric mesh atomizer system.[12], [55], [56]

Dimensionless analysis provides a fundamental framework for understanding droplet formation mechanisms and for developing scaling strategies in spray drying systems. In ultrasonic atomization, droplet generation is governed by the complex interaction between inertial forces, viscous forces, and surface tension forces acting at the liquid interface. These interactions can be quantitatively described using dimensionless parameters, particularly the Weber number (We) and the Ohnesorge number (Oh), which are widely applied in atomization studies [52], [57], [58]. The Weber number represents the ratio between inertial forces and surface tension forces and can be expressed as:

$$We = \frac{\rho u^2 d}{\sigma} \quad (2)$$

where ρ is the liquid density, u is the characteristic velocity of the liquid, d is the characteristic length scale (often the droplet diameter or nozzle dimension), and σ is the surface tension. In atomization processes, the Weber number indicates whether the inertial forces acting on the liquid are sufficient to overcome surface tension and promote droplet breakup. Moreover, The Ohnesorge number is defined as:

$$Oh = \frac{\mu}{\sqrt{\rho\sigma d}} \quad (3)$$

where μ represents the dynamic viscosity of the liquid. This dimensionless parameter characterizes the relative importance of viscous forces compared with inertial and capillary forces. In the context of ultrasonic atomization, the Ohnesorge number determines the extent to which viscous damping suppresses the growth of capillary waves on the liquid surface. Scaling of spray drying processes is traditionally based on maintaining similar thermal histories, residence times, and droplet size distributions between laboratory-scale and industrial-scale systems. However, when ultrasonic atomization is employed, additional parameters related to the vibrating mesh atomizer must be considered. Unlike conventional pressure nozzle atomizers, vibrating mesh atomizers generate droplets through capillary-wave-driven ejection induced by ultrasonic vibration. Consequently, droplet formation is governed not only by flow conditions but also by atomizer geometry, vibration frequency, and fluid properties.

The droplet formation mechanism in piezoelectric mesh atomizers, is typically associated with capillary wave breakup induced by high-frequency oscillations. When the ultrasonic vibration excites the liquid surface, capillary waves are generated. As the wave amplitude increases beyond a critical threshold, the crests of the waves detach from the surface, forming droplets. The stability of this mechanism depends strongly on the balance between the Weber and Ohnesorge numbers. Experimental investigations of ultrasonic atomization have shown that efficient droplet formation occurs within a specific region of the Weber–Ohnesorge parameter space. When the Ohnesorge number is too large, viscous forces dampen the capillary wave growth, preventing efficient droplet ejection [51], [59]. Conversely, when the Weber number is too small, surface tension dominates and inhibits droplet breakup. Therefore, maintaining an appropriate balance between these parameters is essential for stable atomization. Several published studies have confirmed the relevance of this dimensionless framework for vibrating mesh atomizers used in spray drying. Investigations using laboratory-scale nano spray dryers have demonstrated that mesh aperture size and fluid properties strongly influence droplet size and atomization stability [60]. Because these parameters directly affect the characteristic length scale and viscous properties of the liquid, they alter the corresponding Weber and Ohnesorge numbers. Consequently, the operating regime of the atomizer can shift between efficient droplet formation and unstable atomization depending on the fluid formulation and operating conditions.

The Weber–Ohnesorge framework provides a valuable guideline for maintaining dynamic similarity between laboratory-scale and industrial spray drying systems. If the Weber and Ohnesorge numbers remain within the same regime during scale-up, the fundamental droplet formation mechanism can be preserved. This principle suggests that scaling strategies for ultrasonic spray drying should focus on maintaining similar relationships between atomization geometry, fluid properties, and operating conditions rather than relying solely on geometric scaling. Furthermore, the dimensionless analysis highlights the dominant role of atomization parameters in determining droplet size distribution. Parameters such as mesh aperture size and vibration frequency define the characteristic droplet formation scale, while fluid properties such as viscosity and surface tension determine the atomization regime through their influence on the Ohnesorge number. Drying parameters, including inlet temperature and gas flow rate, mainly affect solvent evaporation and particle formation but do not directly control droplet generation. Therefore, the Weber–Ohnesorge framework offers a useful theoretical basis for interpreting experimental results obtained in ultrasonic spray drying studies and for developing scaling strategies for industrial spray drying systems. By maintaining appropriate ranges of these dimensionless parameters, it is possible to preserve droplet formation behaviour across different equipment scales and thereby achieve consistent particle characteristics in large-scale spray drying processes. Figure 2 shows The Weber–Ohnesorge regime map for ultrasonic vibrating mesh atomizer as framework of scaling technique in ultrasonic spray drying.

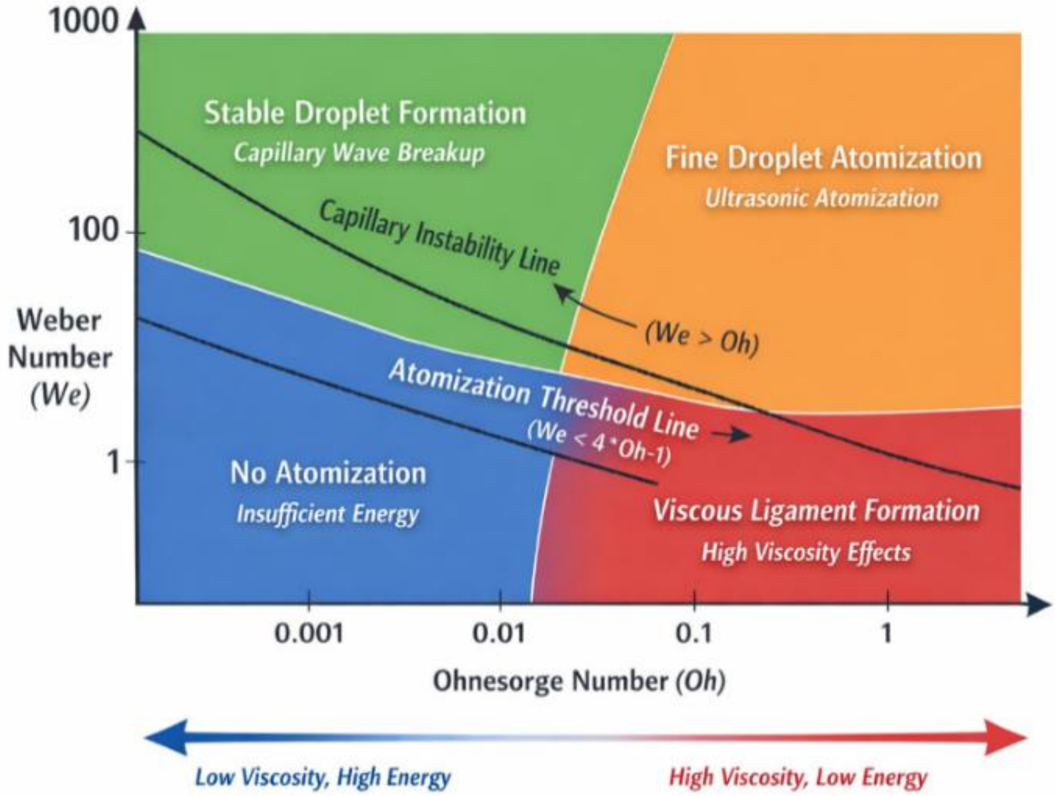

Figure 2 The Weber–Ohnesorge regime map for ultrasonic vibrating mesh atomizer

Based on operating conditions commonly reported in the literature for the Büchi Nano Spray Dryer B-90, approximate Weber and Ohnesorge ranges can be estimated to characterize the atomization regime associated with ultrasonic vibrating mesh atomization. Typical droplet diameters reported for the B-90 system range from approximately 8–21 µm, while atomization frequencies are commonly around 100-140 kHz [7], [12]. Assuming water-like fluid properties with density of approximately 1000 kg/m³, surface tension of 0.072 N/m, and viscosity ranging between 1–10 mPa·s depending on feed composition, estimated Weber numbers are typically within the range of approximately 1–10, while Ohnesorge numbers generally range from 0.01–0.1 [52]. These values are consistent with capillary-wave-driven atomization regimes reported in ultrasonic atomization studies [37]. The moderate Weber number regime indicates sufficient inertial force to overcome surface tension and initiate droplet detachment, whereas relatively low Ohnesorge numbers suggest that viscous damping remains limited and does not suppress capillary wave growth. Consequently, these dimensionless ranges support the interpretation that stable droplet generation in the Büchi B-90 system primarily occurs through capillary wave breakup mechanisms.

4 Disscussion

4.1 Interpretation of Parameter Hierarchy

Vibrating mesh atomizer which is used in the Büchi Nano Spray Dryer B-90, droplet generation typically occurs within a regime characterized by moderate Weber numbers and relatively low Ohnesorge numbers. This regime corresponds to the capillary wave breakup mechanism, where ultrasonic vibration induces surface instabilities that lead to controlled droplet detachment. Experimental studies using the B-90 system have reported droplet diameters ranging from approximately 8 to 21 µm, producing dried particles in the submicron to micron range. Maintaining similar Weber and Ohnesorge numbers during process scale-up ensures dynamic similarity in atomization behaviour, enabling consistent particle size distribution across different spray drying scales [38].

The schematic diagram illustrates the fundamental scaling framework governing droplet and particle formation in spray drying systems employing a piezoelectric vibrating mesh atomizer (see Figure 3.a). In such systems, droplet generation is primarily controlled by the interplay between ultrasonic vibration frequency, mesh aperture size, and the fluid dynamic regime characterized by the Weber and Ohnesorge numbers. The atomization process begins with the oscillation of the piezoelectric actuator, which generates high-frequency mechanical vibrations. These vibrations are transmitted to the liquid layer above the vibrating mesh, inducing capillary waves on the liquid surface. When the amplitude of these waves exceeds a critical instability threshold, droplets are ejected through the micro-scale mesh apertures. Consequently, the vibration frequency plays a crucial role in determining the wavelength of the capillary waves and ultimately the droplet diameter. Higher frequencies generally produce shorter wavelength disturbances, resulting in smaller droplets. In addition to the vibration frequency, the geometry of the vibrating mesh strongly influences droplet formation. The mesh aperture size acts as a geometric constraint that limits the droplet size during the atomization process. Smaller mesh openings typically generate finer droplets due to the restricted liquid flow through the micro-orifices. Therefore, the combination of ultrasonic frequency and mesh aperture size provides an effective mechanism for controlling droplet size distribution in ultrasonic spray drying systems[37], [61], [62].

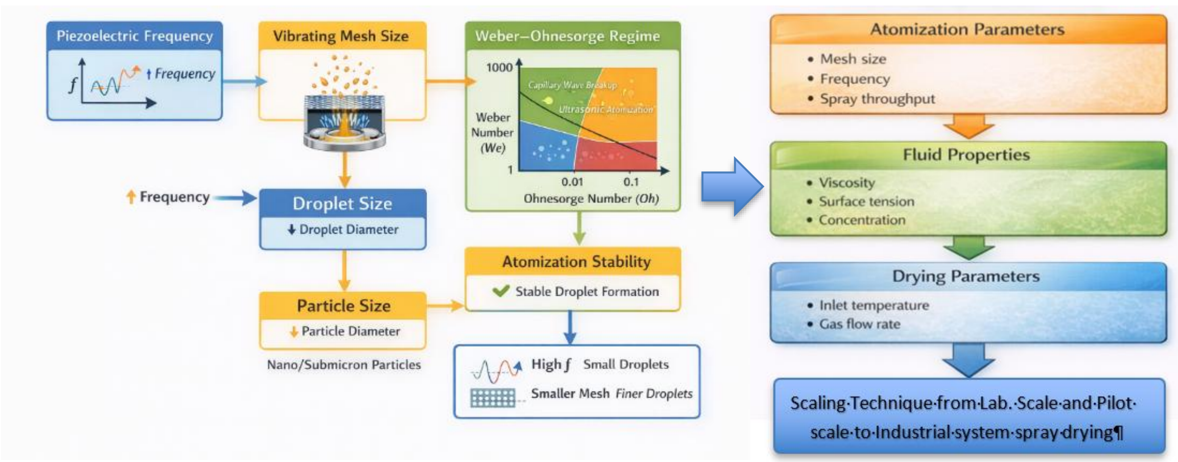

(a) (b)

Figure 3 (a) Fundamental scaling framework governing particle formation in spray drying systems (b) Parameter influence hierarchy for ultrasonic spray drying system

The parameter hierarchy illustrated in Figure 3.b highlights the relative importance of different groups of variables influencing the performance of ultrasonic spray drying systems. The parameter hierarchy presented in Figure 3(b) was developed through qualitative comparative analysis of trends repeatedly reported across the reviewed experimental studies. These parameters were ranked according to the consistency and magnitude of their reported influence on droplet formation, particle size distribution, and atomization stability. Atomization parameters were classified as having the highest influence because they directly govern droplet generation mechanisms. Fluid properties were categorized as secondary parameters due to their indirect influence through modification of viscous and capillary effects. Drying parameters were considered tertiary because their primary role is associated with solvent evaporation and particle morphology rather than initial droplet formation. Although the hierarchy is conceptual and literature-based rather than statistically weighted, it provides a systematic interpretation of the dominant scaling mechanisms governing ultrasonic spray drying systems.

The diagram categorizes the governing parameters into three main levels: atomization parameters, fluid properties, and drying parameters. This hierarchical structure reflects the fundamental mechanism of spray drying, in which droplet generation precedes solvent evaporation and particle formation. Consequently, parameters that control droplet formation tend to exert the strongest influence on the final powder characteristics. At the highest level of influence are the atomization parameters, which include mesh aperture size, vibration frequency, and spray throughput. These parameters directly control the droplet generation mechanism in vibrating mesh atomizers. Several studies have demonstrated that the geometry of the atomizer plays a dominant role in determining droplet size. For instance, experimental investigations by Li et al. (2010) and Arpagaus et al. (2017) showed that smaller mesh apertures in vibrating mesh atomizers produce smaller droplets and consequently smaller particles during spray drying[38], [63] . This relationship occurs because the mesh opening limits the size of the liquid ligaments ejected during atomization. Similarly, ultrasonic vibration frequency influences the wavelength of capillary waves formed on the liquid surface. According to Lang's capillary wave theory, droplet diameter is inversely related to ultrasonic frequency, meaning that higher frequencies generally lead to smaller droplets [51]. Therefore, atomization parameters represent the primary scaling variables when designing spray drying systems using ultrasonic atomizers. The second level in the hierarchy consists of fluid properties, including viscosity, surface tension, and feed concentration. These parameters influence droplet formation indirectly by altering the balance between inertial, viscous, and surface tension forces within the liquid. Several researchers have reported that fluid rheology significantly affects atomization stability. For example, Gómez-Mascaraque et al. (2020) and Wang et al. (2022) observed that higher viscosity tends to increase droplet size because viscous forces dampen the capillary wave instabilities responsible for droplet detachment [64], [65]. Similarly, surface tension influences the energy required for droplet breakup, while feed concentration affects the shrinkage behaviour of droplets during drying. These relationships are commonly described using dimensionless parameters such as the Weber number and Ohnesorge number, which characterize the balance of forces governing atomization processes. At the lowest level of influence are the drying parameters, which include inlet air temperature and drying gas flow rate. Although these parameters are essential for controlling evaporation kinetics and final moisture content, their influence on droplet formation is generally limited. Several studies using nano spray dryers have demonstrated that variations in inlet temperature primarily affect drying rate rather than droplet size distribution. For example, research conducted by Bürki et al. (2011) and Baldelli et al. (2022) reported that inlet temperature had minimal impact on particle size but significantly affected residual moisture and product yield. Gas flow rate also plays an important role in determining particle residence time within the drying chamber, which can influence particle morphology and agglomeration behaviour.[43, 50]

The stability of droplet formation can be interpreted using the Weber–Ohnesorge regime map, which describes the balance between inertial, viscous, and surface tension forces during atomization (see Figure 2). For ultrasonic atomization systems, stable droplet generation typically occurs within a regime characterized by moderate Weber numbers and relatively low Ohnesorge numbers. In this region, capillary wave instabilities dominate the droplet formation mechanism, enabling controlled droplet detachment from the vibrating mesh surface. This scaling framework is particularly relevant to experimental studies conducted using the Büchi Nano Spray Dryer B-90, which employs a piezoelectric vibrating mesh atomizer operating at ultrasonic frequencies of approximately 100 kHz. Experimental investigations have reported droplet diameters typically ranging from 8 to 21 µm, producing dried particles in the submicron to micron range (approximately 300 nm to 5 µm). These particle sizes are primarily governed by the initial droplet diameter and the solid fraction of the feed solution during solvent evaporation. From a process scaling perspective, maintaining similar Weber and Ohnesorge numbers across different operating scales ensures dynamic similarity in the atomization process. This implies that particle formation in spray drying systems scaling up spray drying systems, parameters such as feed viscosity, surface tension, droplet diameter, and characteristic velocity must be adjusted to preserve the same dimensionless regime. By maintaining this similarity, the droplet formation mechanism and resulting particle size distribution can remain consistent across laboratory-scale and pilot-scale spray drying systems.[38], [39]

4.2 Scaling Implications

The scaling of ultrasonic spray drying systems assisted by vibrating mesh atomizers requires a fundamentally different approach compared with conventional pressure-nozzle or rotary-atomizer spray dryers [36]. In conventional spray drying systems, scale-up is generally performed by preserving thermal residence time, drying kinetics, and air-flow distribution within the drying chamber. However, in ultrasonic spray drying systems, the atomization mechanism itself becomes the dominant factor governing particle formation because droplet generation is controlled by capillary-wave instabilities induced by ultrasonic vibration [59]. Consequently, maintaining atomization similarity during scale-up is essential to preserve droplet formation behavior and final particle characteristics.[24]

The present parametric analysis indicates that atomization parameters, particularly mesh aperture size and ultrasonic vibration frequency, represent the primary scaling variables in vibrating mesh atomizer-assisted spray drying systems. These parameters directly determine the wavelength of capillary waves formed at the liquid–mesh interface and therefore control the initial droplet diameter generated during atomization. Since the final particle size distribution strongly depends on the initial droplet size, preserving similar atomization conditions across different process scales becomes critical for maintaining consistent powder characteristics. Unlike conventional spray dryers, where droplet size can often be adjusted through pressure variation, vibrating mesh atomizers are constrained by the geometric characteristics of the mesh and the operating ultrasonic frequency.

Dimensionless analysis further demonstrates that dynamic similarity during scale-up can be achieved by maintaining appropriate Weber number and Ohnesorge number regimes. The Weber number represents the balance between inertial and surface tension forces, whereas the Ohnesorge number characterizes the relative influence of viscous damping during capillary-wave formation. Experimental studies reviewed in this work suggest that stable ultrasonic atomization typically occurs within moderate Weber numbers and relatively low Ohnesorge numbers, corresponding to capillary-wave-driven droplet breakup mechanisms. Therefore, industrial-scale ultrasonic spray drying systems should be designed such that fluid properties, characteristic velocity, and atomization geometry preserve similar Weber–Ohnesorge operating regimes observed in laboratory-scale systems such as the Büchi Nano Spray Dryer B-90.

The scaling implications also indicate that increasing production throughput in ultrasonic spray drying systems cannot rely solely on enlarging atomizer dimensions, as commonly performed in conventional spray dryers. Excessive increase in liquid throughput may destabilize the thin liquid film above the vibrating mesh, reduce acoustic energy transmission efficiency, and alter the capillary-wave breakup mechanism. Consequently, industrial scale-up may require parallelization strategies using multiple vibrating mesh atomizers operating simultaneously rather than simple geometric enlargement of a single atomizer unit. Such modular scaling approaches could maintain atomization stability while increasing production capacity.

Fluid properties also become increasingly important during process scale-up because viscosity and surface tension strongly influence the atomization regime. Feed formulations with higher viscosity may suppress capillary-wave growth due to increased viscous damping, leading to unstable droplet formation or broader droplet size distributions. Therefore, maintaining similar rheological properties between laboratory-scale and industrial-scale feed systems is essential for preserving atomization behavior. In addition, drying conditions such as inlet temperature and gas flow rate must be adjusted to accommodate increased solvent evaporation demands at larger process scales while avoiding thermal degradation or particle agglomeration.

Overall, the proposed scaling framework suggests that successful scale-up of ultrasonic spray drying systems should prioritize atomization similarity rather than purely geometric similarity. Maintaining consistent relationships among ultrasonic frequency, mesh geometry, fluid properties, and dimensionless force balances provides a more reliable basis for preserving droplet generation behavior and achieving controlled particle formation across different operating scales. Consequently, the present framework offers a conceptual guideline for the future development of industrial ultrasonic spray drying technologies capable of producing highly engineered submicron and micron-scale powders with improved process controllability.

4.3 Limitations of the Conceptual Scaling Framework

Although the proposed conceptual scaling framework provides useful theoretical insight into the dominant mechanisms governing ultrasonic spray drying systems, several limitations should be acknowledged. First, the framework is primarily derived from literature synthesis rather than direct experimental validation under controlled scaling conditions. As a result, the proposed parameter hierarchy should be interpreted as a conceptual guideline rather than an absolute predictive model. Second, the reviewed studies employed different feed formulations, experimental configurations, and measurement techniques, which may introduce variability in the reported atomization behavior and particle characteristics. Third, the present framework focuses mainly on droplet generation mechanisms associated with vibrating mesh atomizers and does not fully account for industrial-scale complexities such as turbulent airflow interaction, multi-droplet collision phenomena, or large-scale thermal non-uniformity. Therefore, future work should focus on systematic experimental validation and computational modeling to quantitatively verify the proposed Weber–Ohnesorge scaling framework across different operating scales.

5. CONCLUSION

This study presents a comprehensive review and conceptual parametric hierarchy for ultrasonic spray drying systems assisted by piezoelectric vibrating mesh atomizers. Unlike previous studies that primarily focused on isolated process variables or formulation-specific applications, the present work systematically integrates atomization parameters, fluid properties, and drying conditions into a unified scaling-oriented framework. The analysis demonstrates that atomization parameters, particularly mesh aperture size, ultrasonic vibration frequency, and spray throughput, constitute the dominant variables governing droplet generation and particle size distribution through capillary-wave-driven breakup mechanisms.

Fluid properties such as viscosity, surface tension, and feed concentration were identified as secondary scaling parameters because they influence the atomization regime through the Weber and Ohnesorge dimensionless numbers. In contrast, drying parameters primarily affect evaporation kinetics and particle morphology rather than the initial droplet generation process. The proposed Weber–Ohnesorge scaling framework therefore provides a theoretical basis for maintaining atomization similarity during process scale-up from laboratory-scale to industrial-scale ultrasonic spray drying systems.

The novelty of this study lies in the development of a conceptual parameter hierarchy combined with a dimensionless scaling framework specifically for ultrasonic vibrating mesh atomizer-assisted spray drying systems. This contribution advances the understanding of ultrasonic spray drying engineering and provides a systematic foundation for the future development of industrial-scale spray drying technologies capable of producing highly controlled submicron and micron-scale particles.

6. ACKNOWLEDGEMENT

This research study was supported by The Ministry of Education, Culture, Research and Technology of Indonesia. under Grant No. 162/SPK/D.D4/PPK.01.APTV/VI/2023. The authors also thank the supervisors in Doctoral Program of Engineering, Faculty of Engineering, Udayana University for their valuable assistance and insightful discussions throughout this study.

7. REFERENCES

[1] E. H. J. Kim, X. D. Chen, and D. Pearce, “Surface composition of industrial spray-dried milk powders. 2. Effects of spray drying conditions on the surface composition,” *J. Food Eng.*, vol. 94, no. 2, pp. 169–181, Sep. 2009, doi: 10.1016/j.jfoodeng.2008.10.020.

[2] M. Abdul, M. Imran, F. Atta, and F. Al-asmari, “Industrial Crops & Products Characterization and effect of optimized spray-drying conditions on spray-dried coriander essential oil,” vol. 209, no. October 2023, 2024, doi: 10.1016/j.indcrop.2023.117976.

[3] A. Farshchi, A. Hassanpour, and A. E. Bayly, “The structure of spray-dried detergent powders,” *Powder Technol.*, vol. 355, pp. 738–754, Oct. 2019, doi: 10.1016/j.powtec.2019.06.049.

[4] M. Ordoubadi, H. Wang, and R. Vehring, “Mechanistic Formulation Design of Spray-Dried Powders†,” *KONA Powder and Particle Journal*, vol. 40, pp. 149–171, 2023, doi: 10.14356/KONA.2023012.

[5] S. H. Moon, K. H. Chang, H. M. Park, B. J. Park, S. K. Yoo, and K. C. Nam, “Effects of driving frequency and voltage on the performances of vibrating mesh nebulizers,” *Applied Sciences (Switzerland)*, vol. 11, no. 3, pp. 1–11, 2021, doi: 10.3390/app11031296.

[6] J. N. Pritchard, R. H. M. Hatley, J. Denyer, and Di. Von Hollen, “Mesh nebulizers have become the first choice for new nebulized pharmaceutical drug developments,” *Ther. Deliv.*, vol. 9, no. 2, pp. 121–136, 2018, doi: 10.4155/tde-2017-0102.

[7] P. Fossat, M. Ichchou, and O. Bareille, “Analytical model of the dynamic behavior of a vibrating mesh nebulizer for optimal atomization efficiency,” *Sens. Actuators A Phys.*, vol. 343, 2022, doi: 10.1016/j.sna.2022.113646.

[8] J. L. Liang, F. Zhang, J. H. Zhang, W. Q. Huang, Y. X. Wen, and B. C. Chen, “Improvement of Mesh Atomizer Performance by Electrolytic Polishing,” *Applied Sciences (Switzerland)*, vol. 13, no. 4, 2023, doi: 10.3390/app13042572.

[9] P. Sharma, M. Quazi, I. R. Vazquez, and N. Jackson, “Investigation of droplet size distribution for vibrating mesh atomizers,” *J. Aerosol Sci.*, vol. 166, pp. 1–25, 2022, doi: 10.1016/j.jaerosci.2022.106072.

[10] I. Agus Tri Putra, W. N. Septiadi, D. N. K. P. Negara, and T. G. T. Nindhia, “Performance Investigation of Water Purification System Assisted by Ultrasonic Vibrating Mesh Atomizer,” *J. Phys. Conf. Ser.*, vol. 2972, no. 1, p. 012034, Mar. 2025, doi: 10.1088/1742-6596/2972/1/012034.

[11] I. D. Gede, A. Tri, W. N. Septiadi, D. Ngakan, and K. Putra, *Comparative Study of Ultrasonic Waveform to Enhanced The Atomization Rate of Dynamic Mesh Atomizer*, vol. 2024. Atlantis Press International BV, 2024. doi: 10.2991/978-94-6463-587-4.
[12] Q. Yan, W. Sun, and J. Zhang, "Study on the influencing factors of the atomization rate in a piezoceramic vibrating mesh atomizer," *Applied Sciences (Switzerland)*, vol. 10, no. 7, 2020, doi: 10.3390/app10072422.
[13] R. Vehring, W. R. Foss, and D. Lechuga-Ballesteros, "Particle formation in spray drying," *J. Aerosol Sci.*, vol. 38, no. 7, pp. 728–746, Jul. 2007, doi: 10.1016/J.JAEROSCI.2007.04.005.
[14] S. Chopde, R. Datir, G. Deshmukh, A. Dhotre, and M. Patil, "Nanoparticle formation by nanospray drying & its application in nanoencapsulation of food bioactive ingredients," *J. Agric. Food Res.*, vol. 2, no. 3, p. 100085, Dec. 2020, doi: 10.1016/j.jafr.2020.100085.
[15] C. Draheim, F. De Crécy, S. Hansen, E. M. Collnot, and C. M. Lehr, "A design of experiment study of nanoprecipitation and nano spray drying as processes to prepare plga nano-and microparticles with defined sizes and size distributions," *Pharm. Res.*, vol. 32, no. 8, pp. 2609–2624, 2015, doi: 10.1007/s11095-015-1647-9.
[16] T. W. Wong and P. John, "Advances in spray drying technology for nanoparticle formation," in *Handbook of Nanoparticles*, Springer International Publishing, 2015, pp. 329–346. doi: 10.1007/978-3-319-15338-4_18.
[17] B. Gu, B. Linehan, and Y. C. Tseng, "Optimization of the Büchi B-90 spray drying process using central composite design for preparation of solid dispersions," *Int. J. Pharm.*, vol. 491, no. 1–2, pp. 208–217, Aug. 2015, doi: 10.1016/J.IJPHARM.2015.06.006.
[18] A. Kyriakoudi and M. Z. Tsimidou, "Properties of encapsulated saffron extracts in maltodextrin using the Büchi B-90 nano spray-dryer," *Food Chem.*, vol. 266, pp. 458–465, Nov. 2018, doi: 10.1016/J.FOODCHEM.2018.06.038.
[19] D. Yonata, Y. N. S. Ulvie, E. Soesanto, E. Sulistyowati, B. Pranata, and A. Rosidi, "Stabilization and Controlled Release of Curcumin from Temulawak by Spray-Drying Microencapsulation with Composite Wall Materials," *Trends in Sciences*, vol. 22, no. 2, Feb. 2025, doi: 10.48048/tis.2025.9125.
[20] I. C. Jacobs, "Atomization and Spray-Drying Processes," pp. 47–56, 2014.
[21] D. E. Walton and C. J. Mumford, "The Morphology of Spray-Dried Particles: The Effect of Process Variables upon the Morphology of Spray-Dried Particles," *Chemical Engineering Research and Design*, vol. 77, no. 5, pp. 442–460, Jul. 1999, doi: 10.1205/026387699526296.
[22] C. I. Piñón-Balderrama, C. Leyva-Porras, Y. Terán-Figueroa, V. Espinosa-Solís, C. Álvarez-Salas, and M. Z. Saavedra-Leos, "Encapsulation of active ingredients in food industry by spray-drying and nano spray-drying technologies," *Processes*, vol. 8, no. 8, 2020, doi: 10.3390/PR8080889.
[23] N. A. Pambudi, J. Yusafiadi, M. K. Biddinika, Y. Estriyanto, and A. Sarifudin, "An experimental investigation of salt production improvement by spraying and heating," *Case Studies in Thermal Engineering*, vol. 30, no. December 2021, p. 101739, 2022, doi: 10.1016/j.csite.2021.101739.
[24] M. Selvamuthukumaran, C. Tranchant, and J. Shi, *Spraying drying: Concept, application and its recent advances in food processing*. 2019. doi: 10.1201/9780429055133-1.
[25] M. Munoz-Ibanez, C. Azagoh, B. N. Dubey, E. Dumoulin, and C. Turchiuli, "Changes in oil-in-water emulsion size distribution during the atomization step in spray-drying encapsulation," *J. Food Eng.*, vol. 167, pp. 122–132, 2015, doi: 10.1016/j.jfoodeng.2015.02.008.
[26] A. B. D. Nandiyanto and K. Okuyama, "Progress in developing spray-drying methods for the production of controlled morphology particles: From the nanometer to submicrometer size ranges," *Advanced Powder Technology*, vol. 22, no. 1, pp. 1–19, 2011, doi: 10.1016/j.apt.2010.09.011.
[27] R. Deshmukh, P. Wagh, and J. Naik, "Solvent evaporation and spray drying technique for micro- and nanospheres/particles preparation: A review," Nov. 17, 2016, *Taylor and Francis Inc.* doi: 10.1080/07373937.2016.1232271.
[28] K. Samborska *et al.*, "Innovations in spray drying process for food and pharma industries," *J. Food Eng.*, vol. 321, May 2022, doi: 10.1016/J.JFOODENG.2022.110960.
[29] D. L. Yang, R. K. Liu, Y. Wei, Q. Sun, and J. X. Wang, "Micro-sized nanoaggregates: Spray-drying-assisted fabrication and applications," *Particuology*, vol. 85, pp. 22–48, 2024, doi: 10.1016/j.partic.2023.03.013.
[30] D. A. Miller, D. Ellenberger, T. Porfirio, and M. Gil, "Spray-Drying Technology," in *Formulating Poorly Water Soluble Drugs*, R. O. Williams III, D. A. Davis Jr., and D. A. Miller, Eds., Cham: Springer International Publishing, 2022, pp. 377–452. doi: 10.1007/978-3-030-88719-3_10.

[31] K. B. Shepard, A. M. Dower, A. M. Ekdahl, M. M. Morgen, J. M. Baumann, and D. T. Vodak, "Solvent-Assisted Secondary Drying of Spray-Dried Polymers," *Pharm. Res.*, vol. 37, no. 8, p. 156, 2020, doi: 10.1007/s11095-020-02890-0.
[32] M. N. PATIL, A. B. PANDIT, and B. N. THORAT, "Ultrasonic Atomisation Assisted Spray Drying," pp. 255–261, 2007, doi: 10.1142/9789812771957_0036.
[33] B. Robert and E. B. Brown, *Handbook on Spray Drying Applications for Food Industries*, no. 1. 2004.
[34] J. Jung, M. Kim, and J. Kim, "Filtration of dispersed nanoparticles using cyclone and ultrasonic atomization," *Journal of the Acoustical Society of Korea*, vol. 41, no. 1, pp. 9–15, 2022, doi: 10.7776/ASK.2022.41.1.009.
[35] S. Poozesh, S. M. Jafari, and N. K. Akafuah, "Interrogation of a new inline multi-bin cyclone for sorting of produced powders of a lab-scale spray dryer," *Powder Technol.*, vol. 373, pp. 590–598, 2020, doi: 10.1016/j.powtec.2020.07.012.
[36] L. X. Huang, K. Kumar, and A. S. Mujumdar, "A comparative study of a spray dryer with rotary disc atomizer and pressure nozzle using computational fluid dynamic simulations," *Chemical Engineering and Processing: Process Intensification*, vol. 45, no. 6, pp. 461–470, Jun. 2006, doi: 10.1016/J.CEP.2005.11.004.
[37] Y. Zhang and S. Yuan, "Phase, pressure and velocity evolution and atomization characteristics of multiple Faraday waves in ultrasonic atomization: experiments and simulations," *International Journal of Multiphase Flow*, vol. 156, no. 37, pp. 1–29, 2022, doi: 10.1016/j.ijmultiphaseflow.2022.104223.
[38] X. Li, N. Anton, C. Arpagaus, F. Belleteix, and T. F. Vandamme, "Nanoparticles by spray drying using innovative new technology: The Büchi Nano Spray Dryer B-90," *Journal of Controlled Release*, vol. 147, no. 2, pp. 304–310, Oct. 2010, doi: 10.1016/j.jconrel.2010.07.113.
[39] S. N. Harsha *et al.*, "Nanoparticle formulation by Büchi B-90 Nano Spray Dryer for oral mucoadhesion," *Drug Des. Devel. Ther.*, vol. 9, no. null, pp. 273–282, Jan. 2015, doi: 10.2147/DDDT.S66654.
[40] R. Strob *et al.*, "Preparation and characterization of spray-dried submicron particles for pharmaceutical application," *Advanced Powder Technology*, vol. 29, no. 12, pp. 2920–2927, Dec. 2018, doi: 10.1016/j.apt.2018.09.016.
[41] K. Almansour *et al.*, "Particle Engineering by Nano Spray Drying: Optimization of Process Parameters with Hydroethanolic versus Aqueous Solutions," *Pharmaceutics*, vol. 14, no. 4, pp. 1–20, 2022, doi: 10.3390/pharmaceutics14040800.
[42] S. Hwang, Y. Han, and D. J. Gardner, "Characterization of CNC Nanoparticles Prepared via Ultrasonic-Assisted Spray Drying and Their Application in Composite Films," *Nanomaterials*, vol. 13, no. 22, 2023, doi: 10.3390/nano13222928.
[43] K. Bürki, I. Jeon, C. Arpagaus, and G. Betz, "New insights into respirable protein powder preparation using a nano spray dryer," *Int. J. Pharm.*, vol. 408, no. 1–2, pp. 248–256, Apr. 2011, doi: 10.1016/j.ijpharm.2011.02.012.
[44] S. H. Lee, D. Heng, W. K. Ng, H. K. Chan, and R. B. H. Tan, "Nano spray drying: A novel method for preparing protein nanoparticles for protein therapy," *Int. J. Pharm.*, vol. 403, no. 1–2, pp. 192–200, Jan. 2011, doi: 10.1016/j.ijpharm.2010.10.012.
[45] K. Schmid, C. Arpagaus, and W. Friess, "Evaluation of the Nano Spray Dryer B-90 for pharmaceutical applications," *Pharm. Dev. Technol.*, vol. 16, no. 4, pp. 287–294, Aug. 2011, doi: 10.3109/10837450.2010.485320.
[46] B. Gu, B. Linehan, and Y. C. Tseng, "Optimization of the Büchi B-90 spray drying process using central composite design for preparation of solid dispersions," *Int. J. Pharm.*, vol. 491, no. 1–2, pp. 208–217, Aug. 2015, doi: 10.1016/j.ijpharm.2015.06.006.
[47] C. Arpagaus, A. Collenberg, D. Rütti, E. Assadpour, and S. M. Jafari, "Nano spray drying for encapsulation of pharmaceuticals," *Int. J. Pharm.*, vol. 546, no. 1–2, pp. 194–214, Jul. 2018, doi: 10.1016/j.ijpharm.2018.05.037.
[48] T. M. Shehata and M. M. Ibrahima, "BÜCHI nano spray dryer B-90: a promising technology for the production of metformin hydrochloride-loaded alginate–gelatin nanoparticles," *Drug Dev. Ind. Pharm.*, vol. 45, no. 12, pp. 1907–1914, Dec. 2019, doi: 10.1080/03639045.2019.1680992.
[49] L. G. Gómez-Mascaraque and A. Lopez-Rubio, "Production of food bioactive-loaded nanoparticles by electrospraying," *Nanoencapsulation of Food Ingredients by Specialized Equipment: Volume 3 in the Nanoencapsulation in the Food Industry series*, pp. 107–149, Jan. 2019, doi: 10.1016/B978-0-12-815671-1.00003-2.

[50] A. Baldelli, H. Oguzlu, D. Y. Liang, A. Subiantoro, M. W. Woo, and A. Pratap-Singh, "Spray freeze drying of dairy products: Effect of formulation on dispersibility," *J. Food Eng.*, vol. 335, p. 111191, Dec. 2022, doi: 10.1016/J.JFOODENG.2022.111191.
[51] R. Lang, "Ultrasonic Atomization of Liquids," *Acustica*, vol. 341, no. 1954, pp. 28–30, 1962.
[52] K. A. Ramisetty, A. B. Pandit, and P. R. Gogate, "Investigations into ultrasound induced atomization," *Ultrason. Sonochem.*, vol. 20, no. 1, pp. 254–264, Jan. 2013, doi: 10.1016/J.ULTSONCH.2012.05.001.
[53] O. Z. Olszewski, R. Macloughlin, A. Blake, M. O'Neill, A. Mathewson, and N. Jackson, "A Silicon-based MEMS Vibrating Mesh Nebulizer for Inhaled Drug Delivery," *Procedia Eng.*, vol. 168, pp. 1521–1524, 2016, doi: 10.1016/j.proeng.2016.11.451.
[54] F. Zhang *et al.*, "Error Correction and Reanalysis of the Vibration Analysis of a Piezoelectric Ultrasonic Atomizer to Control Atomization Rate," *Applied Sciences (Switzerland)*, vol. 13, no. 10, 2023, doi: 10.3390/app13106293.
[55] Q. Yan, C. Wu, and J. Zhang, "Effect of the dynamic cone angle on the atomization performance of a piezoceramic vibrating mesh atomizer," *Applied Sciences (Switzerland)*, vol. 9, no. 9, 2019, doi: 10.3390/app9091836.
[56] Y. Da Lang and J. H. Zhang, "Influence of piezoelectric atomizer pores on ultrasonic atomization effect," *Proceedings of the 2014 Symposium on Piezoelectricity, Acoustic Waves and Device Applications, SPAWDA 2014*, pp. 287–290, 2014, doi: 10.1109/SPAWDA.2014.6998582.
[57] I. C. Kemp, T. Hartwig, R. Herdman, P. Hamilton, A. Bisten, and S. Bermingham, "Spray drying with a two-fluid nozzle to produce fine particles: Atomization, scale-up, and modeling," *Drying Technology*, vol. 34, no. 10, pp. 1243–1252, 2016, doi: 10.1080/07373937.2015.1103748.
[58] J. P. Szczap and I. C. Jacobs, "Atomization and spray drying processes," *Microencapsulation in the Food Industry: A Practical Implementation Guide*, pp. 59–71, Jan. 2023, doi: 10.1016/B978-0-12-821683-5.00017-0.
[59] K. Söllner, "The mechanism of the formation of fogs by ultrasonic waves," *Trans. Faraday Soc.*, vol. 32, no. 0, pp. 1532–1536, 1936, doi: 10.1039/TF9363201532.
[60] H. Zhang, X. Zhang, X. Yi, F. He, F. Niu, and P. Hao, "Dynamic behaviors of droplets impacting on ultrasonically vibrating surfaces," *Exp. Therm. Fluid Sci.*, vol. 112, p. 110019, 2020, doi: 10.1016/j.expthermflusci.2019.110019.
[61] F. Liu, N. Kang, Y. Li, and Q. Wu, "Experimental investigation on the atomization of a spherical droplet induced by Faraday instability," *Exp. Therm. Fluid Sci.*, vol. 100, no. February 2018, pp. 311–318, 2019, doi: 10.1016/j.expthermflusci.2018.09.016.
[62] C. S. Tsai *et al.*, "Ultrasound-driven megahertz Faraday waves for generation of monodisperse micro droplets and applications," *Phys. Procedia*, vol. 70, pp. 872–875, 2015, doi: 10.1016/j.phpro.2015.08.179.
[63] S. M. Jafari, C. Arpagaus, M. A. Cerqueira, and K. Samborska, "Nano spray drying of food ingredients; materials, processing and applications," *Trends Food Sci. Technol.*, vol. 109, no. January, pp. 632–646, 2021, doi: 10.1016/j.tifs.2021.01.061.
[64] L. G. Gómez-Mascaraque, B. Miralles, I. Recio, and A. López-Rubio, "Microencapsulation of a whey protein hydrolysate within micro-hydrogels: Impact on gastrointestinal stability and potential for functional yoghurt development," *J. Funct. Foods*, vol. 26, pp. 290–300, 2016, doi: https://doi.org/10.1016/j.jff.2016.08.006.
[65] X. Wang, Y. Mori, and K. Tsuchiya, "Periodicity in ultrasonic atomization involving beads-fountain oscillations and mist generation: Effects of driving frequency," *Ultrason. Sonochem.*, vol. 86, no. March, p. 105997, 2022, doi: 10.1016/j.ultsonch.2022.105997.

(JOURNAL ENGINEERING DESIGN AND TECHNOLOGY)
Journal Engineering Design and Technology
Vol. 26 No.2 July 2026 ; p. 148 - 156
Journal Homepage : http://ojs2.pnb.ac.id/index.php/LOGIC
p-ISSN : 1412-114X e-ISSN : 2580-5649

Performance Evaluation of Banana Fiber as a Natural Adsorbent for Methane Enhancement in Biogas Using GC–MS Analysis

I Wayan Sutama [1)*], I Nyoman Suprapta Winaya [2)], Ida Bagus Alit Swarmardika [3)], Rukmi Sari Hartati [4)], I Made Panji Tirta Prakasa [4)]

1) Program Of Doctor Engineering Science Universitas Udayana, Indonesia
2) Mechanical Engineering Study Program Universitas Udayana, Indonesia
3) Electrical Engineering Study Program Universitas Udayana, Indonesia
4) Electrical Engineering Study Program Universitas Pendidikan Nasional, Indonesia

Corresponding email 1)* :
wayansutama@undiknas.ac.id

Abstract. Biogas utilization from agricultural waste in Indonesia remains underdeveloped despite its significant potential as a renewable energy source. Biogas produced through anaerobic digestion contains a high concentration of carbon dioxide (CO_2), which lowers its calorific value and limits its direct use as a clean fuel. Therefore, biogas upgrading is necessary to increase methane (CH_4) concentration and improve fuel quality. This study evaluates the performance of banana fiber as a natural adsorbent for methane enhancement and carbon dioxide removal in biogas. Banana fiber was selected because of its lignocellulosic composition and porous structure, which provide potential adsorption sites for gas molecules. The experimental setup employed a fixed-bed filtration system in which raw biogas from an anaerobic digester was passed through a column packed with untreated banana fiber. Gas samples were collected before and after filtration and analyzed using Gas Chromatography–Mass Spectrometry (GC–MS) to determine changes in CH_4 and CO_2 concentrations. The results showed that methane concentration increased from 51.37% to 60.84%, corresponding to an enhancement of 9.47%, while carbon dioxide concentration decreased from 48.63% to 39.15%, representing a reduction of 9.48%. These findings indicate that banana fiber effectively improves biogas quality by selectively adsorbing CO_2 and enriching methane content. The adsorption performance is attributed to the presence of hydroxyl (–OH) and carboxyl (–COOH) functional groups in the lignocellulosic structure of banana fiber, which facilitate physical adsorption and enhance gas–solid interactions. In addition, the porous structure of the fiber increases surface area and supports adsorption efficiency. This study demonstrates the effectiveness of untreated banana fiber as a low-cost and environmentally friendly adsorbent for biogas upgrading using GC–MS analysis. The findings highlight its potential application in small-scale and decentralized renewable energy systems, particularly in rural and agricultural areas. Furthermore, the study provides important implications for laboratory-scale biogas purification systems and future industrial biogas upgrading applications.

Keywords : Biogas, Banana Fiber, Methane Enhancement, CO_2 Removal, Natural Adsorbent

1. INTRODUCTION

The increasing global demand for sustainable and environmentally friendly energy sources has become a critical issue due to climate change, environmental degradation, and the depletion of fossil fuel reserves. The continued dependence on fossil fuels has significantly contributed to greenhouse gas emissions, which are the main drivers of global warming and environmental instability. Therefore, the development of renewable energy technologies has become an essential strategy to achieve energy sustainability and reduce environmental impact [1], [18]. Among various renewable energy sources, biogas has emerged as a promising alternative due to its ability to convert organic waste into usable energy. Biogas is produced through the anaerobic digestion of organic materials such as agricultural residues, livestock manure, and food waste. Anaerobic digestion has been widely studied for organic waste treatment [14]. This process not only generates energy but also contributes to waste management and environmental protection, making it an important component in circular economy systems [17], [18].

However, raw biogas contains a significant amount of carbon dioxide (CO_2), which reduces its calorific value and limits its direct application as a clean fuel. The presence of CO_2 leads to lower combustion efficiency, unstable flame characteristics, and reduced energy output. Therefore, biogas upgrading is required to increase methane (CH_4) concentration and improve overall fuel quality [2], [3]. Various technologies have been developed for biogas upgrading, including water scrubbing, chemical absorption, membrane separation, and pressure swing adsorption. Although these methods are effective, they generally require high capital investment, complex operational systems, and considerable energy consumption [4]. These limitations make conventional upgrading technologies less suitable for small-scale and decentralized applications, particularly in rural areas.

To address these challenges, recent studies have focused on the use of low-cost and environmentally friendly adsorbents derived from biomass. Natural fibers have gained considerable attention due to their abundance, biodegradability, and renewable characteristics. Lignocellulosic materials such as rice husk, coconut fiber, and agricultural residues have demonstrated potential for gas adsorption due to their porous structure and the presence of functional groups that facilitate gas interaction [5], [6]. Banana fiber is one of the most abundant agricultural wastes in tropical regions and is often underutilized. It consists primarily of cellulose, hemicellulose, and lignin, which provide a fibrous and porous structure suitable for adsorption processes. The presence of polar functional groups such as hydroxyl (–OH) and carboxyl (–COOH) enables banana fiber to interact with gas molecules, particularly carbon dioxide, through physical adsorption mechanisms such as hydrogen bonding and van der Waals interactions [6]. From a sustainability perspective, the utilization of banana fiber aligns with the concept of circular economy, where agricultural waste is transformed into value-added materials for energy applications. This approach not only reduces environmental pollution but also enhances resource efficiency and supports sustainable energy production, especially in developing regions. Previous studies have shown that natural fibers can improve biogas quality by reducing carbon dioxide and increasing methane concentration.

Previous studies have also confirmed that lignocellulosic materials contain active functional groups that contribute significantly to adsorption processes [5], [7]. However, the adsorption performance of natural fibers varies depending on their chemical composition, surface characteristics, and structural properties. Despite the growing interest in biomass-based adsorbents, studies specifically investigating untreated banana fiber as a direct adsorbent for biogas upgrading remain very limited. Most previous studies have focused on activated carbon, chemically modified biomass, or synthetic adsorbent materials [18], [19], which often require additional chemical treatment, higher production costs, and more complex preparation processes. In contrast, untreated banana fiber offers advantages in terms of availability, low cost, biodegradability, and environmental sustainability, making it highly suitable for decentralized and small-scale renewable energy systems. In addition, previous studies have generally concentrated only on changes in biogas composition without providing detailed analysis of the adsorption mechanism occurring within the adsorbent material. Limited studies have integrated gas composition analysis with material characterization techniques to explain the interaction between biomass fibers and gas molecules during the adsorption process. Therefore, a comprehensive understanding of both adsorption performance and molecular interaction mechanisms remains insufficient [20].

This study is distinct because it combines Gas Chromatography–Mass Spectrometry (GC–MS) analysis and Fourier Transform Infrared (FTIR) characterization to evaluate both methane enhancement performance and adsorption mechanisms in untreated banana fiber. Furthermore, the implementation of a fixed-bed upflow adsorption configuration provides a simple, low-cost, and practical purification system suitable for laboratory-scale and rural biogas upgrading applications. The novelty of this research lies not only in the use of untreated banana fiber as a sustainable adsorbent material, but also in the integration of performance evaluation and functional group characterization to explain the adsorption behavior of carbon dioxide in a biogas purification system. Therefore, this study aims to evaluate the effectiveness of banana fiber as a natural adsorbent for methane enhancement through carbon dioxide removal using GC–MS analysis, supported by FTIR characterization to explain the adsorption mechanism in a fixed-bed filtration system. This research is expected to contribute to the development of environmentally friendly and economically feasible biogas upgrading technologies for small-scale renewable energy applications [21]. In addition to conventional upgrading technologies, several studies have explored the use of packing materials and biofiltration systems for biogas purification. These approaches utilize natural or engineered media to enhance gas–solid interaction and improve removal efficiency of unwanted gases such as carbon dioxide and hydrogen sulfide [10], [11], [12]. Furthermore, hydrogen sulfide removal using bio-based adsorbents has also been widely investigated due to its corrosive nature and environmental impact [9].

2. METHODS

2.1 Materials

The materials used in this study consisted of banana fiber as a natural adsorbent and raw biogas obtained from an anaerobic digester. Banana fiber was selected due to its lignocellulosic composition, which includes cellulose, hemicellulose, and lignin that provide potential adsorption sites for gas molecules [5], [6]. The biogas used in this study was generated from the anaerobic digestion of organic waste and collected directly from the digester outlet. Biogas generally consists of methane (CH_4) and carbon dioxide (CO_2) as the main components, which determine its energy quality [2], [3]. Therefore, these two parameters were used as the main indicators in evaluating the performance of the adsorption process.

2.2 Experimental Setup

The experimental system was designed using a fixed-bed adsorption method to evaluate the performance of banana fiber in improving biogas quality. Fixed-bed systems are widely used in gas purification due to their simplicity, low cost, and effectiveness in adsorption processes [4]. Previous studies have demonstrated that the effectiveness of fixed-bed systems is influenced by parameters such as packing material characteristics, gas residence time, and flow configuration, which directly affect adsorption performance [10], [12].

2.2.1 Operational Parameters

Several operational parameters were controlled during the experimental process to ensure stable adsorption performance and reproducibility of the system. The fixed-bed adsorption column was constructed using a PVC tube with an inner diameter of 7.5 cm and a total height of 50 cm. The adsorption column was packed with approximately 250 g of untreated banana fiber using a loose packing configuration to maintain porosity and minimize pressure drop during gas flow.

The raw biogas flow rate was maintained at approximately 2 L/min using a manual flow control valve. The filtration process was conducted under atmospheric pressure conditions with an estimated gas residence time of approximately 45–60 seconds inside the adsorption column. The upflow configuration was selected to improve gas distribution and maximize gas–solid interaction between biogas and the banana fiber adsorbent.

The experiments were performed at ambient laboratory temperature ranging from 28–30°C. Gas samples were collected before filtration (inlet) and after filtration (outlet) using gas sampling bags for subsequent GC–MS analysis. All experiments were conducted in triplicate to ensure data reliability and reproducibility.

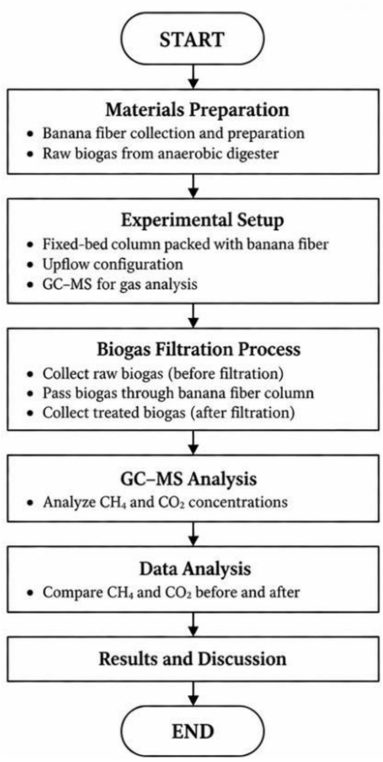

Figure 1. Research flowchart of biogas upgrading using banana fiber

Figure 1 illustrates the overall research workflow used in this study. The process begins with banana fiber preparation and raw biogas collection, followed by the adsorption filtration process using a fixed-bed system. The workflow also includes GC–MS analysis for gas composition evaluation and FTIR characterization to investigate the adsorption mechanism occurring in the banana fiber after filtration. The research procedure consisted of several stages, including banana fiber preparation, experimental setup, raw biogas collection, flow regulation, filtration process, gas sampling, GC–MS analysis, FTIR characterization, and data interpretation.

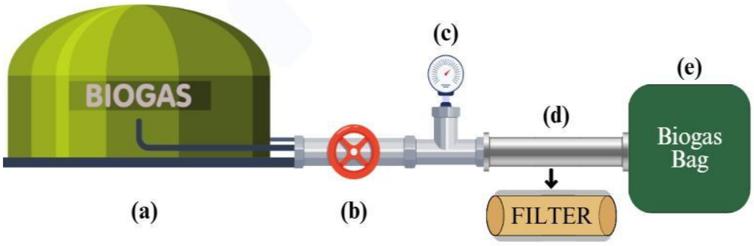

Figure 2. Schematic diagram of the experimental setup: (a) raw biogas source, (b) flow control valve, (c) monitoring gauge, (d) banana fiber filter column, and (e) biogas sampling bag

Figure 2 presents the schematic configuration of the fixed-bed biogas filtration system used in this study. The upflow system configuration was designed to improve gas distribution and increase contact between the biogas and the banana fiber adsorbent. The filtration column serves as the main adsorption chamber where carbon dioxide reduction and methane enrichment occur during the purification process. The system consisted of five main components. Raw biogas (a) was collected from the anaerobic digester outlet and directed into the system. The gas flow was regulated using a control valve (b) to maintain stable operating conditions. A monitoring gauge (c) was used to observe the gas flow condition during the experiment. The biogas was then passed through a fixed-bed filtration column (d) packed with banana fiber, where the adsorption process occurred. The system was operated using an upflow configuration to enhance gas–solid interaction and ensure uniform gas distribution within the column. After filtration, the treated biogas was collected in a sampling bag (e). Gas samples were collected before filtration (inlet) and after filtration (outlet) using biogas sampling bags. The samples were subsequently analyzed using Gas Chromatography–Mass Spectrometry (GC–MS) to determine methane (CH_4) and carbon dioxide (CO_2) concentrations. GC–MS analysis was conducted to quantitatively determine methane (CH_4) and carbon dioxide (CO_2) concentrations before and after filtration. The gas samples were analyzed under standardized laboratory conditions to ensure measurement consistency and accuracy. The obtained chromatograms were interpreted based on peak area percentage to evaluate changes in gas composition resulting from the adsorption process.

Table 1. Operational parameters of the adsorption system

Parameter	Value
Column material	PVC
Column diameter	7.5 cm
Column height	50 cm
Banana fiber mass	250 g
Flow rate	2 L/min
Residence time	45–60 s
Operating temperature	28–30°C
Flow configuration	Upflow
Experimental repetition	Triplicate

2.3 Banana Fiber Preparation and Characteristics

The banana fiber used in this study was obtained from agricultural residues. The fibers were cleaned using water to remove impurities such as dust and dirt. After cleaning, the fibers were air-dried to reduce moisture content while maintaining their natural structure.

Figure 3. Raw banana fiber used as natural adsorbent before filtration process

After drying, the fibers were cut into uniform lengths to ensure consistent packing within the filtration column. The banana fibers were packed uniformly inside the adsorption column with a loose packing arrangement to maintain adequate porosity, reduce channeling effects, and facilitate uniform gas distribution during the filtration process. To further understand the adsorption mechanism, the banana fiber was characterized using Fourier Transform Infrared (FTIR) spectroscopy before and after the biogas filtration process. FTIR analysis was conducted to identify functional groups present in the banana fiber and to observe changes in chemical structure due to interaction with biogas components. FTIR characterization was performed within the wavenumber range of 4000–500 cm^{-1} to identify functional groups involved in the adsorption process. The spectra obtained before and after filtration were compared to observe changes in peak intensity and peak position associated with interaction between banana fiber and carbon dioxide molecules. The FTIR spectra were analyzed to identify key functional groups such as hydroxyl (–OH), carbonyl (C=O), C–H, and C–O groups, which are known to play an important role in adsorption processes [6], [8]. Changes in peak intensity and peak position were used as indicators of interaction between banana fiber and carbon dioxide molecules

2.4 Data Analysis

The performance of banana fiber as a natural adsorbent was evaluated by comparing methane (CH_4) and carbon dioxide (CO_2) concentrations before and after filtration. The adsorption performance evaluation was based on average values obtained from three repeated experiments. The results were expressed as mean ± standard deviation to assess the consistency and repeatability of the adsorption process. Descriptive statistical analysis was applied to compare methane enhancement and carbon dioxide reduction before and after filtration. The percentage increase in methane concentration and the percentage reduction in carbon dioxide were calculated using the following equations:

$$CH^4 \text{ increase } (\%) = \frac{CH_{4,after} - CH_{4,before}}{CH_{4,before}} \times 100 \quad (1)$$

$$CO^2 \text{ reduction } (\%) = \frac{CO_{2,before} - CO_{2,after}}{CO_{2,before}} \times 100 \quad (2)$$

These calculations were used to evaluate the effectiveness of banana fiber in improving biogas quality.

3. RESULTS AND DISCUSSION

3.1 Methane (CH_4) Enhancement

The performance of banana fiber as a natural adsorbent was evaluated based on its ability to increase methane (CH_4) concentration in biogas. The experimental results are presented in Table 2.

Table 2. GC–MS results of biogas composition before and after filtration using banana fiber

Gas Component	Before Filtration (%)	After Filtration (%)
CH_4	51.37 ± 0.72	60.84 ± 0.95
CO_2	48.63 ± 0.68	39.15 ± 0.88

The results presented in Table 2 represent the average values obtained from three repeated experiments. The relatively low standard deviation values (< ±1.5%) indicate that the adsorption process showed good repeatability and stable operational performance under the selected experimental conditions. These findings demonstrate that the fixed-bed adsorption system using banana fiber produced consistent methane enhancement and carbon dioxide reduction during repeated filtration cycles.

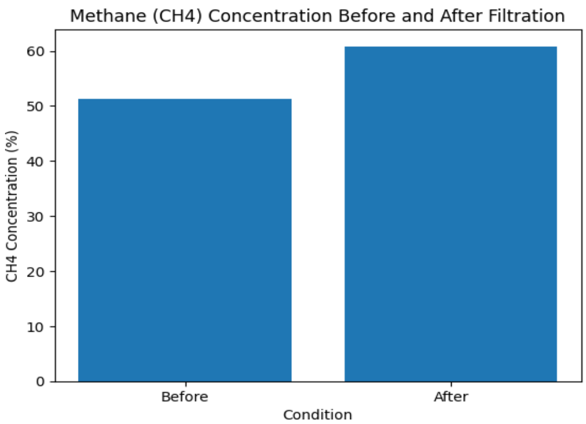

Figure 4. Methane (CH_4) concentration before and after filtration using banana fiber

Figure 4 illustrates the increase in methane concentration after the biogas filtration process using banana fiber. The increase in methane concentration indicates that the adsorption system effectively reduced non-combustible gases, particularly carbon dioxide, thereby increasing the relative methane fraction in the biogas mixture. The increase in methane concentration is not due to methane generation but rather a relative enrichment effect caused by the removal of non-combustible gases, particularly carbon dioxide (CO_2). As CO_2 concentration decreases, the volumetric fraction of methane increases proportionally, resulting in improved biogas quality [4]. The effectiveness of methane enrichment is closely related to the physical structure of banana fiber. The fibrous and porous morphology provides a large surface area, which enhances gas–solid interaction and facilitates selective adsorption of CO_2. This indirect mechanism results in increased methane concentration without altering the chemical structure of methane. Similar methane enrichment behavior has been reported in previous studies using bio-based adsorbents, where selective removal of non-combustible gases leads to an increase in methane concentration without altering its chemical composition [11], [13]. From a practical standpoint, the increase in methane concentration directly improves the calorific value of biogas, making it more suitable for applications such as cooking, heating, and electricity generation. These results indicate that banana fiber has strong potential as a low-cost material for biogas upgrading. From an engineering perspective, the methane enhancement observed in this study demonstrates the potential applicability of banana fiber for low-cost biogas upgrading systems. The increase in methane concentration contributes directly to higher calorific value and improved combustion efficiency, which are important parameters for household energy applications and small-scale electricity generation systems. The stable adsorption performance observed during repeated experiments also indicates that banana fiber can function effectively under continuous gas flow conditions.

3.2 Carbon Dioxide (CO_2) Reduction

The ability of banana fiber to reduce carbon dioxide (CO_2) concentration was also evaluated. The results show that CO_2 concentration decreased from 48.63% to 39.15%, corresponding to a reduction of 9.48% after filtration.

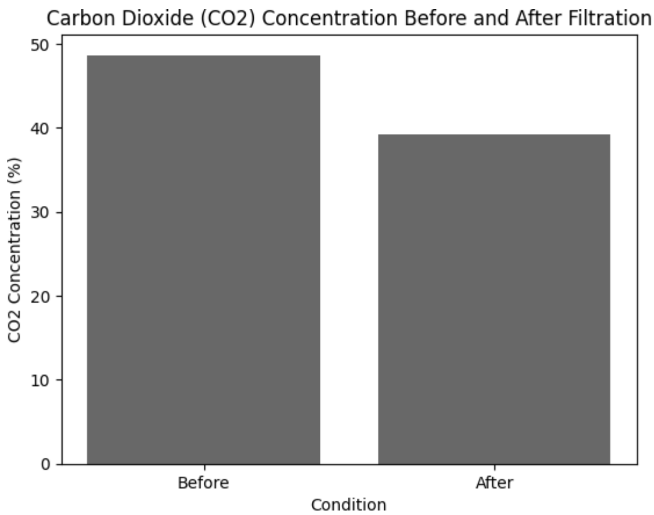

Figure 5. Carbon dioxide (CO_2) concentration before and after filtration using banana fiber

Figure 5 shows the decrease in carbon dioxide concentration after the adsorption process using banana fiber. The reduction in CO_2 concentration confirms the adsorption capability of the lignocellulosic structure of banana fiber, which provides active adsorption sites for gas molecule interaction. The reduction in CO_2 concentration can be explained through adsorption mechanisms occurring on the surface of banana fiber. This process can be described as:

$$CO2(g) + S \rightarrow CO2{\cdot}S \tag{3}$$

Where S represents the surface of the banana fiber acting as an adsorbent.

Banana fiber contains lignocellulosic components such as cellulose, hemicellulose, and lignin, which provide active sites for adsorption. Functional groups such as hydroxyl (–OH) and carboxyl (–COOH) play an important role in attracting CO_2 molecules through physical adsorption mechanisms, including hydrogen bonding and van der Waals interactions [5], [6]. In addition, the porous structure of banana fiber enhances diffusion and provides a large surface area, allowing more CO_2 molecules to be captured during the filtration process. The upflow configuration used in this study further improves gas–solid interaction and reduces channeling effects. Although the adsorption process is predominantly physical, the interaction between CO_2 and functional groups on the fiber surface contributes to the overall effectiveness of the system. The observed CO_2 reduction is consistent with previous findings on biomass-based adsorbents, where lignocellulosic materials have shown promising performance in capturing carbon dioxide due to their porous structure and functional group interactions [9], [10], [13].

3.3 FTIR Analysis of Banana Fiber

To further investigate the adsorption mechanism, Fourier Transform Infrared (FTIR) analysis was conducted to identify changes in the functional groups of banana fiber before and after the filtration process.

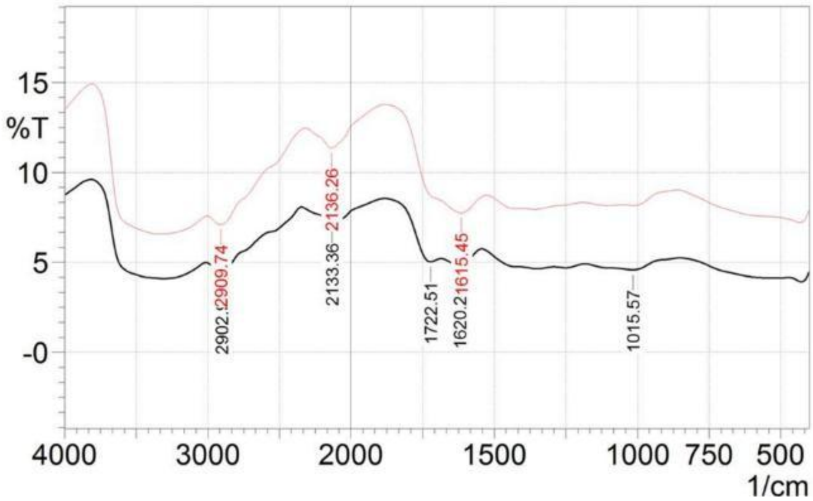

Figure 6. FTIR spectra of banana fiber before and after biogas filtration

Figure 6 presents the FTIR spectra of banana fiber before and after biogas filtration. The observed changes in peak intensity and the appearance of new absorption peaks indicate that interactions occurred between the banana fiber surface and biogas components during the adsorption process. The FTIR spectra of banana fiber before filtration show characteristic absorption bands at 3300–3500 cm^{-1} corresponding to hydroxyl (–OH) groups, 2909 cm^{-1} associated with C–H stretching, and 1615 cm^{-1} related to aromatic C=C bonds from lignin. These peaks confirm the typical lignocellulosic structure of banana fiber. After the filtration process, several changes in the FTIR spectra were observed. The intensity of the C–H stretching band decreased from 7.101 to 4.494, indicating partial degradation or interaction of cellulose components during the filtration process. In addition, new absorption peaks appeared at 1722 cm^{-1} and 1015 cm^{-1}, corresponding to carbonyl (C=O) and C–O functional groups, respectively. The emergence of these peaks suggests that chemical adsorption interactions occurred between the banana fiber and biogas components. The appearance of the carbonyl group (C=O) indicates possible oxidation or transformation of hydroxyl groups (–OH) during the adsorption process. This suggests that CO_2 molecules interact with the polar functional groups of banana fiber through surface interaction mechanisms. Furthermore, the presence of C–O stretching bands confirms the active role of cellulose in providing adsorption sites. The relatively stable aromatic C=C peak indicates that the lignin structure remains largely intact, suggesting that the fiber maintains its structural integrity during the filtration process. These FTIR results support the GC–MS findings, where CO_2 concentration decreased and methane concentration increased after filtration. Therefore, it can be concluded that banana fiber acts not only as a physical filter but also as an active adsorbent through a combination of physical adsorption and weak chemical interactions. Previous studies have also confirmed that natural fibers exhibit active functional groups that contribute significantly to adsorption processes. These functional groups play a crucial role in facilitating gas–solid interactions and enhancing adsorption efficiency [16], [17]. This result indicates that banana fiber has comparable performance to other biomass-based adsorbents reported in previous studies. Compared to previous studies using activated carbon or chemically modified biomass adsorbents, the methane enhancement achieved in this study demonstrates that untreated banana fiber can provide competitive adsorption performance while maintaining lower operational cost and simpler preparation procedures. Although the adsorption efficiency is still lower than some commercial adsorbent systems, the environmental sustainability and economic advantages of banana fiber make it highly promising for decentralized renewable energy applications.

Table 3. FTIR peak assignment of banana fiber before and after filtration

Wavenumber (cm^{-1})	Functional Group	Interpretation
3300–3500	–OH	Hydroxyl stretching vibration
2909	C–H	Cellulose stretching
1722	C=O	Carbonyl interaction after adsorption
1615	Aromatic C=C	Lignin structure
1015	C–O	Cellulose adsorption site

Although the adsorption results were promising, the adsorption capacity of banana fiber may decrease over prolonged operational periods due to saturation of active adsorption sites. Therefore, further studies are necessary to evaluate long-term adsorption performance, regeneration capability, and maximum adsorption capacity under varying operational conditions.

4. CONCLUSION

This study evaluated the performance of banana fiber as a natural adsorbent for biogas upgrading using a fixed-bed filtration system, focusing on methane (CH_4) enhancement and carbon dioxide (CO_2) reduction. The experimental results demonstrated that banana fiber effectively improved biogas quality through a simple and environmentally friendly adsorption process. GC–MS analysis showed that methane concentration increased from 51.37% to 60.84%, corresponding to an enhancement of 9.47%, while carbon dioxide concentration decreased from 48.63% to 39.15%, representing a reduction of 9.48%. These findings indicate that banana fiber can selectively adsorb carbon dioxide and contribute to methane enrichment in biogas systems. The FTIR characterization further confirmed the adsorption mechanism by revealing changes in functional groups after the filtration process. The decrease in C–H stretching intensity and the appearance of carbonyl (C=O) and C–O functional groups indicate that interactions occurred between the lignocellulosic structure of banana fiber and carbon dioxide molecules during adsorption. The results demonstrate that banana fiber functions not only as a physical filtration medium but also as an active adsorbent through surface interaction mechanisms. From a practical perspective, banana fiber offers several advantages, including low cost, wide availability, biodegradability, and environmental sustainability. The utilization of agricultural waste materials as adsorbents supports circular economy principles and provides a feasible alternative for small-scale and decentralized biogas upgrading systems, particularly in rural and developing regions. Despite the promising results, this study has several limitations. The adsorption performance was evaluated only under laboratory-scale conditions and within a relatively short operational period. The maximum adsorption capacity, saturation behavior, regeneration capability, and long-term stability of banana fiber were not investigated in this study. In addition, operational parameters such as humidity, pressure variation, packing density, and prolonged continuous gas flow may significantly influence adsorption efficiency and require further evaluation. Therefore, future studies are recommended to investigate adsorption capacity, breakthrough behavior, regeneration performance, multi-stage filtration systems, and optimization of operational parameters to improve long-term adsorption efficiency and support potential industrial-scale implementation of banana fiber-based biogas purification systems. Overall, this study demonstrates that untreated banana fiber has strong potential as a sustainable biomass-based adsorbent for low-cost biogas upgrading applications.

5. ACKNOWLEDGEMENT

The authors would like to thank the New Renewable and Conservation Energy Laboratory, Faculty of Engineering, Udayana University, and the Electrical Engineering Laboratory, Faculty of Engineering and Informatics, Undiknas University, for providing the facilities and support necessary to conduct this research.

6. REFERENCES

[1] Intergovernmental Panel on Climate Change (IPCC), Climate Change 2021: The Physical Science Basis. Cambridge University Press, 2021.

[2] E. Ryckebosch, M. Drouillon, and H. Vervaeren, "Techniques for transformation of biogas to biomethane," Biomass and Bioenergy, vol. 35, no. 5, pp. 1633–1645, 2011. doi:

10.1016/j.biombioe.2011.02.033
[3] M. Andlar, H. Belskaya, G. Morzak, M. Ivančić Šantek, T. Rezić, V. Petravić Tominac, and B. Šantek, "Biogas production systems and upgrading technologies: A review," Food Technology and Biotechnology, vol. 59, no. 4, pp. 387–412, 2021. doi: 10.17113/ftb.59.04.21.7300.
[4] Q. Sun, H. Li, J. Yan, L. Liu, Z. Yu, and X. Yu, "Selection of appropriate biogas upgrading technology—A review of biogas cleaning, upgrading and utilisation," Renewable and Sustainable Energy Reviews, vol. 51, pp. 521–532, 2015. doi: 10.1016/j.rser.2015.06.029.
[5] S. Li, X. Yuan, S. Deng, L. Zhao, and K. B. Lee, "A review on biomass-derived CO_2 adsorption capture: Adsorbent, adsorber, adsorption, and advice," Renewable and Sustainable Energy Reviews, vol. 152, 111708, 2021. doi: 10.1016/j.rser.2021.111708.
[6] M. Sevilla and A. B. Fuertes, "CO_2 adsorption by activated templated carbons," Journal of Colloid and Interface Science, vol. 366, no. 1, pp. 147–154, 2012. doi: 10.1016/j.jcis.2011.09.038.
[7] K. K. Pandey, "A study of chemical structure of soft and hardwood and wood polymers by FTIR spectroscopy," Journal of Applied Polymer Science, vol. 71, no. 12, pp. 1969–1975, 1999. doi: 10.1002/(SICI)1097-4628(19990321)71:12<1969::AID-APP6>3.0.CO;2-D
[8] P. Weiland, "Biogas production: Current state and perspectives," Applied Microbiology and Biotechnology, vol. 85, no. 4, pp. 849–860, 2010. doi: 10.1007/s00253-009-2246-7.
[9] N. N. Zulkefli, M. S. Masdar, W. N. R. Wan Isahak, J. M. Jahim, S. A. M. Rejab, and C. C. Lye, "Removal of hydrogen sulfide from a biogas mimic by using impregnated activated carbon adsorbent," PLOS ONE, vol. 14, no. 2, e0211713, 2019. doi: 10.1371/journal.pone.0211713.
[10] I. W. Sutama, I. N. S. Winaya, I. B. A. Swamardika, R. S. Hartati, I. M. P. T. Prakasa and A. P. Abiyasa, "Performance Evaluation of Coconut Shell Carbon Fe_2O_3 Composite Filters for Biogas Purification," 2025 International Conference on Smart-Green Technology in Electrical and Information Systems (ICSGTEIS), Denpasar, Bali, Indonesia, 2025, pp. 25-29, doi: 10.1109/ICSGTEIS68532.2025.11284472.
[11] M. Bałys, E. Brodawka, G. S. Jodłowski, J. Szczurowski, and M. Wójcik, "Alternative Materials for the Enrichment of Biogas with Methane," Materials, vol. 14, no. 24, 7759, 2021. doi: 10.3390/ma14247759.
[12] R. Muñoz, L. Meier, I. Diaz, and D. Jeison, "A review on the state-of-the-art of physical/chemical and biological technologies for biogas upgrading," Reviews in Environmental Science and Bio/Technology, vol. 14, pp. 727–759, 2015. doi: 10.1007/s11157-015-9379-1.
[13] A. A. Olajire, "CO_2 capture and separation technologies for end-of-pipe applications—A review," Energy, vol. 35, no. 6, pp. 2610–2628, 2010. doi: 10.1016/j.energy.2010.02.030.
[14] P. H. L. Nguyen, P. Kuruparan, and C. Visvanathan, "Anaerobic digestion of municipal solid waste as a treatment prior to landfill," Bioresource Technology, vol. 98, no. 2, pp. 380–387, 2007. doi: 10.1016/j.biortech.2005.12.018.
[15] M. Mohammed, I. Ozbay, and E. Durmusoglu, "Bio-drying of green waste with high moisture content," Process Safety and Environmental Protection, vol. 111, pp. 420–427, 2017. doi: 10.1016/j.psep.2017.08.002.
[16] D. Haldar, N. Bhattacharjee, A. M. Shabbirahmed, A. G. Sathyanesan, A. K. Patel, J. S. Chang, C. D. Dong, and R. R. Singhania, "Purification of biogas for methane enrichment using biomass-based adsorbents: A review," Biomass and Bioenergy, vol. 173, 106804, 2023. doi: 10.1016/j.biombioe.2023.106804.
[17] I. Angelidaki, L. Treu, P. Tsapekos, G. Luo, S. Campanaro, H. Wenzel, and P. G. Kougias, "Biogas upgrading and utilization: Current status and perspectives," Biotechnology Advances, vol. 36, no. 2, pp. 452–466, 2018. doi: 10.1016/j.biotechadv.2018.01.011.
[18] R. Kapoor, P. Ghosh, B. Tyagi, V. K. Vijay, V. Vijay, I. S. Thakur, H. Kamyab, D. D. Nguyen, and A. Kumar, "Advances in biogas valorization and utilization systems: A comprehensive review," Journal of Cleaner Production, vol. 273, 123052, 2020. doi: 10.1016/j.jclepro.2020.123052.
[19] M. S. Shafeeyan, W. M. A. W. Daud, A. Houshmand, and A. Shamiri, "A review on surface modification of activated carbon for carbon dioxide adsorption," Journal of Analytical and Applied Pyrolysis, vol. 89, no. 2, pp. 143–151, 2010. doi: 10.1016/j.jaap.2010.07.006.
[20] L. Chinea, J. C. Abanades, and M. C. Romano, "Methane enrichment of biogas using carbon capture materials," Fuel, vol. 337, 127161, 2023. doi: 10.1016/j.fuel.2022.127161.

LOGIC (JOURNAL ENGINEERING DESIGN AND TECHNOLOGY)
Journal Engineering Design and Technology
Vol. 26 No.2 July 2026 ; p. 157 - 166
Journal Homepage : http://ojs2.pnb.ac.id/index.php/LOGIC
p-ISSN : 1412-114X e-ISSN : 2580-5649

Numerical Analysis of Outlet Number Effects on Temperature Distribution in a Briquette Oven Using CFD

Alviani Hesthi Permata Ningtyas [1)*], Siti Duratun Nasiqiati Rosady [2)], Muhammad Wildanus Sholih [3)]

1) Prodi Teknik Mesin, Fakultas Teknik, Universitas Muhammadiyah Gresik, Gresik, Indonesia
2) D3 Teknik Mesin, Jurusan Teknik Mesin, Politeknik Negeri Malang, Malang, Indonesia
3) Prodi Teknik Mesin, Fakultas Teknik, Universitas Muhammadiyah Gresik, Gresik, Indonesia

Corresponding email [1)*] :
alvianihesthi@umg.ac.id

Abstract. The performance of briquette drying systems is strongly influenced by airflow distribution and thermal uniformity within the drying chamber, which are governed by outlet configuration and internal flow patterns. However, limited studies have systematically quantified the effect of exhaust outlet arrangements on the coupled heat transfer and fluid flow behavior in industrial-scale briquette ovens. This study aims to numerically investigate the influence of single-, double-, and four-outlet configurations on airflow characteristics, temperature distribution, and overall thermal performance of a briquette drying oven. A three-dimensional geometric model representing the combustion chamber, drying chamber, and briquette racks was developed and analyzed using Computational Fluid Dynamics (CFD). Steady-state simulations were performed in ANSYS Fluent employing the standard k–ε turbulence model, with air properties, inlet velocity (9.97 m/s), and thermal boundary conditions defined based on operational data. The results reveal that outlet configuration significantly affects flow recirculation intensity and temperature uniformity across the briquette racks. The four-outlet configuration produced the most homogeneous airflow distribution and reduced thermal gradients, thereby enhancing convective heat transfer effectiveness compared to single- and double-outlet designs. Conversely, the single-outlet case exhibited pronounced recirculation zones and localized temperature variations, potentially leading to uneven drying. These findings demonstrate that optimizing outlet arrangement is a critical design parameter for improving drying efficiency and energy utilization in briquette oven systems, providing a validated numerical framework for future thermal system optimization.

Keywords : Computational Fluid Dynamics, Heat Transfer, Outlet Configuration.

1. INTRODUCTION

The drying process of briquettes represents a critical stage in biomass thermal processing[1]–[3], where moisture removal occurs through coupled heat and mass transfer mechanisms[4]–[7]. Proper drying significantly improves calorific value, mechanical integrity, storage stability, and combustion performance, thereby enhancing the viability of briquettes as a sustainable alternative energy source. Achieving uniform temperature distribution and efficient heat transfer within the drying chamber is essential to prevent uneven drying, cracking, or quality degradation of the final product[8]–[11].

Previous studies have investigated various drying technologies[3], [12]–[20], including solar-assisted and forced-convection systems, highlighting the importance of airflow management in improving drying efficiency. While these studies report improvements in thermal performance and moisture removal rates, limited attention has been given to the influence of exhaust outlet configuration on internal airflow structure and temperature uniformity. In forced-convection drying ovens, outlet placement plays a crucial role in controlling flow recirculation patterns, pressure distribution, and convective heat transfer across product racks. However, systematic numerical investigations comparing different outlet arrangements under identical operating conditions remain scarce.

Furthermore, experimental evaluation of airflow and temperature distribution inside industrial drying chambers is often challenging due to measurement limitations and spatial constraints. Computational Fluid Dynamics (CFD) offers a robust alternative by enabling detailed visualization of velocity fields, thermal gradients, and recirculation zones within complex geometries[1], [3], [4], [19], [20].

Therefore, this study aims to numerically investigate the influence of single-, double-, and four-outlet configurations on airflow characteristics and temperature distribution inside a briquette drying oven. By employing three-dimensional CFD simulations under steady-state forced convection conditions, this research provides a comparative assessment of outlet designs and identifies the configuration that ensures the most uniform thermal environment. The findings contribute to the optimization of drying chamber design and support the development of more efficient biomass drying systems.

Although briquette drying is fundamentally governed by coupled heat and mass transfer processes, the present study focuses exclusively on the thermal-fluid behavior within the drying chamber. The primary objective is to investigate how different outlet configurations influence airflow distribution, temperature uniformity, and convective heat transfer characteristics. Moisture transport, evaporation mechanisms, and drying kinetics were not included in the present numerical model and are therefore beyond the scope of this investigation. Nevertheless, improving temperature uniformity is expected to provide favorable thermal conditions for subsequent moisture removal. Future work will incorporate coupled heat-and-mass transfer modeling to predict moisture distribution and drying kinetics more comprehensively.

2. METHODS

2.1 Geometrical Modeling and Configurations

A three-dimensional model of the briquette drying oven was developed using Autodesk Inventor 2025 based on actual industrial dimensions. The system consists of a combustion chamber, a drying chamber, insulated steel walls, and multiple briquette holding racks. The oven has a total internal area of 6 m², as summarized in Table 1. To evaluate the effect of exhaust design,

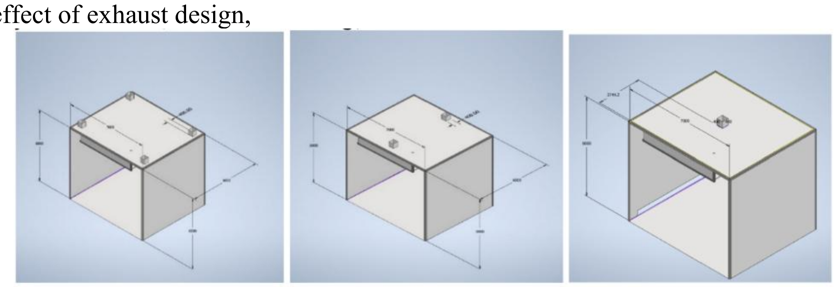

Figure 1. Temperature distribution on the YZ plane for: (a) single outlet, (b) double outlet and (c) four outlets

As illustrated in Figure 1(a–c), the outlet positions were varied on the top surface while maintaining identical chamber geometry and inlet conditions. This approach ensured that performance differences were solely attributed to outlet arrangement. The CAD models were exported in STEP format and imported into ANSYS Workbench for Computational Fluid Dynamics (CFD) analysis.

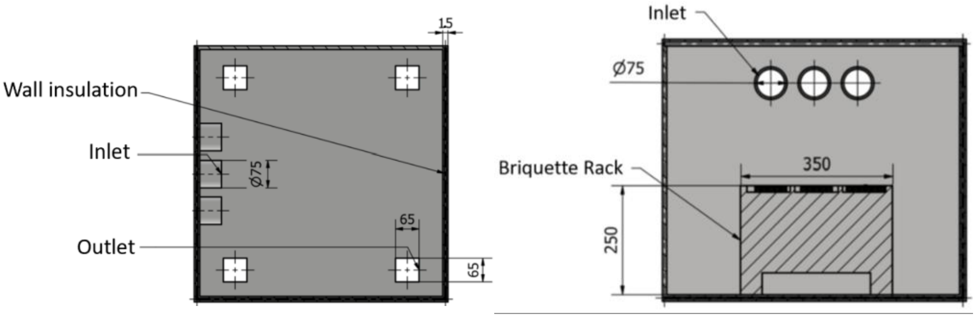

Figure 2. (a)Top View and (b) front view on four outlet oven

The technical drawing in Figure 2 provides the orthogonal views of a four-outlet industrial oven, detailing its top and front configurations alongside a 15 mm thick thermal wall insulation layer. The flow system consists of three parallel inlets with a diameter Ø75 mm on the left wall that feed into the heating chamber from combustion chamber, which then exhaust symmetrically via four 65 mm × 65 mm square outlets situated at the corners. Furthermore, the front view reveals that a 350 mm wide briquette rack is positioned at a height of 250 mm within the oven cavity, directly beneath the horizontally aligned inlet ports to intercept the incoming convective airflow.

Table 1. Geometry Spesification

Descriptions	Value
Oven length	7000 mm
Width	3000 mm
Height	6000 mm
Wall Material	Coated Stell
Inlet diameter	75 cm
Outlet size	65 x 65 cm
Insulation	Glasswool thk. 1.5 mm
Rack dimension	90 x 250 x 350 cm
Capacity	5 Tons

The data provided in Tabel 1. shows the structural and geometric specifications of an industrial oven with an overall capacity of 5 Tons. Constructed with coated steel walls, the primary dimensions of the oven cavity span a length of 7000 mm, a width of 3000 mm, and a height of 6000 mm, supplemented by a 1.5 mm thick glasswool insulation layer. The thermal processing chamber also features a 75 cm inlet diameter, 65 x 65 cm outlets, and houses an internal rack with dimensions of 90 x 250 x 350 cm.

2.2. Governing Equations and Physical Modeling

The airflow and heat transfer inside the drying chamber were modeled using the steady-state, three-dimensional Reynolds-Averaged Navier–Stokes (RANS) equations for incompressible flow[21]–[25]. The governing continuity equation is expressed as Eq. (1)

$$\nabla \cdot u = 0 \tag{1}$$

ensuring mass conservation. The momentum equations are written as Eq. (2)

$$\rho(u \cdot \nabla)u = -\nabla p + \nabla \cdot [(\mu + \mu_t)(\nabla u + \nabla u^T)] + \rho g \tag{2}$$

where ρ is the fluid density, u is the velocity vector, p is the pressure, μ is the dynamic viscosity, and μ_t is the turbulent (eddy) viscosity. Heat transfer is governed by the energy equation as Eq. (3)

$$\rho c_p(\mathbf{u} \cdot \nabla)T = \nabla \cdot \left[\left(k + \frac{\mu_t c_p}{Pr_t}\right)\nabla T\right] + S_T \tag{3}$$

where T is temperature, c_p the specific heat capacity, k is the thermal conductivity, and Pr_t is the turbulent Prandtl number[26], [27]. Turbulence effects were represented using the standard k_ε model, in which the turbulent viscosity is defined as Eq. (4)

$$\mu_t = \rho C_\mu \frac{k^2}{\varepsilon} \tag{4}$$

The transport equations for turbulent kinetic energy (k) and its dissipation rate (ε) are solved to close the RANS system, incorporating production and dissipation terms with the standard model constants $C_\mu = 0.09$, $C_{1\varepsilon} = 1.44$, $C_{2\varepsilon} = 1.92$, $\sigma_k = 1.0$, and $\sigma_\varepsilon = 1.3$. This formulation ensures reliable prediction of internal forced convection and thermal distribution within the drying chamber[28]–[32].
Air was defined as a Newtonian fluid with properties listed in Table 2.

Table 2. Data input for reference value

Descriptions	Value
Area of Oven (A)	6 m^2
Dynamic Viscosity (μ)	1.7894×10^{-5} kg/(m·s)
Temperature (T)	40,3 °C
Velocity (v)	9,97 m/s
Density (ρ)	1,225 Kg/m^3

The total heat transfer rate was evaluated using the surface integral function available in ANSYS Fluent. The calculation was performed by integrating the local wall heat flux over all heated internal surfaces of the drying chamber according to Eq. 5 below

$$Q = \int_A q'' \, dA \tag{5}$$

where Q is the total heat transfer rate (W), q" is the local wall heat flux (W/m²), and A represents the heated wall surface area.

The total heat transfer rate was extracted using the Reports then Surface Integrals then Total Heat Transfer Rate function in ANSYS Fluent after the numerical solution had reached convergence. The evaluated surfaces included the heated chamber walls and the combustion-side heat transfer surfaces that supplied thermal energy to the drying chamber. The reported values therefore represent the net convective heat transferred from the heated walls to the circulating air under steady-state operating conditions.
Since the numerical simulations were conducted under steady-state conditions, the reported heat transfer rate corresponds to the converged solution rather than a transient time-dependent response.

2.3. Mesh Generation
The computational domain, shown schematically in Figure 2, includes the blower inlet, drying racks, and outlet ducts.

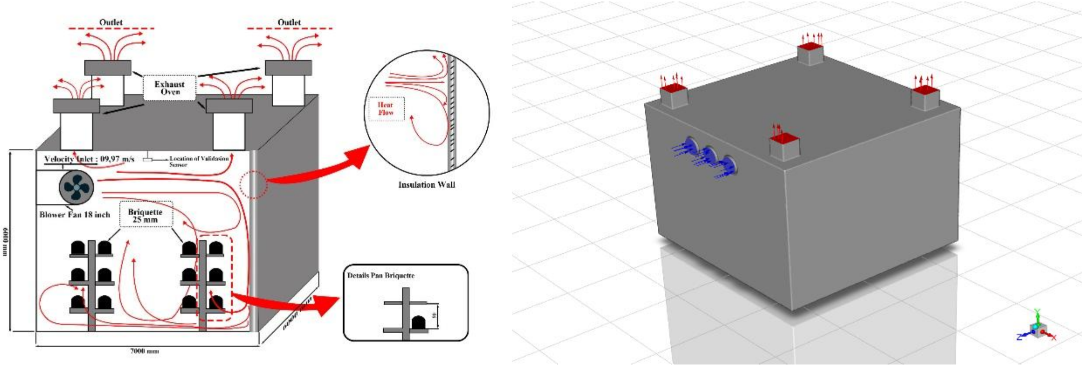

(a) (b)

Figure 3. (a) Schematic and (b) CFD Model of the Forced-Convection Briquette Drying Chamber

The figure 3 illustrates the geometric configuration and airflow characteristics of a forced-convection briquette drying chamber used for thermal performance evaluation. Figure 3.(a) presents the internal arrangement, including an 18-inch blower fan generating an inlet air velocity of approximately 10 m/s, vertically stacked briquettes, exhaust outlets positioned at the top surface, and insulated chamber walls to minimize heat loss. The airflow pattern indicates recirculation zones near the lower region and along the side walls, suggesting potential non-uniform temperature and velocity distributions within the drying space. The three-dimensional CFD model (right) represents the computational domain with defined inlet and outlet boundary conditions, enabling detailed simulation of internal flow structures and heat transfer mechanisms. Collectively, the model highlights the influence of chamber geometry, insulation, and forced airflow on convective heat transfer effectiveness and drying uniformity.

Table 3. Grid Indepedence

Geometry	Cells (million)	Skewness Mesh	THTR [W]	Temperature Thermocouple °C	Error %
Oven 4 Outlet Mesh 1	1.4	0.79889	932	78.5	0.64
Oven 4 Outlet Mesh 2	1.5	0.81121	909	82	-3.66
Oven 4 Outlet Mesh 3	2.1	0.79999	863	79.1	-0.13
Oven 4 Outlet Mesh 4	2.5	0.82122	911	83	-4.82

The data in Table 3. Grid Independence presents a mesh independence study evaluating four different computational grids (Mesh 1 to Mesh 4) for the four-outlet oven geometry based on cell count, skewness, total heat transfer rate (THTR), thermocouple temperature, and percentage error. Mesh 1 consists of 1.4 million cells with a mesh skewness of 0.79889, yielding a total heat transfer rate of 932 W and a thermocouple temperature of 78.5°C, which results in a low relative error of 0.64%. Despite having the coarsest resolution among the tested configurations, Mesh 1 represents a highly favorable choice for the final simulation because it balances numerical accuracy with computational efficiency, providing reliable thermal prediction metrics while keeping computational resource demands to a minimum.

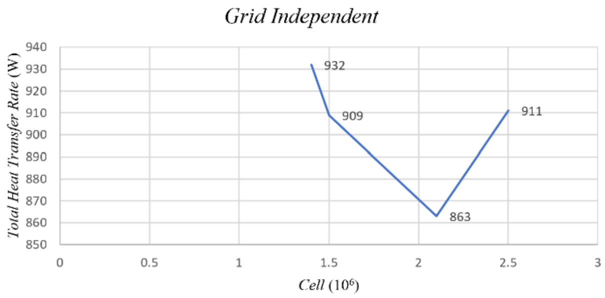

Figure 4. Grid Independence Index

The figure 4 presents the grid independence analysis showing the variation of total heat transfer rate with increasing mesh cell numbers. As the mesh is refined beyond approximately 2.1 × 10^6 cells, the predicted heat transfer rate stabilizes with minimal deviation, indicating that the solution has reached grid-independent behavior.

Special attention was given to boundary layer resolution to capture velocity and thermal gradients.

(a)

(b)

Figure 5. Experimental Briquette Drying Oven Used for CFD Validation (a) oven front view and (b) blower

The figure 5. presents the actual forced-convection briquette drying oven employed for experimental validation of the CFD simulation results. Figure 5. (a) shows the internal drying chamber equipped with multi-level trays for briquette placement, allowing evaluation of temperature and airflow distribution across different vertical positions. Figure 5(b) illustrates the axial blower fan installed to generate forced air circulation within the chamber. This experimental setup was used to measure airflow temperature profiles, providing validation data for comparison with numerical predictions and ensuring the reliability and accuracy of the thermal-fluid simulation model.

3. RESULTS AND DISCUSSION

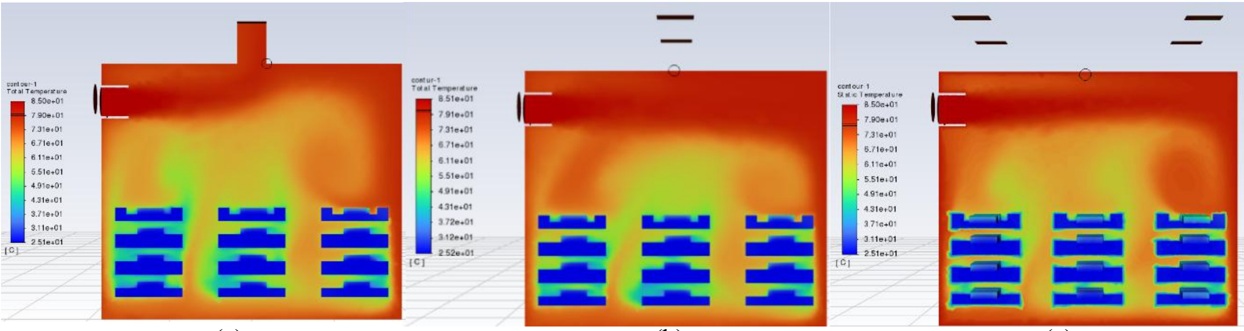

(a) (b) (c)

Figure 6. Temperature distribution YZ plane on (a) 1 outlet, (b) 2 outlets and (c) 4 outlets.

Figure 6 compares the static temperature distribution inside the drying chamber for three exhaust configurations: (a) single exhaust, (b) dual exhausts, and (c) four exhausts. In the single-exhaust configuration as figure 6.(a) pronounced thermal gradient is observed, with significant temperature accumulation in the upper region and non-uniform heat penetration toward the briquette layers. This indicates limited air circulation and localized heat stagnation. When two exhausts are applied as figure 6.(b), the temperature field becomes more evenly distributed, although moderate stratification remains near the central upper zone, suggesting partial improvement in convective heat removal. In contrast, the four-exhaust configuration as figure 6.(c) demonstrates the most uniform temperature distribution, characterized by reduced hot spots near the ceiling and more homogeneous heat diffusion around the briquette stacks. The enhanced uniformity indicates improved airflow circulation and more effective convective heat transfer, leading to better thermal balance within the chamber. Overall, increasing the number of exhaust outlets significantly mitigates thermal stratification and promotes more consistent drying conditions.

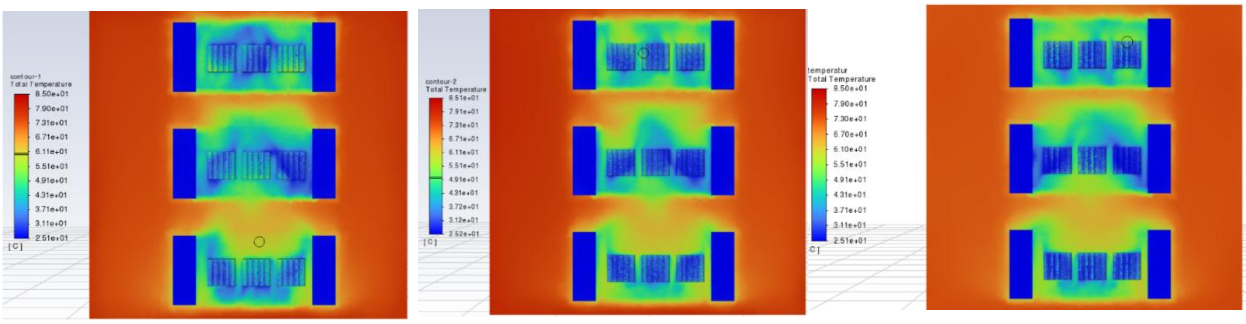

(a) (b) (c)

Figure 7. Temperature distribution plane XZ on (a) 1 outlet, (b) 2 outlets and (c) 4 outlets.

Figure 7 presents the temperature distribution on the XZ plane for configurations with (a) 1 exhaust, (b) 2 exhausts, and (c) 4 exhausts inside the drying chamber. In the single-exhaust configuration, the heat distribution appears less uniform, with high-temperature regions concentrated in specific areas, whereas increasing the number of exhausts to two and four improves temperature uniformity around the drying racks. The four-exhaust configuration demonstrates the most homogeneous thermal distribution and reduces extreme temperature gradients, indicating its potential to enhance drying uniformity and overall thermal performance.

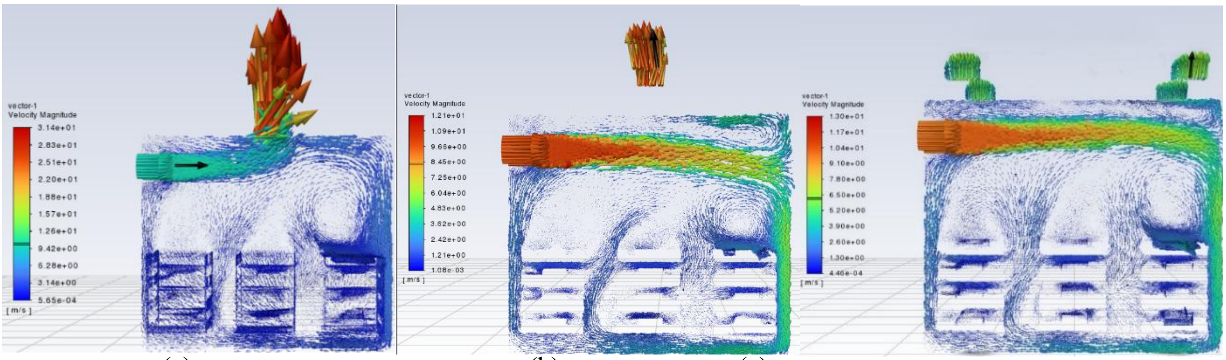

(a) (b) (c)

Figure 8. Velocity vector on ZX plane in (a) 1 outlet, (b) 2 outlets and (c) 4 outlets.

Figure 8 shows that the highest velocity regions are concentrated near the inlet duct and exhaust outlets, indicated by the red–orange vectors, where the airflow is directly driven by the blower and extracted through the vents. In contrast, low-velocity zones (blue regions) are observed inside the chamber, particularly around the lower racks and corner areas, where recirculation and flow stagnation occur. As the number of exhausts increases from one to four, the high-velocity jet becomes more distributed along the upper section, while low-velocity regions inside the chamber are reduced, resulting in more uniform airflow circulation.

To complement the qualitative interpretation of the temperature contours, the thermal performance of each outlet configuration was quantitatively evaluated using four representative parameters: maximum temperature, minimum temperature, average temperature, and total heat transfer rate. These parameters provide an objective assessment of the influence of outlet arrangement on heat distribution and convective heat transfer inside the briquette drying chamber.

Tabel 4. Quantitative thermal performance comparison for different outlet configurations.

Parameter	1 Outlet	2 Outlets	4 Outlets
Maximum Temperature (°C)	79.0	79.1	77.0
Minimum Temperature (°C)	35.0	37.0	57.0
Average Temperature (°C)	39.0	41.0	42.0
Total Heat Transfer Rate (W)	3322	4720	4754

The quantitative results presented in Table 4 demonstrate that the outlet configuration significantly influences the thermal performance of the drying chamber. The maximum temperature remains relatively constant, ranging from 77.0°C to 79.1°C, indicating that the heat source supplies nearly the same thermal energy in all configurations. Therefore, the primary effect of increasing the number of outlets is not to increase the peak temperature, but rather to improve the distribution of heat within the drying chamber.

A more pronounced difference is observed in the minimum temperature. The minimum temperature increases from 35.0°C in the single-outlet configuration to 37.0°C in the double-outlet configuration and reaches 57.0°C in the four-outlet configuration. Compared with the single-outlet design, the four-outlet configuration increases the minimum temperature by approximately 62.9%, indicating that cold regions are substantially reduced. This result suggests a significant improvement in temperature uniformity throughout the chamber, which is beneficial for achieving more consistent drying conditions.

The average chamber temperature also increases from 39.0°C for the single outlet to 41.0°C and 42.0°C for the double- and four-outlet configurations, respectively. Although the increase in average temperature is relatively modest, it indicates that thermal energy is distributed more effectively throughout the drying chamber. The higher average temperature, together with the increased minimum temperature, demonstrates that the additional outlets improve thermal utilization without substantially increasing the peak temperature.

The influence of outlet configuration is further confirmed by the total heat transfer rate. The single-outlet configuration produces a total heat transfer rate of 3322 W, whereas the double- and four-outlet configurations achieve 4720 W and 4754 W, respectively. Relative to the single-outlet configuration, the total heat transfer rate increases by approximately 42.1% for the double-outlet configuration and 43.1% for the four-outlet configuration. Although the difference between the double- and four-outlet configurations is relatively small (approximately 0.7%), the four-outlet configuration consistently exhibits the highest heat transfer rate while simultaneously providing the highest minimum temperature and the most uniform thermal field. These results indicate that increasing the number of outlets improves convective heat transfer efficiency and promotes a more homogeneous thermal environment inside the drying chamber.

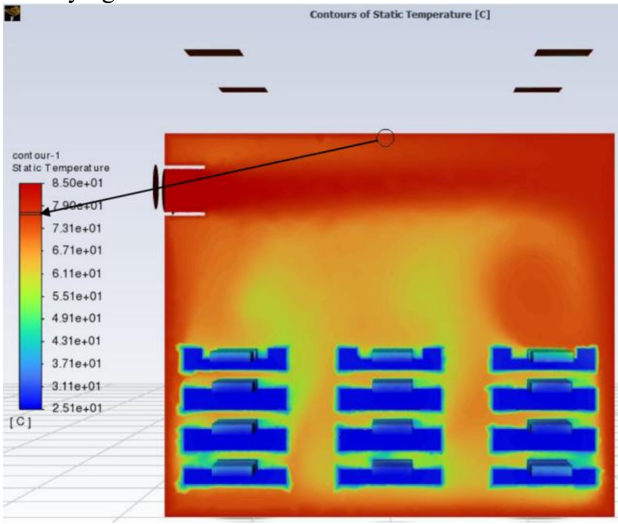

Figure 9. location that take temperature to compare with actual condition

Figure 9 illustrates the static temperature contour on the YZ mid-plane of the oven chamber equipped with four exhaust outlets. This sectional visualization provides insight into the internal thermal field and reveals the spatial temperature gradient along the vertical (Y) and transverse (Z) directions. The distribution demonstrates a relatively uniform thermal region in the core zone, with mild gradients observed near the exhaust boundaries, indicating the influence of convective heat removal on local temperature stratification.

The CFD simulation predicts a representative mid-plane temperature of 78.5°C, whereas experimental measurements obtained under identical operating conditions indicate a temperature of 79°C. The relative deviation between numerical and experimental results was quantified using:

$$\text{Error } (\%) = \frac{T_{\text{oven}} - T_{\text{simulation}}}{T_{\text{simulation}}} \times 100$$

Substitution of the measured values yields:

$$\text{Error } (\%) = \frac{79 - 78.5}{78.5} \times 100 = 0.63\%$$

A discrepancy of only 0.63% confirms a high level of agreement between simulation and experimental data. In heat transfer validation studies, an error below 5% is generally considered acceptable for engineering applications; therefore, the present deviation indicates excellent predictive accuracy of the numerical model.

The minor difference can be attributed to unavoidable experimental uncertainties (thermocouple accuracy and positioning sensitivity), assumptions of uniform material properties, idealized boundary conditions, and potential simplifications in turbulence modeling. Nevertheless, the close correlation suggests that the governing equations for coupled momentum and energy transport were properly resolved and that the mesh and numerical schemes were sufficiently refined to capture the dominant convective heat transfer mechanisms within the drying chamber.

Furthermore, the observed temperature uniformity in the mid-plane implies that the four-exhaust configuration effectively enhances air circulation and reduces localized thermal accumulation. This finding supports the suitability of the current exhaust design for achieving homogeneous drying conditions, which is critical for maintaining briquette quality and minimizing moisture gradients.

Overall, the strong agreement between numerical prediction and experimental measurement validates the robustness of the CFD model and establishes a reliable foundation for subsequent parametric optimization studies involving exhaust arrangement, airflow rate, and thermal efficiency enhancement.

4. CONCLUSION

This study systematically evaluated the influence of exhaust outlet configuration on airflow behavior and thermal performance in a forced-convection briquette drying oven using three-dimensional Computational Fluid Dynamics (CFD) simulations supported by experimental validation. A grid independence study ensured numerical stability, and comparison with measured mid-plane temperatures yielded a relative deviation of only 0.63%, confirming high predictive accuracy of the model. The results demonstrate that outlet configuration significantly affects internal flow topology and temperature uniformity. The single-exhaust design produced strong thermal stratification and localized recirculation zones, leading to uneven heat distribution across briquette layers. The dual-exhaust configuration improved airflow symmetry but still exhibited moderate temperature accumulation near the upper chamber. In contrast, the four-exhaust configuration achieved the most uniform thermal field, minimized stagnant regions, and enhanced convective heat transfer stability during both transient and steady regimes. These findings indicate that exhaust arrangement is a critical design parameter that directly governs convective circulation and drying uniformity rather than serving merely as a structural feature. The validated numerical framework developed in this study provides a practical basis for optimizing industrial biomass drying chambers to improve thermal efficiency and product quality, with future work should incorporate coupled heat-and-mass transfer, moisture diffusion, and drying kinetics to provide a more comprehensive prediction of briquette drying performance. Integrating moisture transport with CFD simulations would enable direct evaluation of drying rate, moisture distribution, and overall thermal efficiency, thereby extending the applicability of the present numerical framework to practical industrial drying processes.

5. ACKNOWLEDGEMENT

The authors would like to express their sincere gratitude to all parties who have supported the completion of this research. The authors gratefully acknowledge the financial support provided by the Directorate of Research and Community Service (DPPM), Universitas Muhammadiyah Gresik.

6. REFERENCES

[1] B. Rayianom, “Analisis Perpindahan Panas Pada Oven Pengering Brem Guna Meningkatkan Kinerja Dan Efektivitas Alat Dengan Metode Panas Pada Oven Pengering Brem,” pp. 1–8, 2023.

[2] O. V. No, M. F. Nurrohman, and G. A. Pohan, “Jurnal Mesin Material Manufaktur dan Energi Desain Dan Simulasi Distribusi Panas Pada Oven Untuk Proses Powder coating Menggunakan Ansys Fluent,” vol. 5, no. 2, pp. 75–84, 2025.

[3] G. Bahari, I. S. Irawati, I. A. Hendaryanto, I. Ayu, and P. Pratiwi, “Simulasi Computational Fluid Dynamics (CFD) untuk Optimalisasi Proses Perekatan pada Oven Bambu Laminasi,” vol. 16, no. 01, pp. 232–239, 2025, doi: 10.35970/infotekmesin.v16i1.2567.

[4] I. R. A. Jurnal, T. Mesin, S. M. Rohman, A. Mukhtar, and A. Burhanudin, “Simulasi Laju Aliran Udara pada Mesin Oven Pengering Kerupuk dengan Burner Sederhana Berbasis Computational Fluid Dynamics Simulation of Air Flow Rate in a Cracker Drying Oven Machine with a Simple Burner Based on Computational Fluid Dynamics,” vol. 3, no. 2, pp. 38–47, 2024.

[5] I. R. A. Jurnal, T. Mesin, and J. D. Hasibuan, “Pemodelan Numerik Perpindahan Panas pada Dinding Ruang Bakar Boiler Menggunakan Software Engineering Numerical Modeling of Heat Transfer in Boiler Combustion Chamber Walls Using Software Engineering,” vol. 2, no. 2, pp. 81–90, 2023.

[6] K. M. R. Khadafi, F. Putri, and O. M. Utami, “Analisis Kegagalan Pipa Embedded Pada PLTU TE 3x10 MW,” vol. 5, no. 2, pp. 48–55, 2024.

[7] N. Titahelu, S. J. Litiloly, J. T. Mesin, F. Teknik, U. Pattimura, and K. Poka-ambon, “Analisis laju kondensasi akibat pengaruh kecepatan udara terhadap karakteristik perpindahan panas pada oven pengering pati sagu kapasitas,” no. April, pp. 108–114, 2018.

[8] R. Sary, “Kaji eksperimental pengeringan biji kopi dengan menggunakan sistem konveksi paksa,” vol. 14, no. 7, pp. 13–18, 2016.

[9] P. P. Menyeluruh, P. Tekanan, M. Iskandar, A. Hakim, and M. Bakrie, “Pengaruh Baffle Cut Pada Shell dan Tube Heat Exchanger Terhadap Koefisien Pengaruh Baffle Cut Pada Shell dan Tube Heat Exchanger Terhadap Koefisien Perpindahan Panas Menyeluruh & Penurunan Tekanan,” no. September, 2024, doi: 10.31851/redoks.v9i2.9089.

[10] F. T. Industri, “Analisis Perpindahan Panas Pada Oven Electric Heaters Oven For Drying”.

[11] D. Version, “Modelling of Heat Transfer and Fluid Flow in the Hot Section of Gas Turbines Used in Power Generation : A Comprehensive Survey,” 2018, doi: 10.1002/er.4296.

[12] T. R. Steiner, “Results in Engineering High temperature steady-state experiment for computational radiative heat transfer validation using Comsol and Ansys,” *Results Eng.*, vol. 13, no. January, p. 100354, 2022, doi: 10.1016/j.rineng.2022.100354.

[13] G. Michael and R. Hulu, “Analisis Perpindahan Panas Dan Efektivitas Economizer Pada Boiler Unit 4 PLTU Pangkalan Susu,” vol. 2, no. 1, 2021.

[14] Jeffry, I. Isranuri, M. Sabri, S. Abda, and M. Marragi, “Analisa Simulasi Distribusi Temperatur Dan Tekanan Menggunakan Aplikasi Ansys 15.0 Pada Ruang Bakar Turbin Gas Untuk Mengetahui Tingkat Keadaan,” no. 3, pp. 67–80, 2019.

[15] A. L. I. Alsharea, E. J. Lavasani, I. Stamatin, C. Diac, and A. Balan, “Designing Geometries In Solidworks

For Heat Transfer Simulations In Ansys," vol. 902, pp. 1–16, 2025.

[16] S. Perpindahan, P. Pada, D. Ruang, and J. D. Hasibuan, "Bakar Boiler Dengan Software Ansys Skripsi Oleh : Fakultas Teknik Universitas Medan Area Medan Skripsi Diajukan sebagai Salah Satu Syarat untuk Memperoleh Gelar Sarjana di Program Studi Teknik Mesin Fakultas Teknik Universitas Medan Area Oleh : Joel Davidson Hasibuan Fakultas Teknik Medan," 2023.

[17] JMPQ Delgado, "eat transfer and fluid flo in separation and transport procesesses," Trans Tech Publication, p. 32.

[18] A. R. Wardana, A. Mukhtar, and A. Burhanuddin, "Analisis Persebaran Panas Pada Mesin Oven Pengering Kerupuk Dengan Burner Sederhana Berbasis Computational Fluid Dynamics," vol. 4, no. 2, pp. 15–24, 2024.

[19] Sabiqunassabiqun, "2D Analysis Of The Effect Of Outlet Position In A Drying," vol. 2, no. 2, pp. 193–202, 2025.

[20] Z. Khatir *et al.*, "Computational fluid dynamics (CFD) investigation of air flow and temperature distribution in a small scale bread-baking oven," *Appl. Energy*, vol. 89, no. 1, pp. 89–96, 2012, doi: 10.1016/j.apenergy.2011.02.002.

[21] A. Kumar, A. Dewangan, O. Khan, P. Kumar, and N. Kumar, "Influence of ceiling fan induced mass flow rate to create uniform temperature distribution in a closed room : A CFD investigation," *Int. J. Thermofluids*, vol. 26, no. February 2025, p. 101140, 2027, doi: 10.1016/j.ijft.2025.101140.

[22] A. Kumar, A. Dewangan, and O. Khan, "Corrigendum to ' Influence of ceiling fan induced mass flow rate to create uniform temperature distribution in a closed room : A CFD investigation ,'" *Int. J. Thermofluids*, vol. 27, no. March 2025, p. 101156, 2027, doi: 10.1016/j.ijft.2025.101156.

[23] M. Abaee, S. Sohrabi, and M. K. Moraveji, "CFD assisted engineering of spiral microfluidic reactors for room temperature synthesis of ZnO nanoparticles," *Ceram. Int.*, vol. 50, no. 18PA, pp. 32613–32623, 2024, doi: 10.1016/j.ceramint.2024.05.495.

[24] A. Azma and Y. Liu, "Case Studies in Thermal Engineering Enhancing CFD computational efficiency using hybrid data-driven and physics-based modeling," *Case Stud. Therm. Eng.*, vol. 78, no. December 2025, p. 107641, 2026, doi: 10.1016/j.csite.2026.107641.

[25] S. Marashian, O. Abouali, A. Vadiee, and S. Sadrizadeh, "Evaluating the effectiveness of personalized exhaust in minimizing cross contamination in two-bed patient rooms using CFD," *J. Build. Eng.*, vol. 120, no. August 2025, p. 115577, 2026, doi: 10.1016/j.jobe.2026.115577.

[26] S. Tang, J. Zhong, M. Li, Y. Jiang, Y. Zhang, and J. Deng, "Field synergy enhancement of fluid flow and heat transfer in intensive tobacco roasting room," *Comput. Electron. Agric.*, vol. 238, no. August, p. 110837, 2025, doi: 10.1016/j.compag.2025.110837.

[27] X. Chen, Z. Wu, R. Ma, Z. Wang, Z. Wang, and X. Wang, "Wind and thermal comfort performance of the fourth-generation apartment housing in Northern and Southern China based on the 'CFD–APMV' method," *Sustain. Cities Soc.*, p. 107655, 2026, doi: 10.1016/j.scs.2026.107655.

[28] G. Baldinelli, J. Schnotale, F. Bianchi, and A. Lechowska, "Energy & Buildings A variable thermal transmittance adaptive wall : comparison between CFD simulations and experimental tests," *Energy Build.*, vol. 350, no. September 2025, p. 116629, 2026, doi: 10.1016/j.enbuild.2025.116629.

[29] H. Zhao, X. Jian, B. Zhou, W. Li, and Z. Xu, "Energy & Buildings Thermal comfort of medical staff in operating rooms : a review and future perspectives," *Energy Build.*, vol. 364, no. 30, p. 117640, 2026, doi: 10.1016/j.enbuild.2026.117640.

[30] P. Kamma, K. Loksupapaiboon, J. Phromjan, and A. Boekfah, "Optimization of cooking vessel geometry for enhanced flame impingement heat transfer using a hybrid CFD and artificial intelligence approach," *Int. Commun. Heat Mass Transf.*, vol. 178, no. P4, p. 111831, 2026, doi: 10.1016/j.icheatmasstransfer.2026.111831.

[31] H. Wang, K. Qiu, Z. Gao, J. Hang, and J. Shen, "Urban Climate A CFD simulation study on the effect of air-conditioning outdoor units on the wind-thermal environment in street canyons," *Urban Clim.*, vol. 67, no. March, p. 102875, 2026, doi: 10.1016/j.uclim.2026.102875.

[32] A. Ravikumar *et al.*, "An improved CFD wall heat transfer model based on a critical analysis in heavy-duty diesel engines ☆," *Appl. Therm. Eng.*, vol. 302, no. P3, p. 131878, 2026, doi: 10.1016/j.applthermaleng.2026.131878.

LOGIC (JOURNAL ENGINEERING DESIGN AND TECHNOLOGY)
Journal Engineering Design and Technology
Vol. 26 No.2 July 2026 ; p. 167 - 176
Journal Homepage : http://ojs2.pnb.ac.id/index.php/LOGIC
p-ISSN : 1412-114X e-ISSN : 2580-5649

Analysis of Spray Droplet Nozzle Characteristics on Biodiesel (B35) with Injection Pressure Variations

Syaiful Arif [1)*], Joni Arif [1)], Widarto[1)]

1) Mechanical Engineering Study Program, Faculty of Engineering, Pamulang University Jl. Lintas Serang – Jakarta, Kampung Malandang, Kelurahan Kelodran, Kecamatan Walantaka, Kota Serang, Banten

Corresponding email [1)*] :
Syaifularif703@gmail.com

Abstract. This study, entitled *Analysis of Spray Droplet Characteristics of Nozzle in Biodiesel (B35) under Injection Pressure Variations*, investigates the effect of injection pressure on the spray droplet atomization characteristics of Biodiesel B35 and correlates these characteristics with changes in fuel molecular composition determined using Gas Chromatography–Mass Spectrometry (GC–MS). The novelty of this research lies in integrating spray atomization analysis with GC–MS-based molecular characterization to explain how molecular composition influences fuel atomization behavior. An experimental approach was employed using several injection pressure variations in a nozzle system, followed by GC–MS analysis of Diesel B0, Biodiesel B35, and the B0+B35 blend. The GC–MS results revealed that the blended fuel exhibited a broad molecular weight distribution ranging from 106.165 to 843.6107 g/mol, containing both light hydrocarbons, such as O-xylene (C_8H_{10}), and heavy hydrocarbons, such as hexacontane ($C_{60}H_{122}$). Biodiesel B35 showed the highest average molecular weight due to the predominance of fatty acid methyl ester (FAME) compounds, whereas Diesel B0 exhibited the lowest molecular weight because of its higher proportion of light hydrocarbon fractions. The blending process also resulted in stable, reduced, disappeared, and newly formed molecular species, indicating changes in molecular distribution caused by physical interactions between the fuels. These compositional changes affected key fuel properties, including viscosity, volatility, and atomization performance. Spray image analysis demonstrated that increasing injection pressure produced finer and more uniformly distributed droplets, indicating improved atomization quality. The findings demonstrate that the interaction between fuel molecular characteristics and injection pressure plays a significant role in determining spray behavior and has the potential to improve diesel engine combustion efficiency and fuel performance.

Keywords : Biodiesel B35, Diesel B0, GC-MS, spray droplet, injection pressure, atomization, nozzle..

1. INTRODUCTION

Current advances in diesel engine technology increasingly demand improved combustion efficiency and reduced exhaust emissions. Diesel engines remain one of the most widely used power generation systems in the transportation, industrial, agricultural, and power generation sectors because of their high thermal efficiency, reliability, and durability [1]. However, diesel engines are also significant sources of particulate matter (PM), carbon monoxide (CO), unburned hydrocarbons (HC), and nitrogen oxides (NOx), all of which contribute to environmental degradation and adverse human health effects [2]. Consequently, the development of cleaner alternative fuels and the optimization of fuel injection systems have become major research priorities aimed at achieving higher combustion efficiency while meeting increasingly stringent emission regulations [3]. In Indonesia, the mandatory implementation of Biodiesel B35, consisting of 35% fatty acid methyl ester (FAME) blended with 65% petroleum diesel, has been fully implemented since 2023 as part of the national strategy to reduce dependence on fossil fuels, improve energy security, and lower greenhouse gas emissions. The nationwide B35 program has substantially increased biodiesel utilization, making Indonesia one of the world's largest biodiesel consumers and producers [3], [4]. Although B35 offers significant environmental and economic benefits, its higher viscosity, density, and molecular weight compared with conventional diesel fuel alter spray atomization characteristics, fuel-air mixing, and combustion performance. These changes highlight the importance of understanding the relationship between the molecular composition of Biodiesel B35 and its spray characteristics under different injection pressures, thereby providing scientific support for optimizing diesel engine performance and fuel injection systems [4–6].

One effort to reduce the environmental impact of diesel engine use is the use of biodiesel as an alternative fuel. Biodiesel, such as B35, is a blend of fossil diesel fuel and fatty acid methyl ester (FAME)-based biodiesel[4]. The use of biodiesel not only aims to reduce dependence on fossil fuels but also to improve lubrication properties and lower overall carbon emissions[3], [4]. Biodiesel has different physical characteristics than conventional diesel, such as higher viscosity, greater density, and lower volatility. These differences can affect the injection and combustion processes in a diesel engine's combustion chamber[5], [6]. One crucial aspect of a diesel engine system is the fuel injection process through the nozzle. This process significantly determines the quality of fuel atomization, which is the process of breaking down liquid fuel into small droplets that mix with air before combustion occurs[7]. Atomization quality is greatly influenced by injection pressure, nozzle design, and the physical properties of the fuel used. The better the atomization process, the greater the contact surface area between the fuel and air, allowing for faster and more complete vaporization and combustion.Injection Pressure (IP) is a key factor influencing spray droplet characteristics[6], [7], [8]. Increasing injection pressure generally results in smaller droplet sizes and a more homogeneous spray distribution. This occurs because the greater kinetic energy breaks down the fuel stream into finer particles. Conversely, lower injection pressure tends to produce larger droplets and uneven distribution, which can reduce combustion efficiency[6], [8].

In addition to pressure, the chemical composition of the fuel also significantly influences the atomization process. Diesel B0 and Biodiesel B35 blends have different molecular characteristics, both in terms of carbon chain length and oxygen content in their molecular structures[4], [5]. Diesel B0 is dominated by aliphatic hydrocarbons with high volatility, while Biodiesel B35 contains ester compounds with longer carbon chains and oxygen-rich properties[9], [10]. These differences cause changes in physical properties such as viscosity, density, and surface tension, which ultimately affect the spray droplet formation process at the nozzle.Based on Gas Chromatography–Mass Spectrometry (GC-MS) testing results, the blend of Diesel B0 and Biodiesel B35 exhibits a fairly broad molecular distribution, with the presence of light to heavy compounds. This indicates that the blend is not simply a simple combination but also undergoes changes in molecular distribution due to physical interactions between the components[10]. Light compounds, such as O-xylene, play a role in the initial evaporation process, while heavy compounds, such as hexacontane, affect viscosity and atomization. These differences in molecular characteristics directly impact the fuel's combustion properties[11].

Changes in molecular composition due to blending also indicate the presence of compounds that remain constant, are reduced, are lost, and are formed. This phenomenon indicates that the blending process is not simply a physical process but also affects the chemical distribution within the blend[11], [12], [13]. The dominance of hydrocarbons in diesel and the contribution of ester compounds in biodiesel create intermediate fuel characteristics, somewhere between those of pure diesel and pure biodiesel.In the context of an injection system, these changes in the physical and chemical properties of the fuel have a direct impact on spray droplet characteristics[12], [13], [14]. Fuels with higher viscosity tend to produce larger droplets, resulting in less optimal atomization. Conversely, fuels with high volatility evaporate more easily and form a more homogeneous mixture with air. The combination of injection pressure variations and fuel type is a crucial factor in determining combustion quality[14], [15].

Based on this description, a more in-depth analysis is needed regarding the relationship between injection pressure variations and spray droplet characteristics in B35 biodiesel, as well as how changes in fuel molecular composition affect the atomization process[16], [17]. To address this gap, the present study integrates GC–MS-based molecular characterization with spray droplet analysis under various injection pressures. The novelty of this research lies in establishing the relationship between changes in fuel molecular composition, particularly in Biodiesel B35 and its blends, and the resulting spray atomization characteristics. By combining chemical and spray analyses within a single experimental framework, this study provides a more comprehensive understanding of the mechanisms governing fuel atomization. The findings are expected to contribute to the optimization of diesel fuel injection systems, support the development of more efficient and environmentally friendly diesel engines, and provide scientific guidance for the wider application of biodiesel fuels in modern diesel engine technology.

2. METHODS

This study employed an experimental research approach to investigate the effect of injection pressure variations on spray droplet characteristics in a diesel fuel system using Biodiesel B35, Diesel B0, and their blends[18]. The experimental method was selected because it allows direct observation of cause-and-effect relationships between controlled variables (injection pressure and fuel type) and the resulting response variable (spray droplet characteristics)[16], [17], [18]. The study was conducted under controlled laboratory conditions to ensure consistency and repeatability of results.

Research Approach and Design

The research design used in this study is a quantitative experimental design. The independent variables include injection pressure variations and fuel type (Diesel B0, Biodiesel B35, and B0+B35 blend). The dependent variable is the spray droplet characteristics, which include droplet diameter and spray pattern distribution. Controlled variables include nozzle type, ambient temperature, and test setup configuration to minimize external influences on the results.

Population and Sample

The population in this study refers to all possible spray characteristics generated by diesel injection systems under varying operating conditions[18], [19]. The sample consists of spray droplets produced from a test nozzle system using three types of fuel: Diesel B0, Biodiesel B35, and a 1:1 mixture of both fuels (50 ml Diesel B0 and 50 ml Biodiesel B35). Each fuel sample was tested under multiple injection pressure conditions to obtain comparative data on spray droplet behavior.

Operational Definition of Variables

Injection pressure is defined as the pressure applied to force fuel through the nozzle during the injection process, measured in bar or MPa[2], [3], [5]. Fuel type refers to the composition of the tested fuel, namely Diesel B0, Biodiesel B35, and their mixture. Spray droplet characteristics are defined as the physical attributes of the atomized fuel, including droplet diameter size, distribution pattern, and spray dispersion quality. Smaller droplet diameters indicate better atomization quality, which contributes to improved combustion efficiency.

Data Collection Methods

Data collection was conducted using an experimental test rig consisting of a fuel injection system, high-pressure pump, nozzle, and pressure gauge. Fuel was injected through the nozzle under controlled pressure variations[9], [10]. The resulting spray was captured using a high-speed imaging system combined with proper lighting to ensure clear visualization of droplet formation. The recorded images were then analyzed using image processing techniques to determine droplet size and distribution.

Additionally, chemical composition data of the fuels were obtained using Gas Chromatography–Mass Spectrometry (GC-MS) analysis. This method was used to identify molecular composition, molecular weight distribution, and chemical changes in Diesel B0, Biodiesel B35, and their blends. The GC-MS data provided supporting information to explain differences in physical spray characteristics based on fuel molecular structure.

Data Analysis Method

The experimental data were analyzed using quantitative and descriptive statistical methods. Spray images were processed using digital image analysis software to determine droplet size distribution under each injection pressure and fuel type [11], [12]. Prior to analysis, the images were calibrated using a reference scale, converted into grayscale, and segmented using an intensity threshold to identify individual droplets. The equivalent droplet diameter was then calculated for each test condition, and the average droplet size together with its distribution was used to evaluate atomization performance.

Each experimental condition was repeated to ensure measurement consistency, and the results are presented as mean values. GC–MS analysis was performed under controlled operating conditions using helium as the carrier gas, with the injector operated in split mode and the oven temperature programmed from a low initial temperature to a higher final temperature to separate compounds with different boiling points [9], [10]. The obtained chromatograms and mass spectra were analyzed by comparing the detected peaks with the reference library to identify molecular species and determine their relative abundances. The analysis focused on molecular weight distribution, dominant compounds, and compositional changes among Diesel B0, Biodiesel B35, and the blended fuel samples. The relationships between fuel molecular characteristics, including molecular weight, viscosity, and volatility, and spray droplet behavior were evaluated by comparing the experimental results obtained under different injection pressures. Descriptive statistical analysis was employed to identify trends in droplet size variation and atomization quality, while the combined physical and chemical analyses were used to explain the influence of fuel composition on spray characteristics and their implications for diesel engine combustion performance.

3. RESULTS AND DISCUSSION

3.1 GC-MS Test of Diesel B0 + Biodiesel B35

Gas Chromatography–Mass Spectroscopy (GC–MS) testing on a mixture of Diesel B0 + Biodiesel B35 fuel was carried out to identify the chemical composition of compounds and understand the changes in molecular distribution due to the mixing process of the two fuels. This analysis aims to provide a comprehensive picture of the molecular characteristics of the mixture, which is a combination of aliphatic hydrocarbons from diesel and ester compounds (fatty acid methyl esters/FAME) from biodiesel[12], [13]. The B0+B35 mixture has chemical properties that are not simply the sum of each component, but also show changes in compound distribution due to physical interactions and differences in volatility properties. Therefore, the use of the GC–MS method is very important to separate and identify each component based on the retention time and the resulting mass fragmentation pattern. Through this test, it is expected to determine the dominance of the type of compound in the mixture, changes in the amount or loss of certain compounds, and the range of molecular weights formed. This information is the basis for understanding the effect of fuel composition on physical properties, such as viscosity and volatility, as well as its implications for the atomization and combustion processes in diesel engines, as seen in Figure 1 below.

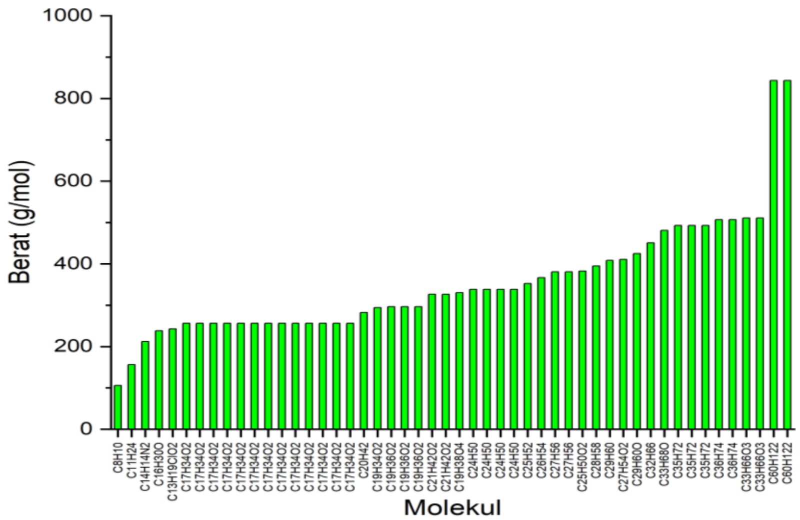

Figure 1 GC-MS Test Results of Diesel B0 + Biodiesel B35

The results of GC-MS testing of Diesel B0 Biodiesel B35 fuel showed the lowest molecular weight of O-Xylene C_8H_{10} = 106.165 grams/mol, while the highest molecular weight of Hexacontane $C_{60}H_{122}$ = 843.6107 grams/mol. Based on Figure 1, the results of Gas Chromatography–Mass Spectroscopy (GC–MS) testing on the Diesel B0 + Biodiesel B35 fuel mixture showed a fairly wide molecular weight distribution. The compound with the lowest molecular weight was identified as O-xylene (C_8H_{10}) with a value of 106.165 g/mol, while the compound with the highest molecular weight was hexacontane ($C_{60}H_{122}$) with a value of 843.6107 g/mol. The presence of O-xylene as a light aromatic compound indicates the presence of volatile fractions in the fuel mixture. This compound has a relatively low boiling point, making it crucial for the initial evaporation process and the formation of the air-fuel mixture. This light fraction supports better atomization and accelerates ignition during combustion.

The presence of hexacontane, a very long-chain hydrocarbon, indicates the presence of a heavy fraction with low volatility[4], [5]. This compound tends to increase fuel viscosity and slow the evaporation process. In a combustion system, the heavy fraction can cause delayed atomization, larger droplet formation, and the potential for residue or deposit formation. The broad molecular distribution of the B0+B35 blend reflects a combination of characteristics between pure diesel and biodiesel. The B0 diesel contributes light to medium hydrocarbon fractions, while the B35 biodiesel contributes to an increase in long-chain compounds and oxygenates. As a result, this blend has intermediate properties in terms of both volatility and viscosity. Overall, the GC-MS results indicate that:

a) The B0+B35 mixture has a wide molecular weight range (±106–843 g/mol)
b) Contains a combination of light aromatic compounds and heavy hydrocarbons
c) The fuel's characteristics are intermediate between diesel and biodiesel.

The implication of these results is that the fuel mixture has a balance between ease of evaporation (from the light fraction) and energy stability (from the heavy fraction). The increase in heavy fractions can also affect the atomization and combustion processes, which is in line with the results of previous tests related to droplet size. Thus, this GC–MS analysis provides an important basis in understanding the relationship between molecular composition and fuel performance in a diesel engine system. Based on the results of the GC–MS analysis of the

Diesel B0 + Biodiesel B35 fuel mixture, compounds with a fairly contrasting molecular weight range were identified, namely C_8H_{10} as the light fraction and $C_{60}H_{122}$ as the heavy fraction. The C_8H_{10} compound is an aromatic hydrocarbon with a relatively low molecular weight, which is included in the group of volatile compounds. The presence of this compound indicates that the fuel mixture still contains light fractions that play an important role in the initial evaporation process. This fraction supports faster formation of the air-fuel mixture and increases the ease of ignition during the combustion process. In contrast, the compound $C_{60}H_{122}$ is a very long-chain hydrocarbon with a high molecular weight included in the heavy fraction. This compound has low volatility and tends to increase fuel viscosity. Its presence can affect the atomization process by producing larger droplets and slowing the fuel evaporation process in the combustion chamber. The significant difference between the two compounds shows that the B0+B35 mixture has a wide molecular distribution, reflecting a combination of characteristics of pure diesel and biodiesel. The light fraction of diesel contributes to increased volatility, while the heavy fraction of biodiesel increases the content of long-chain molecules, as seen in Figure 2 below.

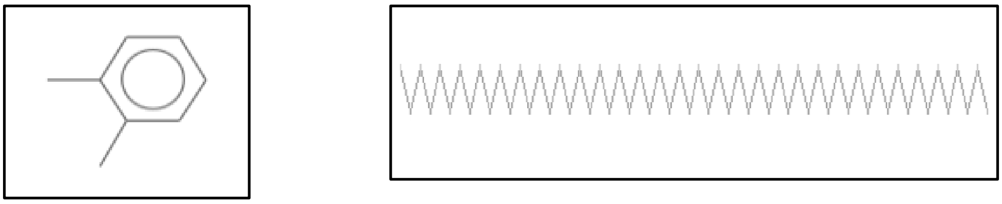

C_8H_{10} **$C_{60}H_{122}$**

Figure 2. Results of GC-MS (Gas Chromatography-Mass Spectrometry) testing

The results of the GC-MS (Gas Chromatography-Mass Spectrometry) test showed that the average molecular weight was highest for B35 biodiesel, followed by the B0+B35 mixture, and the lowest for B0 diesel fuel. The results of the Gas Chromatography–Mass Spectrometry (GC–MS) test showed differences in the distribution of average molecular weights for each type of fuel tested. Based on this analysis, it was found that B35 biodiesel had the highest average molecular weight, followed by the B0+B35 mixture, and the lowest was B0 diesel fuel. The higher average molecular weight value in B35 biodiesel was due to the dominance of fatty acid methyl ester (FAME) compounds which have long carbon chains and contain oxygen groups in their molecular structure. These compounds generally have a larger molecular mass than the hydrocarbons that make up diesel, thus increasing the overall average molecular weight of biodiesel. In the B0+B35 mixture, the average molecular weight value is between the two, which indicates intermediate properties due to the combination of hydrocarbon compounds from diesel and ester compounds from biodiesel. The decrease in the average molecular weight compared to B35 occurs due to dilution by B0 diesel which has lighter molecular components. B0 diesel has the lowest average molecular weight because it is dominated by aliphatic hydrocarbon compounds with relatively shorter carbon chains and does not contain oxygenate groups. This causes the properties of diesel fuel to be lighter and have higher volatility. This difference in average molecular weight has direct implications for the physical properties and performance of the fuel, including:

a) B35 biodiesel tends to have higher viscosity and lower volatility
b) B0 diesel has higher volatility and better atomization
c) B0+B35 blends exhibit intermediate characteristics

The results of GC-MS (Gas Chromatography-Mass Spectrometry) confirm that increasing the biodiesel content in fuel will increase the average molecular weight, which in turn affects the atomization process, droplet formation, and combustion efficiency in the diesel engine system, as seen in Figure 3 below.

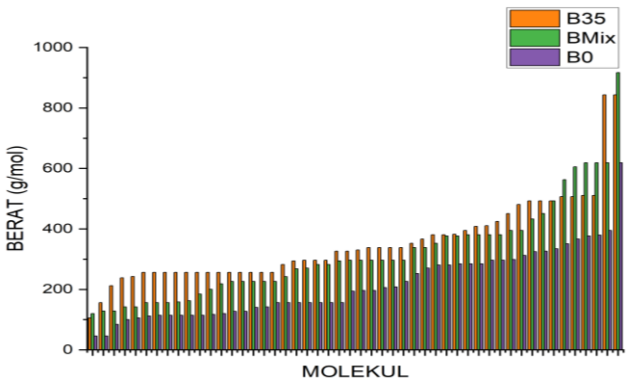

Figure 3 Molecular Weight of GC-MS Test Results of Biodiesel B0, B35 and Bmix

Figure 3 shows the molecular weight distributions from GC-MS analysis of three types of fuel: B0, B35, and Bmix. In general, the graph shows that all samples experienced an increase in molecular weight from the light compound fraction to the heavy compound fraction. This reflects variations in carbon chain length in each fuel, with low molecular weight compounds being at the beginning of the graph, while high molecular weight compounds were at the end. B0, which is pure diesel fuel without biodiesel blends, shows a tendency for lower molecular weight values compared to B35 and Bmix. This indicates that B0 is dominated by hydrocarbon compounds with relatively shorter carbon chains. This characteristic makes B0 more volatile and has a better atomization process during combustion. This dominance of light compounds can also have an impact on environmentally unfriendly emissions, such as increased hydrocarbon (HC) and carbon monoxide (CO) emissions.

In contrast to B0, B35 shows the highest molecular weight value among the three samples, especially in the heavy compound fraction at the end of the graph[6], [7], [8]. This is due to the 35% biodiesel content, which generally consists of long-chain fatty acid methyl esters (FAME). The presence of these compounds increases the average molecular weight of the fuel. Consequently, B35 tends to have a higher viscosity and slower evaporation rate than B0. This fuel has the advantage of cleaner and more stable combustion, as well as lower emissions, making it more environmentally friendly. Bmix exhibits characteristics that fall between B0 and B35. Its molecular weight is neither as low as B0 nor as high as B35, indicating that this blend composition produces a more balanced distribution of compounds between light and heavy fractions[5], [6], [13]. This provides the advantage of a combination of properties, maintaining adequate atomization while improving combustion quality and reducing emissions. Bmix can be considered an optimal compromise between engine performance and environmental aspects.

In the heavy fraction section, a significant increase was observed in B35, followed by Bmix, and then B0. This phenomenon confirms that the higher the biodiesel content in the mixture, the greater the contribution of heavy compounds in the fuel[9], [10]. These heavy compounds generally come from long carbon chains that play a role in increasing the lubricity value of the fuel and combustion stability. The analysis results show that increasing the biodiesel content in the fuel mixture is directly proportional to the increase in the average molecular weight. This has a positive impact on reducing emissions and improving combustion quality, but also needs to be balanced with attention to the physical properties of the fuel such as viscosity and atomization ability. Selecting the right mixture composition is an important factor in optimizing fuel performance while maintaining environmental aspects, as seen in Figure 4 below.

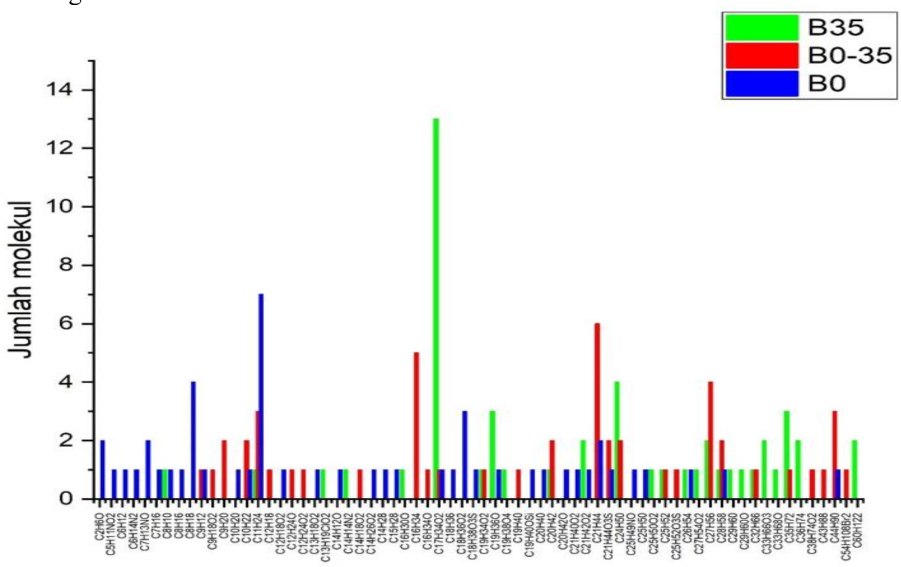

Figure 4 Changes in Molecular Compounds of Biodiesel B0, B35 and Bmix

Based on the results of GC-MS analysis. The horizontal axis represents the type of compound (generally hydrocarbons and their derivatives with varying carbon chain lengths), while the vertical axis shows the number of molecules or the intensity of the compound's appearance in the sample[12], [13], [14]. The graph shows that each fuel has different molecular composition characteristics. In B0 (blue), the distribution of compounds tends to be more even but with a relatively low to moderate number of molecules in almost all fractions. This indicates that pure diesel is dominated by a mixture of hydrocarbons with a fairly wide distribution, but no single type of compound is very dominant. This composition is common in fossil fuels consisting of various hydrocarbon fractions, ranging from short to medium chains. In B35 (green), there is a significant spike in certain types of compounds, indicated by peaks in the number of molecules that are much higher than in B0. This indicates the dominance of certain compounds, which are most likely methyl ester compounds (FAME) resulting from biodiesel. These compounds usually have a long carbon chain structure (e.g., C_{16}–C_{18}) and appear in greater amounts due to the relatively high composition of biodiesel (35%). This dominance indicates that the addition of biodiesel not only increases the molecular weight (as seen in Figure 3) but also significantly changes the chemical composition of the fuel by increasing the concentration of certain compounds.

B0-35 (red) shows a distribution pattern that falls between B0 and B35. The number of molecules in some compounds increases compared to B0, but not as much as B35. This indicates that this blend produces a more balanced composition between hydrocarbons from diesel and esters from biodiesel. The absence of extreme dominance of any one compound indicates that B0-35 has a more homogeneous blend, potentially providing more stable combustion characteristics than B0, without the excessive increase in viscosity as in B35. This change in the number of molecules significantly impacts the physical and chemical properties of the fuel. In B35, the dominance of ester compounds tends to increase the fuel's viscosity, density, and lubrication properties. The oxygen content in biodiesel molecules also contributes to more complete combustion, thereby reducing emissions of harmful gases such as carbon monoxide and unburned hydrocarbons. On the other hand, the dominance of certain compounds can also lead to uneven evaporation characteristics.

In B0, although the compound distribution is more even, the absence of oxygen in the hydrocarbon molecules tends to result in incomplete combustion, potentially increasing emissions. Meanwhile, in B0-35, the combination of the two compounds provides a balance between combustion performance and the fuel's physical properties, making it an optimal alternative for diesel engine applications. Figure 4 shows that increasing the biodiesel content in a fuel blend not only affects the molecular weight but also significantly alters the distribution and dominance of the chemical compounds within it. These changes directly impact combustion characteristics, energy efficiency, and emissions, making selecting the right blend composition crucial for developing efficient and environmentally friendly fuels.

A. Fixed Molecules

Based on Figure 4, the results of GC-MS testing of molecular compounds that do not change (remain) in B35 biodiesel mixed with B0 diesel fuel are: $C_{19}H_{34}O_2$, $C_{25}H_{52}$, $C_{32}H_{66}$ and the results of GC-MS testing, there are several compounds that do not experience changes (remain present) when B35 biodiesel is mixed with B0 diesel fuel, namely $C_{19}H_{34}O_2$, $C_{25}H_{52}$, and $C_{32}H_{66}$. The presence of these compounds in both B0, B35, and their mixtures indicates that these compounds are stable and not significantly affected by the mixing process. The $C_{19}H_{34}O_2$ compound is a group of fatty acid esters (Fatty Acid Methyl Ester/FAME) which generally comes from biodiesel. Its constant presence indicates that the main components of biodiesel do not experience degradation or further chemical reactions when mixed with diesel fuel. This indicates that the blending process between B35 and B0 is physical (physical mixing), not a chemical reaction that changes the molecular structure. Meanwhile, $C_{25}H_{52}$ and $C_{32}H_{66}$ are saturated hydrocarbon compounds (long-chain alkanes) that generally come from the heavy fraction in diesel (B0). The fact that these compounds remained detectable after blending indicates that the hydrocarbon components of diesel also did not experience changes in chemical structure during the blending process. The presence of these compounds has several important implications. First, it confirms that blending biodiesel and diesel does not damage the main components of each fuel, so that the basic properties of both are still maintained. Second, the stability of these compounds indicates good compatibility between biodiesel and diesel, which is important to ensure optimal engine performance. Third, the presence of ester and hydrocarbon compounds together in the blend provides a combination of properties, such as improved lubricity of biodiesel and combustion characteristics of diesel.

B. Molecules Reduce and Disappear

The molecular composition of B35 biodiesel, after being mixed with B0 diesel, changes occur, with some molecules being reduced or lost. The same molecular composition, but with a reduced quantity, is: $C_{17}H_{34}O_2$, $C_{24}H_{50}$, $C_{35}H_{72}$. While the missing molecular compounds are C_8H_{10}, $C_{13}H_{19}C_1O_2$, $C_{14}H_{14}N_2$, $C_{16}H_{30}O$, $C_{19}H_{36}O$, $C_{19}H_{38}O_4$, $C_{21}H_{42}O_2$, $C_{25}H_{50}O_2$, $C_{26}H_{54}$, $C_{27}H_{54}O_2$, $C_{29}H_{60}$, $C_{29}H_{60}O$, $C_{33}H_{66}O_3$, $C_{33}H_{68}O$, $C_{36}H_{74}$, $C_{60}H_{122}$. The results of the molecular composition analysis showed that B35 biodiesel experienced changes in its chemical structure after being mixed with B0 diesel fuel. This change was indicated by a decrease in the number of several molecular compounds and the loss of certain components in the B0+B35 mixture. This phenomenon indicates the occurrence of physical interactions and the possibility of changes in component distribution during the mixing process. Molecular compounds that were still detected but experienced a decrease in number included C17H34O2, $C_{24}H_{50}$, and $C_{35}H_{72}$. These compounds are generally part of the main structure of biodiesel and long-chain hydrocarbons. The decrease in intensity or amount can be caused by the dilution effect of B0 diesel, so that the relative proportion of the compound becomes smaller in the mixture. There are a number of compounds that are no longer detected after mixing, namely C_8H_{10}, $C_{13}H_{19}ClO_2$, $C_{14}H_{14}N_2$, $C_{16}H_{30}O$, $C_{19}H_{36}O$, $C_{19}H_{38}O_4$, $C_{21}H_{42}O_2$,

$C_{25}H_{50}O_2$, $C_{26}H_{54}$, $C_{27}H_{54}O_2$, $C_{29}H_{60}$, $C_{29}H_{60}O$, $C_{33}H_{66}O_3$, $C_{33}H_{68}O$, $C_{36}H_{74}$, and $C_{60}H_{122}$. The loss of these compounds can be caused by several factors, including:

a) Dilution effect, where the concentration of a compound becomes so low that it is undetectable by the instrument.
b) Differences in volatility, which cause some components to evaporate more easily or not be detected in the test.
c) Interactions between molecules, which allow for changes in the distribution or association of molecules in the fuel mixture.

These changes in molecular composition indicate that blending biodiesel with diesel not only results in a simple mixture, but also affects the distribution of chemical compounds within it. The dominance of hydrocarbons from B0 diesel causes a relative decrease in oxygenate compounds derived from biodiesel. The implications of these changes are quite significant for fuel properties, including:

a) A decrease in oxygenate compound content can affect combustion quality.
b) Changes in carbon chain composition affect fuel viscosity and density.
c) Variations in molecular structure impact the atomization process and droplet size.

This molecular composition analysis strengthens the results of previous FTIR tests, that the B0+B35 mixture has intermediate chemical characteristics influenced by the dominance of diesel hydrocarbons and limited contribution from biodiesel ester compounds.

C. New and Added Molecules

Phenomena that occur after B35 biodiesel is mixed with B0 diesel include the presence of additional molecules and new molecules. These molecules include: $C_{11}H_{24}$, $C_{20}H_{42}$, $C_{27}H_{56}$, $C_{28}H_{58}$ and the newly formed molecules are: C_9H_{12}, $C_9H_{18}O_2$, C_9H_{20}, $C_{10}H_{22}$, $C_{12}H_{18}$, $C_{12}H_{24}O$, $C_{12}H_{24}O_2$, $C_{14}H_{18}O_2$, $C_{16}H_{34}$, $C_{16}H_{34}O$, $C_{19}H_{40}$, $C_{21}H_{44}$, $C_{21}H_{44}O_3S$, $C_{25}H_{52}O_3S$, $C_{38}H_{74}O_2$, $C_{43}H_{88}$, $C_{44}H_{90}$, $C_{54}H_{108}Br_2$

4. CONCLUSION

Based on the experimental results, it can be concluded that both injection pressure and fuel molecular characteristics significantly influence the atomization behavior of Biodiesel B35. GC–MS analysis revealed that the B0+B35 blended fuel exhibited a broad molecular weight distribution ranging from **106.165 to 843.6107 g/mol**, indicating the presence of both light hydrocarbons, such as O-xylene (C_8H_{10}), and heavy hydrocarbons, such as hexacontane ($C_{60}H_{122}$). Biodiesel B35 exhibited the highest average molecular weight due to the predominance of fatty acid methyl ester (FAME) compounds, whereas Diesel B0 contained a larger proportion of lighter hydrocarbon fractions. The blending process also resulted in stable, reduced, disappeared, and newly formed molecular species, demonstrating changes in molecular distribution that influence important fuel properties, particularly viscosity and volatility.

The spray analysis demonstrated that increasing injection pressure produced finer and more uniformly distributed fuel droplets, indicating improved atomization performance and enhanced fuel–air mixing. These findings confirm that the interaction between fuel molecular composition and injection pressure plays an important role in determining spray characteristics and is expected to improve diesel engine combustion efficiency.

The novelty of this study lies in integrating GC–MS-based molecular characterization with spray droplet analysis to establish the relationship between changes in fuel molecular composition and atomization behavior under different injection pressures. This integrated approach provides a more comprehensive understanding of the mechanisms governing biodiesel spray formation than studies that evaluate fuel composition or spray characteristics separately. The findings provide valuable information for optimizing diesel fuel injection systems, improving combustion efficiency, and supporting the wider implementation of Biodiesel B35 in modern diesel engines.

This study is limited to laboratory-scale spray characterization and molecular composition analysis under controlled operating conditions. Engine performance parameters, combustion characteristics, and exhaust emissions were not directly evaluated. Therefore, future studies should incorporate engine performance testing, combustion analysis, emission measurements, and computational fluid dynamics (CFD) simulations to further validate the relationship between molecular composition, spray atomization, and diesel engine performance under actual operating conditions.

5. ACKNOWLEDGEMENT

The author would like to express sincere gratitude to all parties who have provided support in the completion of this research. Special appreciation is extended to the research supervisor from the Mechanical Engineering Study Program, Faculty of Engineering, Universitas Pamulang, for the opportunity, guidance, and continuous supervision throughout the research process.The author also acknowledges the Faculty of Engineering, Universitas Pamulang, for providing the necessary facilities and infrastructure that supported the successful completion of this study. Furthermore, gratitude is conveyed to colleagues who assisted in data collection and supported the experimental work conducted during the research activities.The support, cooperation, and contributions from all parties have been highly valuable and greatly appreciated in ensuring the successful completion of this research.

6. REFERENCES

[1] S. V. Minov, F. Cointault, J. Vangeyte, J. G. Pieters, and D. Nuyttens, "Spray droplet characterization from a single nozzle by high speed image analysis using an in-Focus droplet criterion," *Sensors (Switzerland)*, vol. 16, no. 2, Feb. 2016, Doi: 10.3390/s16020218.

[2] E. Cerruto, G. Manetto, R. Papa, and D. Longo, "Modelling spray pressure effects on droplet size distribution from agricultural nozzles," *Applied Sciences (Switzerland)*, vol. 11, no. 19, Oct. 2021, Doi: 10.3390/app11199283.

[3] Y. Jiang, C. Chen, H. Li, and Q. J. Xiang, "Influences of nozzle parameters and low-pressure on jet breakup and droplet characteristics," *International Journal of Agricultural and Biological Engineering*, vol. 9, no. 4, pp. 22–32, 2016, Doi: 10.3965/j.ijabe.20160904.2103.

[4] R. Nogueira Martins, H. Marcus Fialho Moraes, M. Alexandre Moreira de Freitas, A. da Costa Lima, and M. Ribeiro Furtado Junior, "Effect of nozzle type and pressure on spray droplet characteristics," Jan. 2021. https://Doi.org/10.4067/S0718-34292021000100101

[5] B. K. Fritz and W. C. Hoffmann, "Measuring spray droplet size from agricultural nozzles using laser diffraction," *Journal of Visualized Experiments*, vol. 2016, no. 115, Sep. 2016, Doi: 10.3791/54533.

[6] Cynthia Marisca Muntu dan Ilona Pricilya Tenderan, "Pengaruh Laju Alir pada Proses Spray Drying terhadap Karakteristik Fisiko Kimia Mikrosfer Glibenklamid menggunakan Polimer Kitosan dan Penyambung Silang Natrium Tripolifosfat," *Media Pharmaceutica Indonesiana*, no. 4, pp. 13–22, Jul. 2022. https://Doi.org/10.24123/mpi.v4i1.5045

[7] A. Agung Surya Dwi Pramana, I. Gusti Bagus Wijaya Kusuma, and dan I. Made Widiyarta, "Pengujian Performance Biodiesel Biji Alpukat Di Tinjau Dari Karakteristik Panjang Penyemprotan Dan Ukuran Butiran," Nov. 2015. Doi: https://Doi.org/10.21776/jrm.v15i2.907

[8] Irwan Tri Murdianto, "Pengaruh Variasi Tekanan Pada Pembakaran Spray Bahan Bakar Minyak Kelapa Murni Terhadap Sudut, Panjang Nyala Api, Diameter Droplet, Flashback," *Mechonversio: Mechanical Engineering Journal*, vol. 2, no. 1, p. 1, Jul. 2019. https://Doi.org/10.51804/mmej.v2i1.820

[9] Muhammat Firman Pratama Hokil, "Peranan Variasi Tekanan Pembakaran Difusi Terhadap Karakteristik Spray Dengan Bahan Bakar Minyak Kapuk," *Mechonversio: Mechanical Engineering Journal*, vol. 2, no. 1, pp. 1–9, Jun. 2019. https://Doi.org/10.51804/mmej.v2i1.823

[10] S. Sukri, M. N. Sasongko, and T. D. Widodo, "Pengaruh Campuran Bahan Bakar Biodiesel WCO - Diesel terhadap Karakteristik Api Hasil Pembakaran Spray Difusi pada Concentric Jet Burner," *Jurnal Rekayasa Mesin*, vol. 12, no. 2, pp. 459–466, Aug. 2021, Doi: 10.21776/ub.jrm.2021.012.02.22.

[11] A. G. Roring, G. Soebiyakto, A. Farid, and D. Hermawan, "Pengaruh Variasi Diameter Nozzle terhadap Dimensi Droplet, Sudut Spray dan Jarak Spray Menggunakan Bahan Bakar Pertalite," *Jurnal Flywheel*, vol. 16, no. 1, pp. 7–12, Feb. 2025, [Online]. Available: https://ejournal.itn.ac.id/index.php/flywheel/ https://Doi.org/10.36040/flywheel.v16i1.9500

[12] M. Suryaningrat, M. Nur Sasongko, N. Hamidi, and N. Saputro, "Analisis Karakteristik Sudut Penyemprotan Biodiesel Palm Oil Melalui Penambahan Variasi Konsentrasi Metanol," *Jurnal Rekayasa Mesin*, vol. 49, no. 4, pp. 37–49, Apr. 2024, Doi: 10.21776/jrm.v15i3.1211.

[13] L. Y. A. S. W. Arwin, "Karakteristik Pembakaran Droplet Dengan Variasi Komposisi Campuran Bensin-Etanol," 2020. https://Doi.org/10.21776/ub.jrm.2020.011.01.1

[14] I Gede Teddy Prananda Surya, "Simulasi Numerik Ii : Distribusi Diameter Droplet Pada Semprotan Biodiesel Kelapa, Jatropa Curcas Dan Minyak Goreng Bekas Dalam Ruang Bakar Mexican Hat," *Jurnal Teknik Mesin*, vol. 6, no. 2, pp. 1–6, Oct. 2020. https://Doi.org/10.33019/jm.v6i2.1381

[15] M. I. Cholis, M. F. Noor, and L. Hakim, "Analisis Karakteristik spray Bahan Bakar Pertalite Pertamax Dan Pertamax Turbo Dengan Campuran Etanol," *Energy : Jurnal Ilmiah Ilmu-Ilmu Teknik*, vol. 14, no. 2, pp. 81–92, Nov. 2024, Doi: 10.51747/energy.v14i2.2075.

[16] T. Y. Ardiansah, "Peranan Variasi Tekanan Terhadap Karakteristik Pembakaran Spray Dengan Campuran Bahan Bakar Minyak Kelapa Dan Minyak Kapuk (B50)," *Mechonversio: Mechanical Engineering Journal*, vol. 3, no. 1, pp. 12–17, 2020. https://Doi.org/10.51804/mmej.v3i1.834
[17] Y. Kurniawan, I. Bagus Dharmawan, P. Negeri Balikpapan, and J. Soekarno Hatta Km, "Karakteristik Spray Bahan Bakar Campuran Bensin-Etanol Pada Vacuum Chamber," Jul. 2024. [Online]. Available: https://jurnal.poltekba.ac.id/index.php/prosiding/index Doi:10.51747/energy.v14i2.2075
[18] A. Pinto, W. Kusuma, and W. B. Adnyana, "Uji Karakteristik Penyemprotan Bahan Bakar Biodiesel Pada Nozel Mesin Diesel Dengan Sistem Injeksi Langsung," Apr. 2015. Doi:10.32486/jeecae.v10i1.759
[19] M. Iqbal Harapan Muslim Siregar, M. Hutagalung, and K. Salomo Sitorus, "Penggantian Nozzle untuk Meningkatkan Daya Mesin Diesel Caterpillar C32 Penggerak Pompa Pemadam Kebakaran," *Cosmic Jurnal Teknik*, vol. 2, no. 2, pp. 65–74, Dec. 2025, Doi: 10.55537/cosmic.